Evaporation-driven formation of supraparticles composed of ellipsoids and spheres

Dissertation

zur Erlangung des Grades
"Doktorin der Naturwissenschaften" (Dr.rer.nat.)
im Promotionsfach Chemie

am Fachbereich Chemie, Pharmazie,
Geographie und Geowissenschaften
der Johannes Gutenberg-Universität Mainz

Melis Yetkin
geboren in Sahinbey, Türkei

Mainz, 2024

This dissertation work was carried out at Max-Planck-Institute for Polymer Research, Mainz from August 2020 to until July 2024 under the supervision of [redacted] and [redacted].

1. Gutachter: [redacted]
2. Gutachter: [redacted]
3. Gutachter: [redacted]
4. Gutachter: [redacted]

Tag der mündlichen Prüfung:

Dedicated to [redacted]

Abstract

When liquids with dispersed colloids evaporate, the colloids left behind can form complex structures, which are important in many natural phenomena and technical applications. The availability of superamphiphobic surfaces opens new opportunities to study the structure formation of evaporating dispersions leading to the fabrication of supraparticles. Supraparticles are engineered materials formed by the directed self-assembly of smaller nano- or microparticles. The material properties of supraparticles can be controlled by tailoring the shape and chemistry of their building blocks, and evaporation conditions. Thus far, spherical colloids have been the conventional choice of building blocks, which leave the use of anisotropic colloids largely unexplored for controlling the supraparticle structure. The self-assembly of ellipsoidal particles is, for instance, particularly interesting, as it offers a broad range of final ordered structures. However, systematic experiments showing the influence of ellipsoid aspect ratio, mixing ellipsoids with spheres, and evaporation rate on the final supraparticle structure are still lacking. In this thesis, I attempt to answer such open questions by investigating the structure formation of evaporation-induced supraparticles composed of polystyrene ellipsoids and/or spheres. To do that, I form supraparticles by evaporating aqueous dispersion droplets of ellipsoids and/or spheres on silicone nanofilaments-based superamphiphobic surfaces, during which the evaporation process is monitored by a camera. I perform the evaporation experiments in a humidity chamber, which allows regulating the humidity, and hence, the evaporation rate. The results demonstrate the importance of colloidal stability in determining the final supraparticle morphology, as the evaporation of non-stabilized dispersion droplets leads to an irregular buckled shape. The spherical supraparticles, which are obtained after stabilizing the dispersions, present the potential to control the range of ordering of ellipsoids by tuning their aspect ratio and/or the evaporation rate. This finding is further validated by drying simulations. The supraparticles composed of randomly packed ellipsoids tend to increase in porosity with increasing ellipsoid aspect ratio. Furthermore, the sphere-ellipsoid binary supraparticles show that the increased ordering of ellipsoids can be disrupted by the presence of spheres under the same evaporation conditions. My findings here highlight the influence of interparticle interactions, the particle shape and evaporation rate in determining the final morphology and structure of supraparticles. The conclusions drawn from varying all these variables could potentially inspire the fabrication of supraparticles with desired ordered structures for various applications.

Zusammenfassung

Wenn Flüssigkeiten mit dispergierten Kolloiden verdampfen, können die zurückbleibenden Kolloide komplexe Strukturen bilden, die für viele natürliche Phänomene und technische Anwendungen von Bedeutung sind. Die Verfügbarkeit von superamphiphoben Oberflächen eröffnet neue Möglichkeiten zur Untersuchung der Strukturbildung in verdampfenden Dispersionen, die zur Herstellung von Suprapartikeln führen. Suprapartikel sind Gebilde, die durch die gezielte Selbstorganisation kleinerer Nano- oder Mikropartikel entstehen. Die Materialeigenschaften von Suprapartikeln lassen sich durch Anpassung der Form und der Chemie ihrer Bausteine sowie der Verdampfungsbedingungen steuern. Bislang waren kugelförmige Kolloide die herkömmliche Wahl der Bausteine, so dass die Verwendung anisotroper Kolloide zur Steuerung der Struktur der Suprapartikel weitgehend unerforscht blieb. Die Selbstorganisation ellipsoider Partikel ist zum Beispiel besonders interessant, da sie eine breite Palette geordneter Endstrukturen bietet. Es fehlen jedoch systematische Experimente, die den Einfluss des Ellipsoid-Aspektverhältnisses, der Kombination von Ellipsoiden mit Kugeln und der Verdampfungsrate auf die endgültige Struktur der Suprapartikel zeigen. In dieser Arbeit versuche ich, diese offenen Fragen zu beantworten, indem ich die Strukturbildung von verdampfungsinduzierten Suprapartikeln, die aus Polystyrol-Ellipsoiden und/oder -Kugeln bestehen, untersuche. Dazu bilde ich Suprapartikel, indem ich wässrige Dispersionstropfen von Ellipsoiden und/oder Kugeln auf superamphiphoben Oberflächen auf Basis von Silikon-Nanofilamenten verdampfe, wobei der Verdampfungsprozess mit einer Kamera überwacht wird. Ich führe die Verdunstungsexperimente in einer Feuchtekammer durch, die es ermöglicht, die Luftfeuchtigkeit und damit die Verdunstungsrate zu regulieren. Die Ergebnisse zeigen, wie wichtig die kolloidale Stabilität für die endgültige Morphologie

der Suprapartikel ist, da die Verdampfung von nicht ausreichend stabilisierten Dispersionströpfchen zu einer unregelmäßigen, eingeknickten Form führt. Die sphärischen Suprapartikel, die nach der Stabilisierung der Dispersionen erhalten werden, bieten das Potenzial, den die Anordnung der Ellipsoide durch Abstimmung ihres Aspektverhältnisses und/oder der Verdampfungsrate zu kontrollieren. Dieses experimentelle Ergebnis wird durch Trocknungssimulationen bestätigt. Die Suprapartikel, aus zufällig gepackten Ellipsoiden weisen mit zunehmendem Ellipsoid-Aspektverhältnis eine zunehmende Porosität auf. Darüber hinaus zeigen die binären Kugel-Ellipsoid-Suprapartikel, dass die erhöhte Ordnung der Ellipsoide durch die Anwesenheit von Kugeln unter denselben Verdampfungsbedingungen gestört werden kann. Meine Ergebnisse verdeutlichen den Einfluss der Wechselwirkungen zwischen den Partikeln, der Partikelform und der Verdampfungsrate auf die endgültige Morphologie und Struktur der Suprapartikel. Die Schlussfolgerungen, die aus der Variation all dieser Variablen gezogen werden, könnten die Herstellung von Suprapartikeln mit gewünschten geordneten Strukturen für verschiedene Anwendungen inspirieren.

Contents

Chapter 1

Introduction

1.1 Motivation and Outline

The last decades demonstrated many breakthroughs in making nanoparticles with a wide range of chemical compositions, controlled sizes, and defined morphologies.[1] Due to their superior properties such as high specific surface area, quantum effects, or catalytic activity, nanoparticles became invaluable in various areas of science and technology.[1;2] Going one step further would be to assemble nanoparticles into larger and more complex entities, such as supraparticles. By assembling nanoparticles, supraparticles reduce the hazards associated with the high mobility and nonspecific surface activity of primary nanoparticle building blocks.[3] Instead of the chemical methods required to synthesize nanoparticles, supraparticles can be made using physical methods based on solvent drying, which are easier to control.

The superparticulate nature, i.e., combining different nanoscale or colloidal building blocks into a single object, brings enhanced functionality.[1] Usually due to a distinct structural arrangement or interactions within close proximity, supraparticles might show emergent properties exceeding the functionalities of its building blocks.[1] Therefore, they are considered as a multifunctional material platform in various applications of science and technology.

In order to realize functional supraparticles, we need to gain control over the assembly process, which is directly dependent on the interactions between the constituent colloids and the process conditions.[1;4] Supraparticles offer a wide range of building blocks of different sizes, chemistries, and shapes, all of which are important handles to control structure formation.[1;5] Recently, many possibilities of making anisotropic colloids have been demonstrated.[6] Assembling shape anisotropic colloids under spherical confinement into supraparticles provides the opportunity to tune the colloidal interactions via shape-induced interface deformations.[7;8] Therefore, nonspherical colloids are promising building blocks for realizing unique superparticulate assemblies which otherwise cannot be achieved with spherical colloids.[8]

The primary goal of this thesis is to understand the structure formation in supraparticles composed of ellipsoids and sphere-ellipsoid mixtures under varying ellipsoid aspect ratio and evaporation conditions. In this first chapter, I will introduce colloids and discuss about evaporating colloidal dispersions on solid substrates. Then, I will define supraparticles and talk about the characteristics of supraparticle fabrication methods. Later, I will give some examples from the literature which showcase the structure formation in supraparticles and their functionalities. Finally, I will present the gap of knowledge and the systematic experiments I have been doing to answer some of the open questions regarding the effect of primary colloid shape and of the evaporation rate on the final supraparticle structure. In Chapter 2, I will introduce the experimental methods to prepare the superamphiphobic surfaces, the ellipsoidal colloids, the supraparticles and the associated characterization methods. In Chapter 3, I will discuss results regarding supraparticles that show a buckled morphology under various conditions, such as varying colloid shape, evaporation rate and initial colloid volume fraction. Following this, in Chapter 4, I will present a facile method to prevent buckling and successively show the importance of evaporation rate for buckling. The orientational ordering of ellipsoids on the surface as well as in the interior of spherical supraparticles will then be examined. Lastly, in Chapter 5, I will talk about the surface and interior ordering of ellipsoids for sphere-ellipsoid binary supraparticles with a spherical morphology. While doing so, the influence of parameters such as ellipsoid aspect ratio, evaporation rate, and ellipsoid to sphere volume ratio are investigated. Finally, I will give a summary of the results and a prospect for future studies.

My research work discussed in Chapter 3-5 have either been already published in a scientific journal or is currently under review as follows:

- Melis Yetkin, Yashraj M. Wani, Kritika Kritika, Michael P. Howard, Michael Kappl, Hans-Jürgen Butt, and Arash Nikoubashman. Structure formation in supraparticles composed of spherical and elongated particles. *Langmuir*, 40(1):1096-1108, 2024.

- Melis Yetkin, Yashraj M. Wani, Arash Nikoubashman, Hans-Jürgen Butt, and Michael Kappl. Tuning the morphology and structure of supraparticles composed of ellipsoids. (*currently under review*)

1.2 Colloids

A dispersion is a two-phase system, which consists of grains or droplets of one phase in a matrix of the other phase.[9] Therefore, a dispersion is uniform on the macroscopic scale, but not on the microscopic scale. Colloids refer to dispersions, in which one phase has dimensions roughly between 1 nm to 1 μm.[9;5] Colloidal particles can be found in a broad range of materials, such as minerals, clays, ceramics, metals, semiconductors, and polymers. They have long been used in various industrial applications, including paints, food, cosmetics, rheological fluids, and coatings.[5] The term "nanoparticles" are often used in today's literature in analogy to colloids. The prefix "nano-" indicates a size range of 1 to 100 nm, where untypical electronic, magnetic, or optical properties may be observed.[9;10] Such properties are usually size-dependent due to electron confinement and are observed, for instance, in quantum dots and nanocrystals.[5]

Colloidal systems are typically dominated by interfacial effects instead of bulk properties. Due to the high specific surface area of colloids, their behaviour is determined by surface properties rather than gravity.[9] Colloids are therefore the choice of material for many interface-related technologies, e.g., wetting, sensing, filtering, as electrode materials in catalysis.[5]

Colloids often assemble into larger entities and show collective behavior.[10;5] For instance, they can form crystals and other phases of matter observed in atomic and molecular systems.[10] For this reason, colloids have been utilized as "model atoms"[11] or "big atoms"[12] to study physics of condensed matter and materials science.[10;5] However, colloids show some interesting features, e.g., collective behaviour, that are not observed at the atomic scale. The attraction between the colloidal particles can be much shorter ranged (relative to their size) compared to that of atoms. This makes entropy and hydrodynamics determine the rate of transitions between structures, instead of energy barriers as is the case for atomic systems.[10]

Colloids can be considered as "building blocks" that tend to self-assemble into complex structures with hierarchical order.[5] Most colloids can now be synthesized in the desired size, shape and surface chemistry in macroscopic quantities.[5;6] Change in particle shape strongly alters the equilibrium phases.[10] For example, monodisperse spheres usually form hexagonal crystal packing (FCC and HCP), whereas monodisperse cubes yield simple cubic lattice symmetries.[5] Aside from nonspherical colloids, surface-functionalized, Janus, patchy or core-shell colloids can also be used to achieve architectural complexity [Figure 1.1].[5] Controlling the assembly process of such complex structures is essential to attain functional materials.

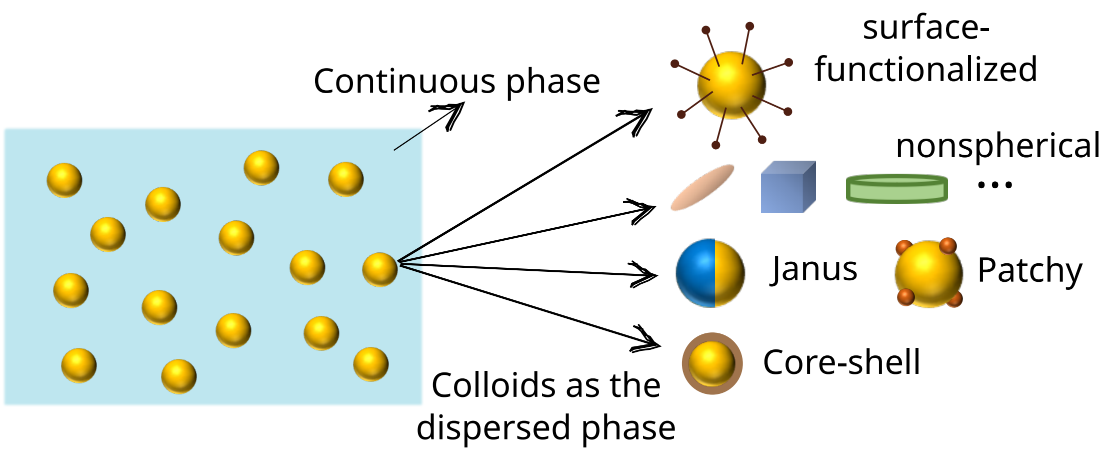

Figure 1.1: Schematics showing a dispersion, in which colloids are the dispersed phase and can exhibit architectural complexity, e.g., surface-functionalized, nonspherical, Janus, patchy, or core-shell.

The forces between colloids are related to their size, shape, and chemistry and directly determine the assembly process for a given dispersing medium.[5] The forces involved in colloidal assembly can be (i) repulsive, e.g., Coulomb interactions, dipolar interactions or steric stabilization, which prevent the spontaneous aggregation and flocculation of a colloidal dispersion, (ii) attractive, e.g., capillary forces, Van der Waals forces, depletion interactions or hydrodynamic coupling, which yield distinct assembled structures, and (iii) external forces, e.g., Brownian motion, gravitational forces or geometrical confinement, acting on individual colloids or colloidal clusters.[5;13] The final self-assembled structure is a direct consequence of the interplay between colloidal forces directed towards thermodynamic equilibrium, which is typically associated with the system's free energy minimum.[5;14] Nevertheless, external forces such as spherical confinement (as is the case for colloidal dispersion droplets) may drive the directed self-assembly of colloids into discrete structures beyond the thermodynamic free energy minimum.[14] In a nutshell, colloidal assembly is a complicated process, for which one cannot easily draw a clear guideline. Therefore, studying the structural evolution during colloidal assembly is necessary to realize functional materials with optimal performance.

1.3 Evaporation of Colloidal Dispersion Droplets

When colloidal dispersion droplets evaporate from a solid substrate, the volume of the droplet decreases and the packing density of the dispersed colloids increases, leading to the formation of a distinctive deposit in the contact region. The structure of this deposit depends on the wetting properties of the surface.[15] If the dispersion fully wets the substrate, a film is formed, which is important for many applications such as coating, thin colloidal films, and painting [Figure 1.2(a)].[16] In this case, the evaporation process is spatially symmetric and can be described by a single coordinate perpendicular to the substrate.[17;18] If an isolated dispersion droplet partially wets the substrate, the deposited colloids form a more complex structure, since the evaporation is no longer homogeneous as in the former case [Figure 1.2(b)].[19;20] In case the apparent contact angle between the droplet and substrate is below 90°, the drop edges become pinned to the substrate and more evaporation occurs at the periphery than in the center.[19;21;22] Due to contact line pinning, the evaporation of the droplets occurs at a constant contact radius rather than at a constant contact angle. The capillary flow of liquid from the centre of the droplet to the edge continuously enriches colloids at the periphery throughout evaporation. As a result, the colloids aggregate at the droplet edge to form doughnut-like or ring-like structures (so-called "coffee-ring effect").[19;23;24;25;26;27;28;29] The coffee-ring effect has been studied extensively due to its relevance in many applications including ink-jet printing,[30] chromatography,[31] functional coating,[32] and biochemical analysis.[33] The evaporation of dispersion droplets can also happen in a contact free environment, as is the case for infamous spray-drying [Figure 1.2(c)].[34;35;36] The evaporation of the free spherical droplet in this case is radially symmetric and hence can be described by one single coordinate.

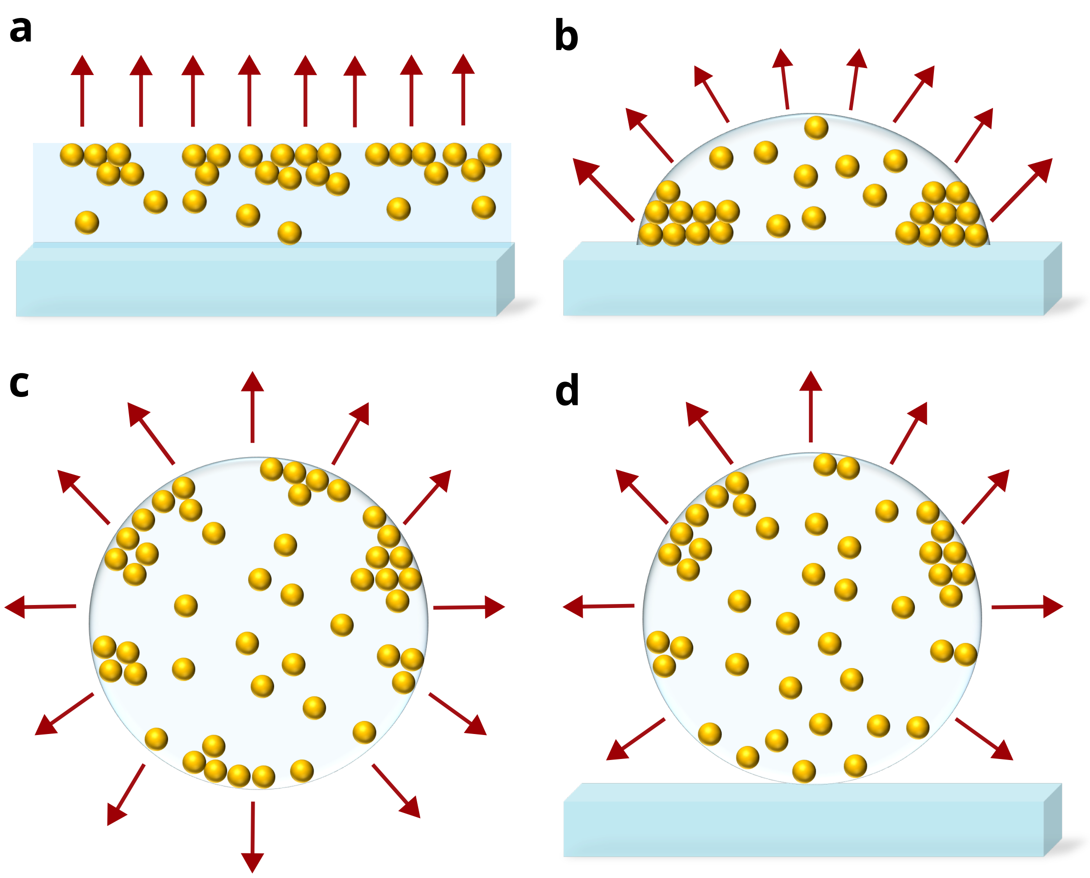

Figure 1.2: Schematic overview of drying dispersion geometries occurring on a solid surface or contact free. Evaporation of a) a horizontal film, b) a droplet on a partially wetted surface, c) a free droplet, and d) a droplet on a super-liquid-repellent surface.

Water and oil repellent surfaces, so-called superamphiphobic surfaces,[37;38] have become available over the last two decades. Droplets on superamphiphobic surfaces acquire a spherical morphology with contact angles larger than 150° and roll off angles smaller than 10° [Figure 1.2(d)]. As a result, evaporation is almost radially symmetric with a constant contact angle and the capillary flow, which leads to contact line pinning and coffee-ring formation for droplets evaporating on partially wetted surfaces, is suppressed. The use of superamphiphobic surfaces facilitates studying the evaporation-induced structure formation in colloidal deposits.

Evaporation of dispersion droplets is a complex, non-equilibrium transport process in confinement. Inside the spherical droplet, colloids diffuse due to Brownian motion. Throughout evaporation, the interface recedes at a rate, which is determined by the diffusion of solvent through its surrounding vapor or processing liquid.[39] For a water droplet evaporating at a constant contact angle, the volume $V^{2/3}$ decreases linearly with time as[40]

$$V^{2/3} = V_0^{2/3} - \alpha t \tag{1.1}$$

where V_0 is the initial volume of the droplet and α is the evaporation speed. Colloidal droplets evaporate mostly in the same manner, but with a slightly slower rate,[15] as colloids reduce the exposed surface area through which solvent can evaporate. The receding air-solvent interface creates an effective advection,[41] which can lead to a concentration gradient by accumulating the colloidal particles provided the drying is fast enough.

The balance between diffusion and advection is commonly characterized by a dimensionless quantity known as the Péclet number Pe. Péclet number can be defined as the ratio of the typical diffusion time, $\tau_d = R_0^2/D_0$, and the evaporation time, $\tau_{ev} = R_0/v_{ev}$, at the beginning of drying. Here, R_0 is the initial droplet radius, D_0 is the diffusion coefficient of the colloidal particles at infinite dilution, and v_{ev} is the initial speed of the receding droplet interface. The expression for

Péclet number can then be written as[17]

$$Pe = \frac{\tau_d}{\tau_{ev}} = \frac{v_{ev} R_0}{D_0} \quad (1.2)$$

When $Pe \leq 1$, the evaporation is considered as slow and concentration gradients can relax by diffusion. In contrast, when $Pe \gg 1$, the evaporation is considered fast and far from thermodynamic equilibrium. In this case, significant concentration gradients develop due to advection, which then might be arrested towards the end of evaporation, e.g., by jamming.[42] The Péclet number changes as drying proceeds. However, the initial Péclet numbers, that were calculated throughout this study, are useful in characterizing the drying regime of the droplets.

1.4 Supraparticles: Definition and Nomenclature

Evaporation of dispersion droplets may induce the assembly of smaller colloids into a larger and more complex entity, which can be termed supraparticles.[2] During the formation of supraparticles, the colloids assemble through weak, noncovalent interactions (e.g., van der Waals, hydrogen bonding, electrostatic interactions) or hard-particle (e.g., excluded volume) interactions, similar to supramolecular chemistry.[1;43;44] This directed self-assembly process includes multiple length-scales, associated with the solvent molecules (0.1-1 nm), the dispersed colloids (5-1000 nm), and the droplet (0.1-1mm). Moreover, several interfaces, i.e. between the solvent, colloids, substrate, and surrounding vapor phase, govern the assembly process.

The term supraparticle was first used in 1971 to describe the microstructures of particle aggregates in clay domains.[45] The term was not used in the field of colloidal science until 1995, where it was first used to describe bridging of TiO_2 to CdS particles through bifunctional mercaptocarboxylic acids.[46] In 1996, the term supraparticle was formally defined for the first time as the assembly of different types of colloid particles into ordered or multicomponent clusters, by Velev group.[47;48;49] Since then, the terms "superstructures",[50] "suprastructures",[51] "supraballs",[52;53] "supramolecular colloidal materials",[54] "colloidal Janus particles",[55] "colloidosomes",[56;57] or "supracolloids"[58;59] have been often used interchangeably to denote supraparticles. This non-existing common nomenclature in the field of particles creates difficulties in finding related literature and a clear definition.[1]

In their review article, Wintzheimer et al. determined some criteria to define supraparticles.[1] Accordingly, the term supraparticle requires assembling defined particles, which means using colloidally dispersed nano- or microparticles as the starting material. Supraparticles should be obtained in a dispersed form as colloid, powder or microcomposite, which distinguish them from the self-assembled nanoparticle arrangements that are infinitely extended in one, two, or three dimensions such as fibers, films, or colloidal crystals. In contrast to randomly agglomerated nanoparticles, supraparticles should have a defined average size, shape, or an internal structure. This thesis conforms such criteria and designates supraparticles as the assembly of primary nano- or microparticles (or building blocks) with a typical size from a few 10 μm to several 100 μm[2] [Figure 1.3].

The toolbox for creating supraparticles is quite broad. Multiple types of colloidal materials with a specific size, shape and chemistry, e.g., proteins,[60] semiconductors,[61] or magnetic colloids,[62] can be hierarchically assembled to form supraparticles with combined functionalities. Therefore, supraparticles are considered as promising materials for many different applications including catalysis,[2;63;64] drug delivery and encapsulation,[65] photonics,[66;67] and energy storage[68;69].

1.5 Supraparticle Fabrication Methods

Supraparticles can be fabricated using physical strategies that are easier to handle compared to the chemical strategies used for synthesizing nanoparticles. Common strategies for obtaining supraparticles in droplets can be can be divided into two broad categories as "wet self-assembly" (WSA) and "dry self-assembly" (DSA).[70] Both categories start with a liquid of primary particles, which are later dispersed into defined droplets. The particle concentration continuously increases, as the liquid evaporates, to finally form the consolidated supraparticles.[48]

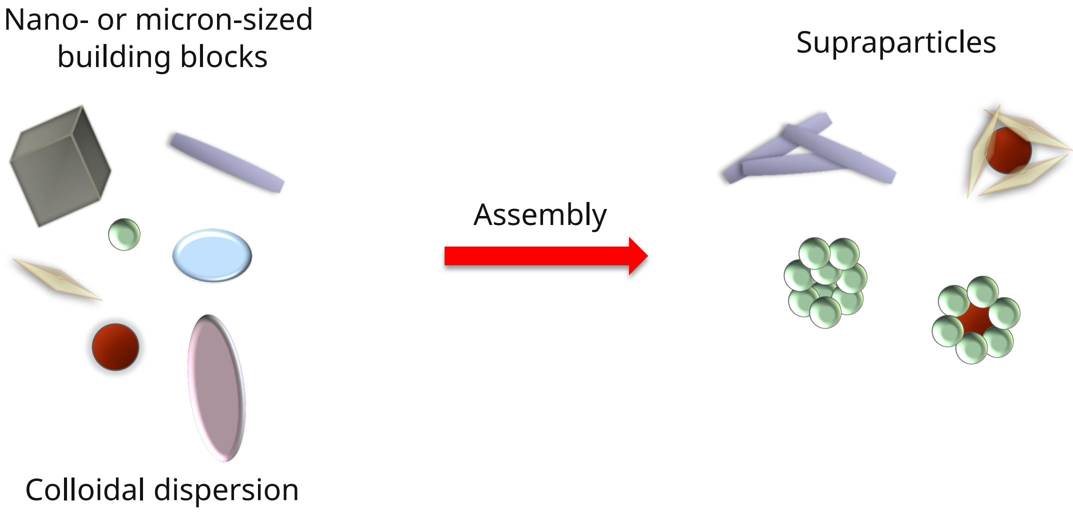

Figure 1.3: Supraparticles are formed through the self-assembly of colloidally dispersed nano- or micron-sized building blocks.

1.5.1 Wet self-assembly (WSA)

Wet self-assembly methods have been frequently used to form supraparticles from liquid–liquid interfaces. Emulsion droplets, suspended in another liquid, are commonly used as templates for obtaining the final solid supraparticle [Figure 1.4(a)]. Several techniques allow generating emulsion droplets of sizes ranging from nanometers to millimeters.[1;63] Electrospraying,[71] inkjet printing,[72] or droplet shear-off techniques[73] produce micro- to millimeter-sized droplets. Smaller micrometer-sized emulsion droplets can be obtained using membrane emulsification,[74] emulsification via high shear homogenizer, or microfluidics.[75] Miniemulsion techniques[76;77] are established to generate nanometer droplets. Oil-in-water emulsions were adopted to self-assemble hydrophobic Au nanoparticles[78;79] and CdSe quantum dots,[80] whereas water-in-oil emulsions were adopted to self-assemble hydrophilic PS and SiO_2 colloids[81] into various supraparticle structures. Different surfactants were used in such systems to stabilize the emulsion droplets. Velev et al. formed aqueous droplets of negatively charged PS microspheres in fluorinated oil without using any surfactants.[82] Water was removed from the suspended droplets by keeping the system in a sealed chamber that contained a desiccating agent, which led to the formation of crystalline porous supraparticles. The addition of surfactant further resulted with more complex supraparticles such as toroidal, doughnut-like assemblies. Manoharan et al. used surfactant-free Pickering emulsions stabilized by charged PS particles that adsorbed at liquid-liquid interface.[83] Removing oil generated capillary interactions that forced the particles into densely packed, symmetric clusters.

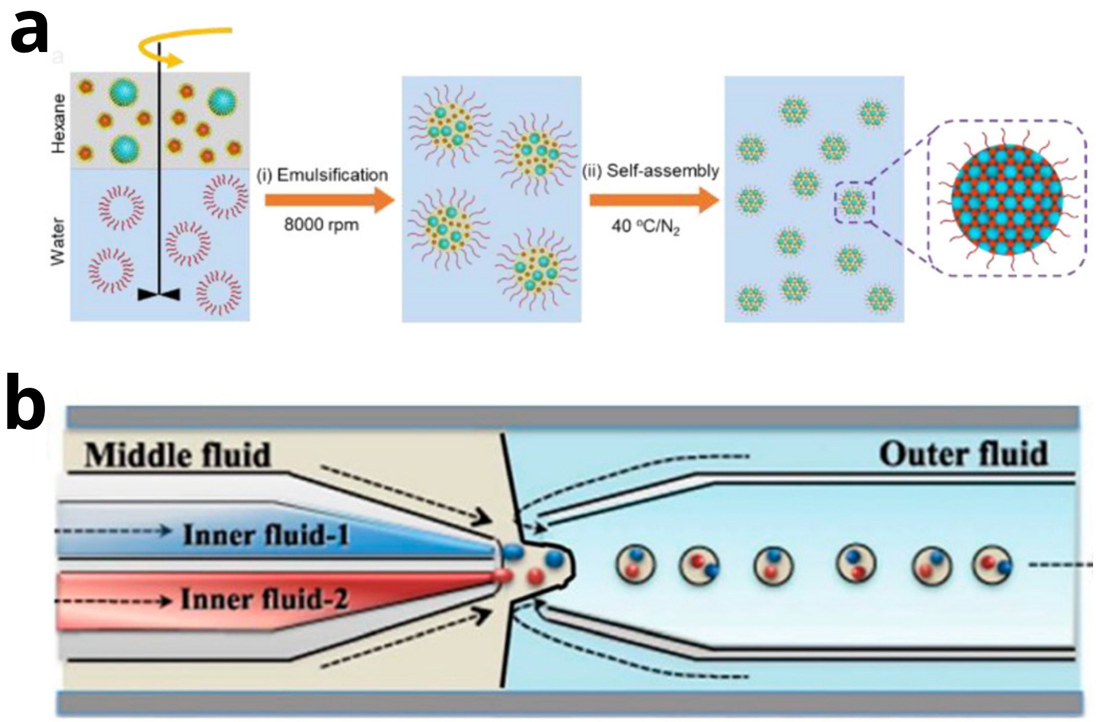

Figure 1.4: a) Schematic illustrating the binary supraparticles obtained by an oil-in-water emulsion assembly. Reprinted with permission from ref.[84] Copyright 2018 American Chemical Society. b) Schematic of a microfluidic capillary device for preparation of multiple component double emulsions. Reprinted with permission from ref.[85] Copyright 2012 The Royal Society of Chemistry.

Most emulsion techniques rely on high shear stresses when generating droplets, which might result with polydisperse droplets, and hence, polydisperse supraparticles. Microfluidics offer much better control over the emulsification process and enable the formation of highly monodisperse droplets, the proper adjustment of droplet size, and the design of more complex, multicompartment liquid droplets.[86;87;88;75;89] Therefore, microfluidics have become a strong method to produce monodisperse supraparticles with complex architectures. Typical microfluidic devices include polydimethylsiloxane-based devices with single or multiple liquid junctions in serial arrangement to produce homogeneous emulsion droplets or droplets with core-shell architectures.[90] Glass capillary-based devices with multiple coaxial flows are also available to fabricate multicompartment emulsions [Figure 1.4(b)].[85] Nisisako et al. synthesized monodisperse bicolored Janus particles by using a quartz glass microfluidic device.[91] To form bicolored droplets, two isobornyl acrylate streams - one dispersed with carbon black pigments (black) and the other one dispersed with titanium dioxide pigments (white) - were forced through a flow-focusing like geometry. These droplets were later polymerized into solid particles by thermal polymerization. Xu et al. produced spherical, disk or rod-shaped droplets by physically confining them in microfluidic channels that have different geometry.[92] These droplets were then photochemically and thermally solidified into particles of respective shapes. A disadvantage of microfluidics is the low throughput, which is typically limited to generating droplets in the lower milliliter per hour range.[93] The yield could be scaled up by increasing the number of outlets in parallel, however, this might lead to polydisperse droplets.

WSA approaches are suitable for large-scale production. However, they have certain drawbacks with regards to their dependence on additional processing liquids as well as limited control over the final supraparticle morphology.[2;70] The additional chemicals or processing liquids used during such processes need to be separated from the supraparticles and disposed of afterwards, which consume energy and harm the environment. Therefore, methods that reduce the use of such processing liquids, solvents, emulsifiers, or templates are more preferable.

1.5.2 Dry self-assembly (DSA)

In dry self-assembly methods, supraparticles are formed by evaporating droplets from liquid-air interfaces. DSA techniques avoid the use and removal of any processing chemical, and hence, the assembled structures can easily be collected without further processing.[70] Many studies used Leidenfrost levitation to make supraparticles in a contact free environment [Figure 1.5(a)].[94;95;96] As described by Leidenfrost in 1756, a water droplet on a very hot plate will be levitated above the surface instead of wetting it.[97] Provided that the plate is hot enough (typically above 150°C), the dispersion droplets do not boil, but levitate on their own vapor layer as long as there is enough solvent to feed them. As the solvent evaporates, the volume decreases and the particles consolidate into supraparticles.

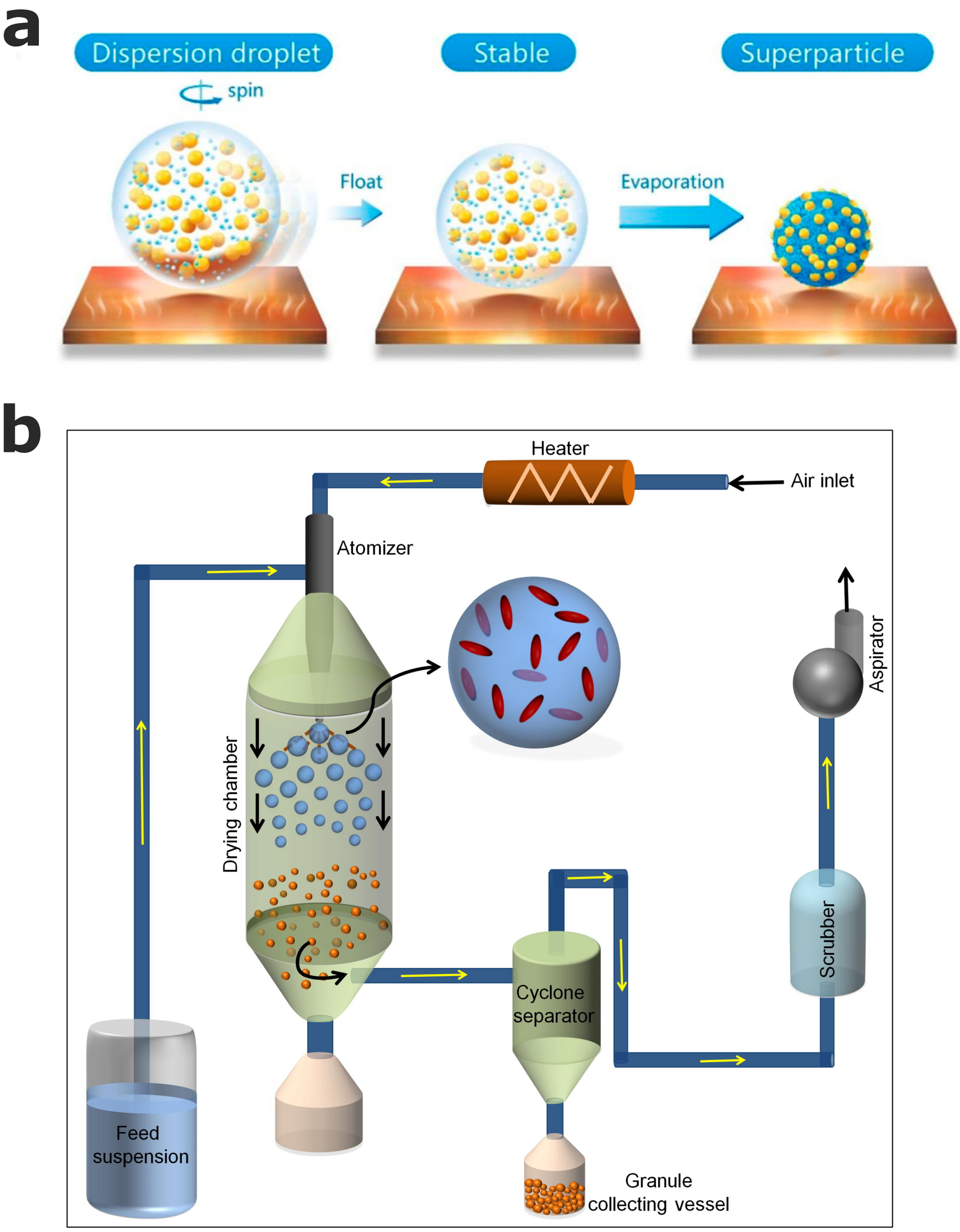

Figure 1.5: a) Schematic illustrating the supraparticle fabrication by Leidenfrost phenomenon. Reprinted with permission from ref.[96] Copyright 2022 American Chemical Society. b) Schematic showing laboratory scale spray-drying setup. Reprinted with permission from ref.[98] Copyright 2019 Elsevier.

Another DSA method which involves evaporating freely suspended droplets is spray-drying. Spray-drying is widely used in industry to create powders (e.g., instant coffee, milk powder) from solutions or suspensions. In a typical spray-drying process, an atomizer is used to convert the colloidal dispersion into small droplets, which are then carried into a hot zone by air, steam, or gas flow [Figure 1.5(b)].[99] Inside the hot zone (typically heated to 100°-200°C), the concentration of the particles in the droplet increases as the solvent evaporates, and the particles self-assemble due to attractive forces and possibly due to compression by capillary force, leading to the formation of supraparticles. The obtained supraparticles are collected with the help of a cyclone, a filter bag, or an electric field precipitator. Depending on the process parameters such as solid concentration, solvent type, evaporation rate, or spray geometry supraparticles of various structures can be fabricated.[1] The method is effective in producing multicomponent supraparticles with distinct physical characteristics. Examples include antimicrobially active raspberry-like supraparticles for antimicrobial activity,[100] hydrophobic-hydrophilic core-shell supraparticles for water filtration,[101] or shear stress indicator supraparticles with light emitting core and light absorbing shell.[102]

Both Leidenfrost levitation and spray-drying are are typically performed at high temperatures, where evaporation takes only a few seconds. The fast evaporation conditions complicate the control of the final supraparticle shape and the distribution of the colloidal particles inside the supraparticle.[96] Therefore, studying structure formation with these techniques in real time is quite difficult.

A significant DSA technique for obtaining supraparticles is to evaporate dispersion droplets dispensed on super-liquid-repellent surfaces, e.g., superhydrophobic or superamphiphobic surfaces. In contrast to Leidenfrost levitation and spray-drying, evaporation process on such surfaces can be carried out slowly under well-defined conditions, which allows to study the structure formation in detail. In the following Subchapter 1.6, important features of superhydrophobic and superamphiphobic surfaces and the formation of supraparticles on such surfaces will be addressed.

1.6 Supraparticle Fabrication on Super-Liquid-Repellent Surfaces

1.6.1 Characteristics of super-liquid-repellent surfaces

As already mentioned in Subchapter 1.3, the structure of the deposit on a solid surface is determined by its wetting properties. The wettability of a surface is typically characterized by two parameters–contact angle and contact angle hysteresis. The contact angle (CA) θ of a liquid on a solid surface [Figure 1.6(a)] depends on the interfacial tensions between the different phases and is determined by Young's equation as follows[103]

$$cos\theta = \frac{\gamma_{SV} - \gamma_{SL}}{\gamma_{LV}} \tag{1.3}$$

Here γ refers to the interfacial tension and S, L and V correspond to the solid, liquid and vapor phases, respectively. If the CA of a water droplet $\theta = 0°$, the liquid spreads on the surface completely and the surface is classified as superhydrophilic. The surface is considered as hydrophilic when $\theta<90°$ and hydrophobic when $\theta>90°$.[104]

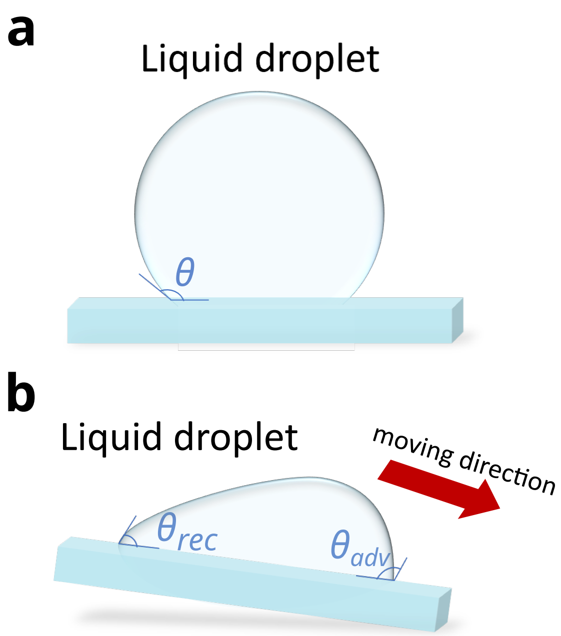

Figure 1.6: a) Schematic illustration of contact angle (θ) of a liquid droplet on a solid surface. b) Schematic illustration of a moving liquid droplet on a tilted surface with advancing (θ_{adv}) and receding (θ_{rec}) contact angles.

Most real surfaces are non-ideal, i.e., they are usually rough and heterogeneous. Therefore, surfaces are prone to showing contact angle hysteresis (CAH) [Figure 1.6(b)].[104] CAH is associated to the energy barriers that a liquid droplet must overcome during its movement along a solid surface, and thus measures the resistance to the droplet movement.[105] CAH is given by the difference between the advancing (θ_{adv}) and receding (θ_{rec}) contact angles on a surface. Lower solid-liquid interfacial area means lower resistance to droplet movement, and eventually lower CAH.

When a liquid droplet contacts a rough, textured surface, it can adapt two different configurations to minimize its overall free energy– the Wenzel state[106] or the Cassie-Baxter state[107]. In the Wenzel state, the droplet completely wets the surface within the apparent contact area by permeating into all the protrusions [Figure 1.7(a)]. In this state, the apparent contact angles can be determined using the Wenzel equation as[106]

$$cos\theta_{app} = R_{rough} cos\theta \tag{1.4}$$

Here R_{rough} is the roughness parameter, which is defined as the ratio between the actual and the projected surface area. Since R_{rough} is always larger or equal to unity (≥ 1), roughness strengthens both the wetting and non-wetting behavior of surfaces in the case of Wenzel state. In other words, for θ<90° surface roughness decreases θ_{app}, while for θ>90°, θ_{app} increases. As a result, low surface tension liquids, such as oils and alcohols, show very low contact angles in the Wenzel state.[108]

In the Cassie-Baxter state, however, the droplet does not fully wet the surface within the apparent contact area [Figure 1.7(b)]. Instead, air pockets remain trapped between the droplet and surface protrusions.[109;104] θ_{app} in this state can be found by the following relation[107]

$$cos\theta_{app} = f_{SL}cos\theta + f_{LV}cos\pi \tag{1.5}$$

Here f_{SL} and f_{LV} represent the area fraction of the solid-liquid interface and the liquid-air interface, respectively. Cassie-Baxter state can lead to $\theta_{app} \gg 90°$ for θ>90° as well as θ<90°, when the solid-liquid area fraction is sufficiently low and the liquid-air area fraction is sufficiently high.[108] Compared to the Wenzel state, the Cassie-Baxter state leads to very high CA even for low surface tension liquids. Additionally, the Cassie-Baxter state results in a lower CAH than the Wenzel state due to the lower solid-liquid area fraction. Therefore, the Cassie-Baxter state is favored when designing super-liquid-repellent surfaces, e.g., superhydrophobic and superamphiphobic surfaces.

If water droplets on a surface show CA>150° and CAH<5°, then it is considered a superhydrophobic surface.[108] A well-known example from nature is the "lotus-effect"[110] which is observed with various plant leaves [Figure 1.8(a-b)]. The water droplets placed on these leaves are in contact with hydrophobic spikes and can roll off easily, cleaning the surface from dirt particles. Such natural superhydrophobic surfaces inspired scientists to fabricate artificial surfaces mimicking the chemical hydrophobicity and the surface texture on the micro- or nano-scale. The appropriate surface chemistry is usually ensured by the choice of low surface energy materials, e.g., fluorinated and perfluorinated materials, as they display high contact angles.[108] The micro- and nano-scale surface roughness can be provided

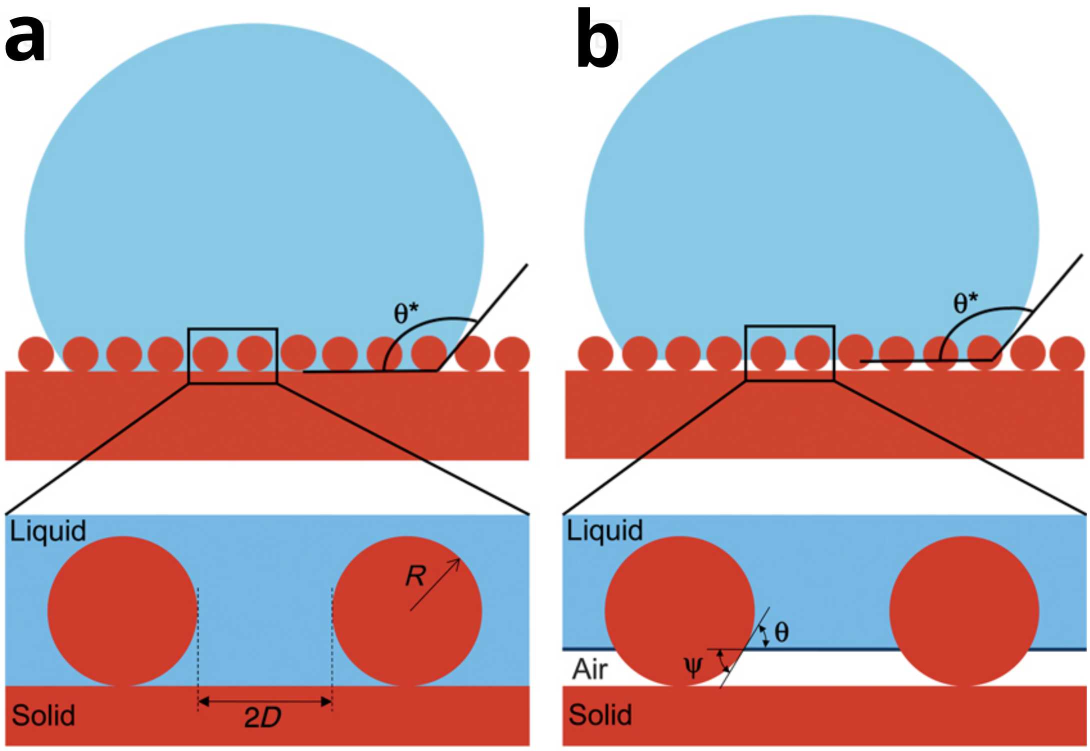

Figure 1.7: Schematic of a liquid droplet in a) the Wenzel state and b) the Cassie–Baxter state, on a textured solid surface. Reprinted with permission from ref.[105] Copyright 2013 Materials Research Society.

by several methods such as lithography, etching, nanoimprinting, and deposition (e.g., spin coating, spray coating, electrochemical deposition and chemical vapor deposition).[111] For instance, Shieh at al.[112] fabricated a superhydrophobic silicone surface, which provided surface roughness through nanopillars and nanograss features. E-beam lithography and dry etching were used to produce nanopillars, followed by hydrogen plasma etching to form the nanograss on the surface. The surface was later hydrophobized by CHF_3 plasma. Gu et al.[113] electrochemically deposited a highly porous coral-like silver film on commercial copper alloy substrates. They further functionalized the surface with an aliphatic thiol to achieve CA>150° and CAH<2°.

If liquid droplets with low surface tension, such as oils, alcohols or other organic solvents, on a surface show CA>150° and CAH<5°, the surface is considered superoleophobic.[108] There are almost no superoleophobic surfaces found in nature.[108] A rare natural oleophobic surface is found on the skin of springtails [Figure 1.8(c)].[114] Springtail skin shows a hierarchical structure, where secondary granules are superimposed on primary granules. Primary granules exhibit a rhombic or hexagonal comb pattern combined with bristles and feathered hairs. Meanwhile, the secondary granules display re-entrant texture, which makes the skin oleophobic.

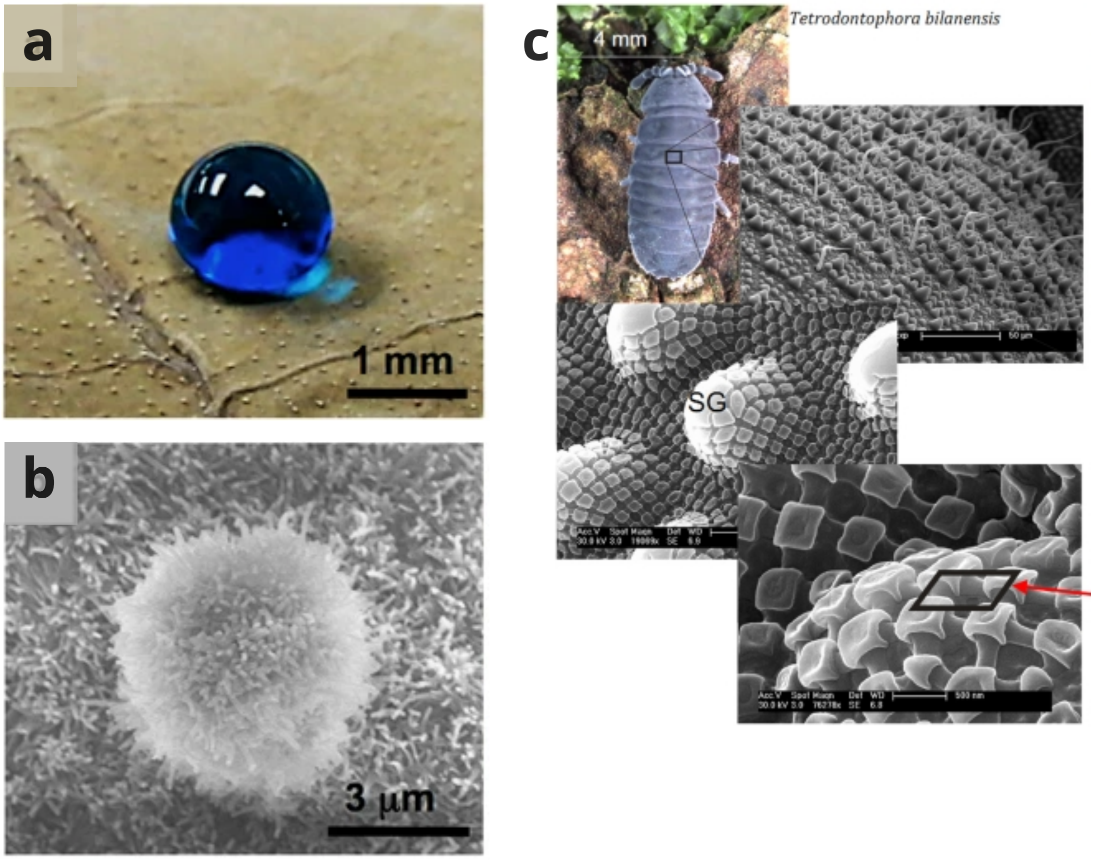

Figure 1.8: The super-liquid-repellent surfaces in nature. a) A water droplet (blue) assuming high contact angle on a lotus leaf. b) SEM image of a lotus leaf showing its rough, hierarchical texture. (a,b) Reprinted with permission from ref.[108] Copyright 2014 Nature Publishing Group. c) A photo and SEM images of the skin of springtails, showing hierarchical structure with re-entrant texture. Reprinted with permission from ref.[114]. Copyright 2011 PLOS One.

Most surfaces that can repel lower surface tension liquids (for example, 32 mN m^{-1} for olive oil, 27.5 mN m^{-1} for hexadecane and 23.8 mN m^{-1} for decane)[115] can typically also repel higher surface tension liquids, such as water (72.8 mN m^{-1}). Such surfaces that display both superhydrophobicity and superoleophobicity are called superamphiphobic or superomniphobic.[108] Surface chemistry and roughness alone are not sufficient to make superamphiphobic surfaces. Re-entrant texture in the form of "overhangs", as already observed on the surfaces of lotus leaf and springtail skin, play a significant role in the design of superamphiphobic surfaces.[109;116] This is because low surface tension liquids (θ<90°) cannot display a stable Cassie-Baxter state unless the surface possesses overhang structures, providing a convex curvature.[109;116;108] Most liquid-repellent surfaces in nature show more than one length scale of texture, which typically comprise of a finer length scale texture overlaying a coarser one [Figure 1.9].[117;108] As a result, air is entrapped at multiple length scales instead of a single length scale texture. Such a hierarchically structured surface ensures low solid-liquid contact area, and hence, a significantly low CAH.[117;108] Consequently, hierarchically structured surfaces with overhang structures enable the Cassie-Baxter state for low surface tension liquids and are optimal for making superamphiphobic surfaces.

Figure 1.9: Schematics depicting a liquid droplet in the Cassie–Baxter state a) on a coarser textured surface, b) a finer textured surface, and c) a hierarchically textured surface. Reprinted with permission from ref.[105] Copyright 2013 Materials Research Society.

With an understanding of critical design parameters, superamphiphobic surfaces have been engineered using various materials ranging from metals to polymers and surface coatings ranging from perfluoralkyl silanes to perfluoroalkyl polyhedral oligomeric silsesquioxanes.[105] Fujii et al.[118] developed a hierarchical dual pillar surface by first depositing discrete pillars of aluminum-niobium (Al-Nb) alloy on a scalloped aluminum substrate via oblique angle magnetron sputtering, followed by anodizing the deposited pillars to form a nanoporous oxide layer. This hierarchically textured surface was later coated with a fluoroalkyl phosphate layer to achieve superamphiphobicity. Golovin et al.[119] fabricated a hierarchically textured and transparent superamphiphobic surface by spray coating poly(dimethylsiloxane) (PDMS)—fluorodecyl POSS microparticles onto transparent PDMS pillars, which were built using the standard imprint lithography. Deng et al.[120] produced a candle soot morphology covered with a silica shell using chemical vapor deposition of tetraethoxysilane, catalyzed by ammonia. After calcination at high temperatures and subsequent functionalization with a fluorinated silane, the surfaces were transparent and superamphiphobic for different liquids, including peanut oil, olive oil, hexadecane and tetradecane.

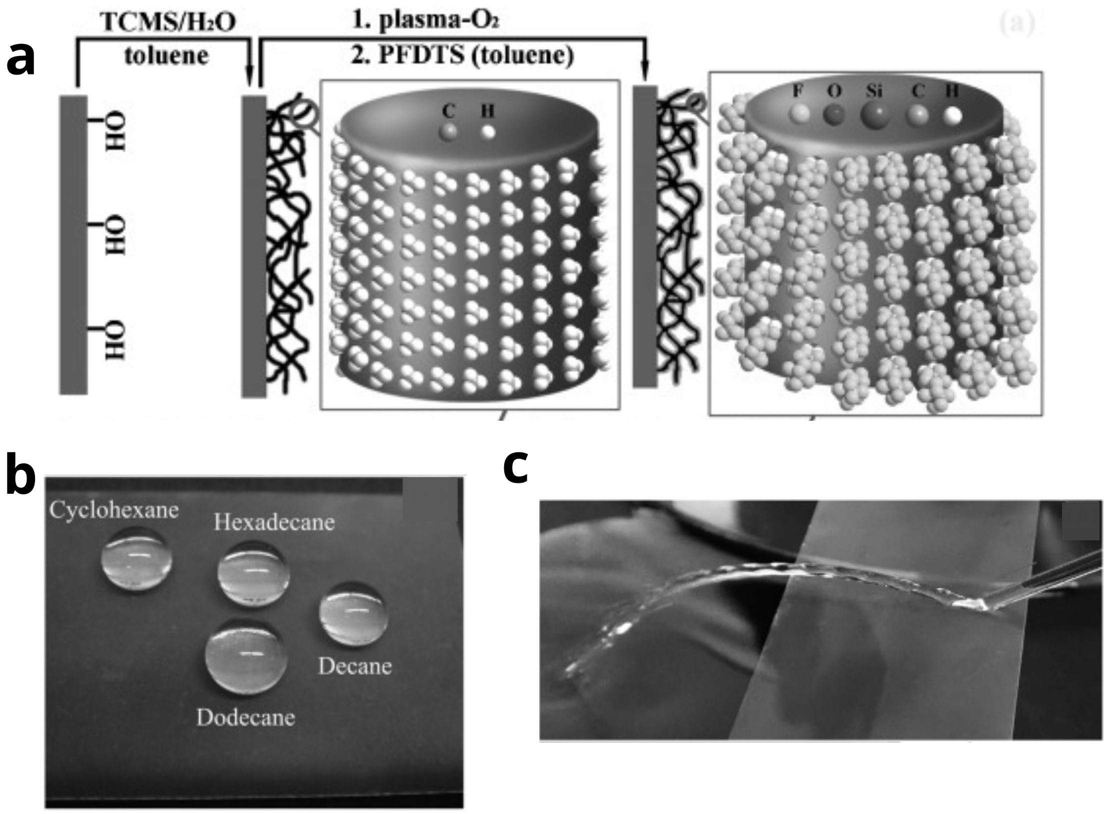

Figure 1.10: a) Schematic showing the growth of silicone nanofilaments onto glass slides upon hydrolysis and condensation of TCMS and subsequent modification with PFDTS. Images of nanofilaments-coated glass slides b) with droplets of various nonpolar liquids and c) with a jet of toluene bouncing off. Reprinted with permission from ref.[115] Copyright 2011 WILEY-VCH Verlag GmbH & Co.

The silicone nanofilaments superamphiphobic surfaces used in this thesis were developed by Zhang and Seeger [Figure 1.10(a)].[115] The silicone nanofilaments were grown onto glass slides upon hydrolysis and condensation of trichloromethylsilane (TCMS) in toluene. The random growth of nanofilaments created a rough topography on the surface. The nanofilaments carried methyl groups on their surface, which decreased the surface tension. At this stage the surfaces were superhydrophobic, but superoleophilic. The nanofilaments were further activated with oxygen plasma to convert the hydrophobic methyl groups into hydrophilic hydroxy groups while keeping the silicone skeleton intact. After the oxygen plasma treatment, the surfaces became superhydrophilic and superoleophilic. These surfaces were modified by immersing them in dry toluene, which contained 1H,1H,2H,2H-perfluorodecyltrichlorosilane (PFDTS). The PFDTS molecules anchored onto the hydroxy groups so that the nanofilament surface became superoleophobic. These surfaces showed high CA and ultra-low sliding angles (SA) for a variety of nonpolar liquids (of 5 μL volume), such as mineral oil (γ=32 mN m^{-1}, CA=172.2°, SA=1.2°), toluene (γ=28.4 mN m^{-1}, CA=168.4°, SA=2.5°), hexadecane (γ=27.5 mN m^{-1}, CA=174.4°, SA=2.0°), and decane (γ=23.8 mN m^{-1}, CA=162.5°, SA=5.3°) [Figure 1.10(b-c)]. The water concentration in toluene during TCMS coating was reported to highly influence the CA and the SA of hexadecane. For this reason, when growing nanofilaments I used toluene that contained around 166 ppm water, as this value provided good wetting properties.[115]

Super-liquid-repellent surfaces are suitable candidates for many applications, such as self-cleaning, antifouling, corrosion resistance, and chemical shielding.[105;121;122] In recent years, such surfaces have also been utilized as templates for the evaporation-induced assembly of colloids. The following Subsection 1.6.2 will provide examples where superhydrophobic and superamphiphobic surfaces are used to fabricate supraparticles.

1.6.2 A DSA method: Supraparticle formation on super-liquid-repellent surfaces

As I already discussed so far, supraparticles can be produced using physical methods such as emulsion evaporation, Leidenfrost levitation and spray-drying. Another interesting method is to evaporate colloidal dispersion droplets on super-liquid-repellent surfaces, which brings certain advantages. Utilizing these surfaces removes the need of using and removing a second phase, e.g., an oil phase. This makes the method environment-friendly, as it reduces organic pollution and saves materials and energy.[2;70] Due to the low solid-liquid interfacial area and low adhesion, the supraparticles can be easily collected from the substrates.[70] Most importantly, the method allows altering the evaporation conditions and the choice of colloidal dispersions. As a result, it becomes convenient to design complex supraparticles and to study their structure formation during evaporation [Figure 1.11].

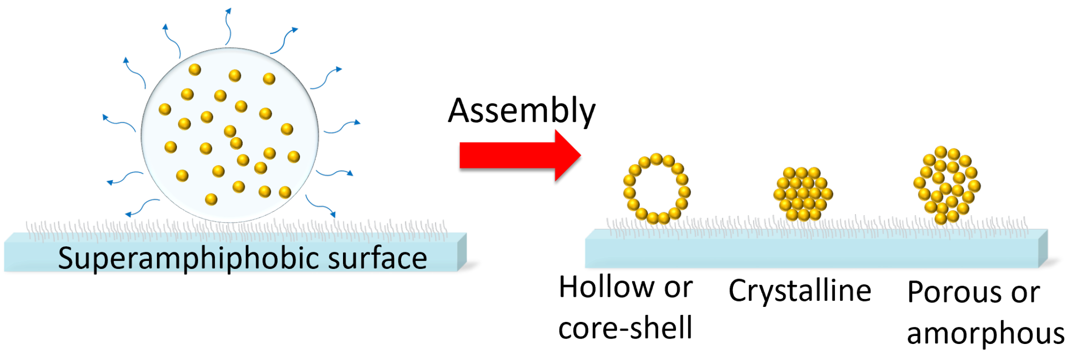

Figure 1.11: Schematic illustrating supraparticle formation on superamphiphobic surface. The evaporation of dispersion droplets is almost radially symmetric and might lead to supraparticles of various structures, e.g., hollow, core-shell, crystalline, porous.

Evaporation of aqueous droplets on superhydrophobic surfaces is almost symmetric, as θ_{app}>150° with a small solid-liquid contact area, leading to spherical droplet shape.[2] Deviation from this spherical shape can occur due to gravity, which can be characterized by a dimensionless Bond number Bo as[123]

$$Bo = \frac{\Delta\rho g r^2}{\gamma} \tag{1.6}$$

Herein, $\Delta\rho$ is the difference in the densities of the droplet and its surroundings, g= 9.81 m/s^2 is the acceleration of gravity and r is the characteristic dimension. When the diameter of the droplet approaches the capillary length, $\kappa = (\gamma/g\rho)^{1/2}$, the sphericity of the droplet starts distorting.[2] For water κ = 2.7 mm, therefore, for droplets much smaller than this value, the effect of gravity on shape will be negligible. Rastogi et al.[123] fabricated doughnut-shape supraparticles by evaporating aqueous silica suspension droplets on superhydrophobic substrates. Initially, the droplets assumed a near-spherical shape showing high contact angles on the surface. As the evaporation proceeded, the droplets showed shape transitions depending on the initial particle volume fraction and microsphere diameter. The pinning that facilitated the shape transitions was a result of the internal formation of a dense particle structure at the bottom of the droplets. They further fabricated spherical patchy magnetic supraparticles by evaporating mixtures of latex and magnetic particles, while applying magnetic fields to certain regions. Seyfert et al.[124] obtained a variety of supraparticles by evaporating aqueous droplets on a superhydrophobic surface patterned with fractal-like microstructures, which dramatically reduced the solid-liquid contact area. Depending on the initial particle concentration, pancake-shape clusters engulfing the fractal-like micropillars, buckled clusters, or unbuckled 3D spheroids with smooth surfaces were formed. Zhou et al.[125] tuned the shape of photonic crystal supraparticles from microbeads to microwells to microellipsoids by changing the three-phase contact line behaviour of colloidal droplets on superhydrophobic surfaces during evaporation. The dynamic behaviour of the contact line, i.e., continuous pinning or anisometric pinning, was modified by using colloidal droplets of ethanol-water mixture, which altered the surface tension. The anisometric pinning of the three-phase contact line led to anisometric photonic crystals.

Superhydrophobic surfaces restrict the use of nonpolar liquids when creating supraparticles, since nonpolar liquids cannot remain in the Cassie-Baxter state and impale into the superhydrophobic surface.[2] Superamphiphobic surfaces overcome this limitation, as they are also repellent to nonpolar liquids, surfactant, or protein solutions. Droplets on such surfaces acquire θ_{app}>150°, SA<10°, while the interfacial area between the liquid and solid is extremely small ($\ll V^{2/3}$, where V is the droplet volume).[37;105;116] Additionally, superamphiphobic surfaces usually have a highly porous structure, which allows the liquid to evaporate also through the substrate, leading to almost radially symmetric evaporation [Figure 1.12].[2] The method suppresses contact line pinning and hence the coffee-ring effect, as well as temperature-induced Marangoni flow inside the droplet.[127] Many studies illustrated that supraparticles of various sizes, compositions, and architectures can be produced by evaporating droplets on superamphiphobic surfaces. Wooh et al.[126] fabricated multicomponent spherical mesoporous supraparticles of vari-

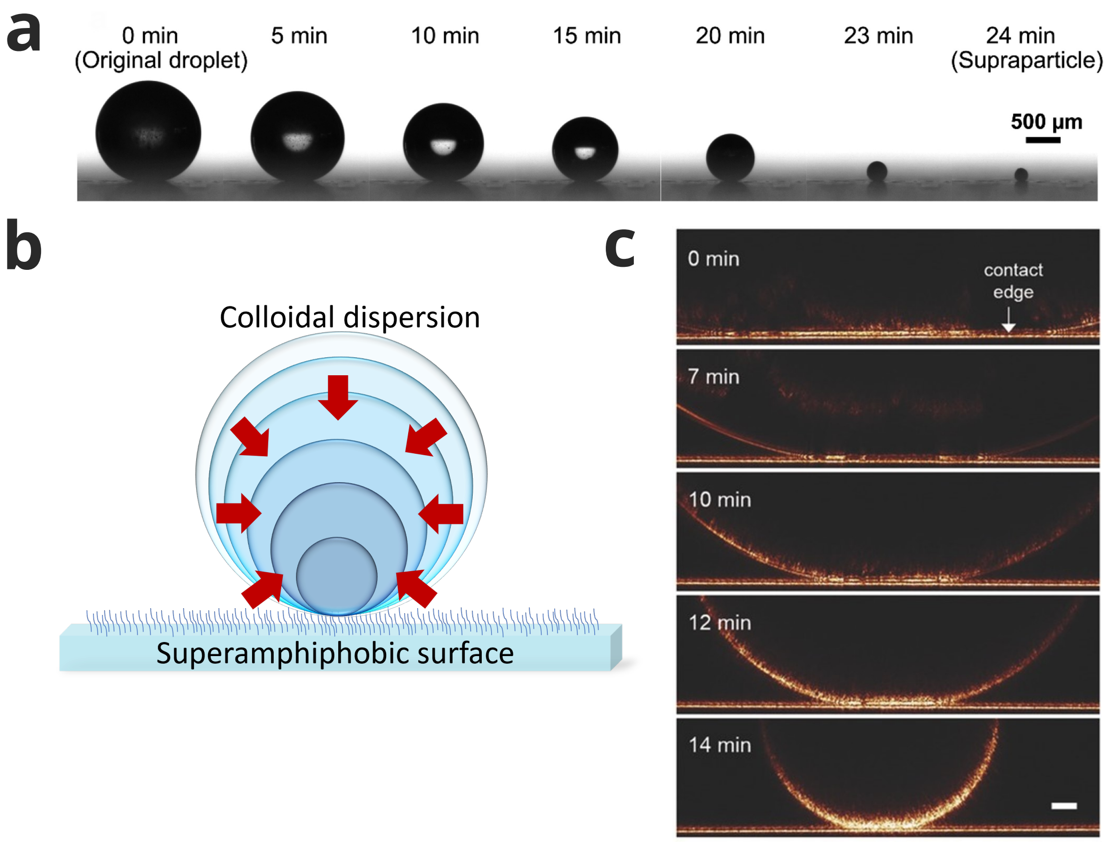

Figure 1.12: a) Images from an evaporation experiment of a colloidal dispersion droplet on a superamphiphobic surface. Reprinted with permission from ref.[2] Copyright 2019 American Chemical Society. b) Schematic showing the evaporation of the colloidal dispersion droplet on the superamphiphobic surface with moving contact line, eventually forming the supraparticle. c) Confocal microscopy images showing the evaporation of an aqueous dispersion droplet on a superamphiphobic surface. The scale bar is 20 μm. Reprinted with permission from ref.[126] Copyright 2015 WILEY-VCH Verlag GmbH & Co.

ous metal oxides such as TiO_2/SnO_2 and TiO_2/ZnO by using superamphiphobic surfaces. They further formulated SnO_2/TiO_2 core-shell supraparticles by sequentially drying nanoparticle dispersions of SnO_2 and TiO_2. Mano et al.[128] synthesized spherical PLGA particles for drug encapsulation by evaporating drops of PLGA/ciprofloxacin suspensions in dioxane on a superamphiphobic surface showing that the surface is suitable for solvents of any polarity. Tan et al.[127] studied the evaporation of an ouzo droplet (a transparent mixture of water, ethanol, and trans-anethole) on a superamphiphobic surface. As the ethanol evaporated, oil microdroplets formed at the top of the droplet and at later stages of evaporation an oil shell formed around the droplet. They later showed the formation of various multicomponent porous supraparticles ($TiO_2/SiO_2/Fe_3O_4$) by evaporating colloidal ouzo droplets.[129]

1.7 Structure Formation in Supraparticles

Fabricating supraparticles require assembling colloidal objects at mesoscale. Controlling the size, shape, and structure formation during the assembly process is essential in governing the material properties of supraparticles, such as photonic band gap, porosity, and mechanical strength.[130] Therefore, various fields of science and technology, ranging from soft matter physics to powder technology and pharmaceutical and food sciences, have aimed to gain control over the structure formation in such complex entities.[1] Key to controlling the supraparticle structure is through the choice of the building blocks and through engineering the kinetics of the assembly process.[1;5]

The choice of colloidal building blocks ranges from nanometer-sized quantum dots[80] or metal organic frameworks[131] to micrometer-sized polystyrene (PS) particles[15], with different shapes and chemistries. Hence, the interactions between the building blocks are equally broad and play a significant role in determining the characteristics of supraparticles. Sekido et al.[130] created supraparticles on superamphiphobic surfaces from aqueous dispersions of PS microparticles carrying a pH-responsive group. Particle assembly of supraparticles, e.g., either ordered or disordered particle assembly, was controlled by tuning the pH of the dispersion. When the dispersion droplets were dried at pH=3, spherical supraparticles with densely packed ordered structures were obtained, because at this pH the colloids were well-dispersed due to the positively charged responsive group leading to electrosteric repulsion. On the other hand, at pH=10 the colloids became hydrophobic by deprotonation and formed aggregates due to the increased hydrophobic attraction between particles. Consequently, at pH=10 more oblate supraparticles with disordered structures were formed. Binary mixtures of apolar gold nanoparticles were self-assembled into Janus or core-shell supraparticles depending on the surfactant used to stabilize the evaporating oil droplets.[79] The surfactant that provided higher repulsive interparticle potentials formed core-shell, whereas the one that provided a lower repulsive interparticle potential formed

Janus supraparticles as it provided earlier agglomeration. A pronounced variation of supraparticle shape was shown by evaporating aqueous droplets of fumed silica containing different concentrations of electrolyte from a superhydrophobic substrate.[132] As the ionic strength increased, the electrostatic repulsion between the silica particles decreased and hence there was a higher tendency for agglomeration, which led to a thicker shell formation at the evaporation front. This stiff silica shell could not shrink isotropically and folded into an elongated anisometric final shape beyond a threshold salt concentration. Similarly, Liu et al.[4] altered the electrostatic repulsion and van der Waals attraction forces between the colloids, which in turn, determined the final shape and the interior structure of the supraparticles. Below 100 μM NaCl in the initial colloidal droplet, the final supraparticles were spherical and highly crystalline, whereas, for increasing salt concentrations of up to 10 mM the supraparticles became more nonspherical and less crystalline [Figure 1.13].

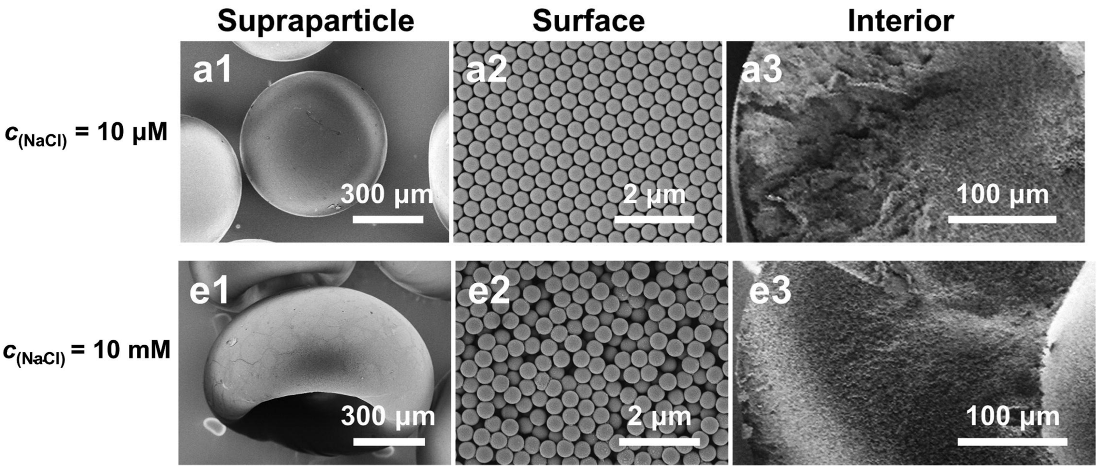

Figure 1.13: SEM images showing the final supraparticle shape, the surface and the interior. The first row corresponds to the supraparticles prepared with 10 μM NaCl in the initial colloidal droplet, whereas the second row shows those with 10 mM NaCl. Reprinted with permission from ref.[4] Copyright 2021 Elsevier.

Since supraparticles are usually formed by drying-induced assembly, the balance between the Brownian diffusion of colloids and the effective advection of the drying interface highly influences the assembly process and the final supraparticle structure.[41] In other words, changing the evaporation conditions such as temperature and humidity directly affect the final supraparticle. Slow evaporation provides time for the individual building blocks to minimize their free energy and promotes the formation of highly ordered and regular structures.[1] In case of fast evaporation, however, the structure formation is kinetically controlled and usually results in less defined supraparticles.[1] Liu et al.[15] obtained core-shell supraparticles by evaporating binary colloidal dispersions, i.e., the mixture of small and large colloids, at a faster rate (Pe=180 and 770, for small and large colloids, respectively) on superamphiphobic surfaces [Figure 1.14(b)]. Since the evaporation induced stronger inward forces on the larger colloids, the supraparticle core was mostly occupied by the amorphously packed larger colloids. Meanwhile, the smaller colloids were closely-packed into a crystalline structure forming the supraparticle shell. By increasing the humidity, evaporation conducted at a slower evaporation rate (Pe=27 and 110, for small and large colloids, respectively) which impeded the segregation and formed a disordered structure of small and large colloids [Figure 1.14(a)]. Raju et al.[133] also observed segregation of a few layers of smaller particles on the supraparticle surface from larger particles, which were pushed radially inside, after evaporating acoustically levitated droplets. When an external heat supply was used to heat the droplet, the faster evaporation rate led to a steeper density gradient enhancing the segregation behaviour. In another study, lowering the temperature at which the droplets levitated due to Leidenfrost effect prevented buckling on top of the droplet and led to spherical supraparticles.[96]

The prior research work clearly demonstrates that by tuning the properties of building blocks as well as the process conditions, one modifies the supraparticle structure. Studying the structure formation in supraparticles enables understanding the structure-property relationship of such mesoscale materials. Thereby, these materials can be utilized in different applications, as will be briefly described in Subchapter 1.8.

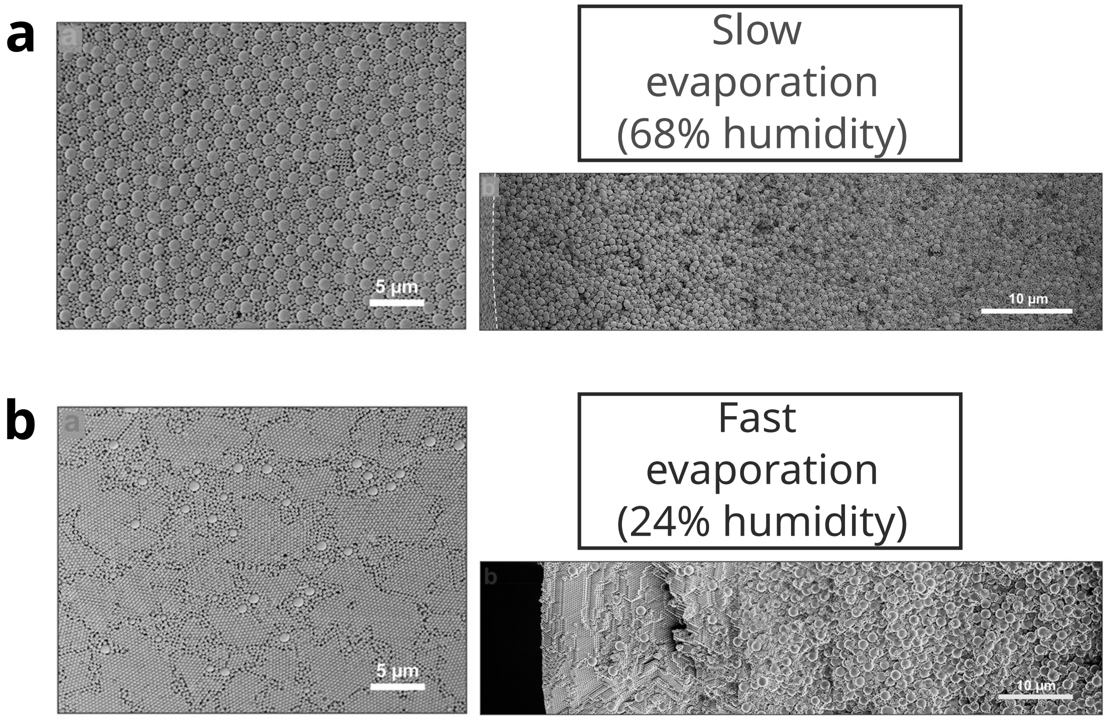

Figure 1.14: a) SEM images showing supraparticle surfaces (left) and cross-sections (right) prepared at slower evaporation rate (with Pe=27 and 110, for small and large colloids, respectively) and b) SEM images showing supraparticle surfaces (left) and cross-sections (right) prepared at faster evaporation rate (with Pe=180 and 770, for small and large colloids, respectively). Reprinted with permission from ref.[15] Copyright 2019 American Chemical Society.

1.8 Functionality and Potential Applications of Supraparticles

One of the reasons why supraparticles are a promising materials platform is related to their improved functionalities compared to their nano- or micron-sized constituents. Supraparticles may carry the functionalities of their building blocks, e.g., high specific surface area, catalytic activity, intrinsic material property.[2] In addition to this, they may exhibit emergent properties arising from the interactions between different types of building blocks.[2;1] Consequently, supraparticles are potential candidates for many applications in different fields.

For instance, structural coloration may be an emergent optical property of supraparticles.[1] The optical properties usually stem from the controlled arrangement of monodisperse colloidal particles within the supraparticle.[1] Rastogi et al.[70] made highly light-diffracting opal balls by using mixtures of variably-sized

PS nano-/micro-particles and gold nanoparticles [Figure 1.15(a)]. Changing the size of the PS particles changed the interparticle spacing on the supraparticle surface, which affected both the size and the color of the diffraction rings. The structural color of supraparticles made from silica and melanin was also manipulated through the degree of nanoparticle mixing.[134] The various optical effects that can be engineered with supraparticles promote their use in photonics.

Porosity is another emergent property that arises from the interstitial spaces inside the supraparticle.[1] The co-assembly of polymeric and inorganic particles into supraparticles is one way to enable the control of porosity. Liu et al.[2] prepared highly porous titania supraparticles from co-dispersed droplets of titania and PS nanoparticles, by the subsequent calcination of the sacrificial polymer particles [Figure 1.15(b)]. The resultant supraparticles with 92% porosity were showing enhanced photocatalytic activity.

Magnetic nanoparticles can be clustered into supraparticles to realize magnetic steering with realistic field gradients.[1] Hu et al.[135] prepared superparamagnetic supraparticles by evaporating ferrofluid droplets from superamphiphobic surfaces in the presence of a magnetic field. The final 3D architecture of the magneto-responsive supraparticles (e.g., deflated ball, cone, barrel, two-tower shapes) were tuned by varying the initial concentration of superparamagnetic nanoparticles and the applied magnetic field. Such superparamagnetic objects can be utilized in numerous applications such as microactuators, magnetic separation and drug delivery.[1;135]

The electrons in nanoparticles may interact strongly with each other once they are in close proximity. If separate electronic systems are connected within a distinct entity like supraparticles, they would generate functionality.[1] For example, surface plasmon resonance stems from the coherent excitation of electrons in metal particles, which results in coloration of many noble metal nanocrystals.[1] Supraparticles were suggested to increase the sensitivity of surface-enhanced Raman spectroscopy, as the electromagnetic field between plasmonic nanoparticles enhanced in close proximity.[136]

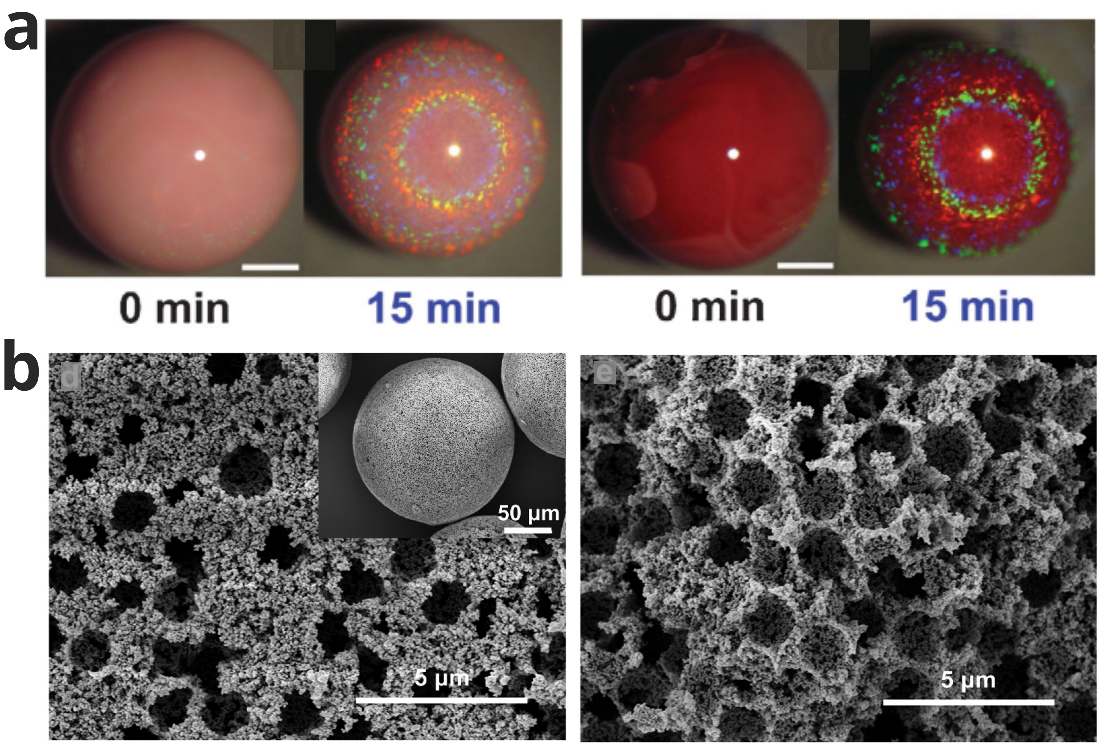

Figure 1.15: a) The timeline formation of mixtures of polystyrene and gold opal balls on a superhydrophobic substrate. Reprinted with permission from ref.[70] Copyright 2008 John Wiley and Sons. b) SEM images showing the surface (left) and interior (right) of highly porous titania supraparticles obtained after calcinating the sacrificial PS particles. Reprinted with permission from ref.[2] Copyright 2019 American Chemical Society.

1.9 Knowledge Gap and Proposed Solutions

Conventionally, spherical colloids have been the choice of building blocks to make supraparticles of various structures and compositions, as many examples I have provided in Subchapters 1.5-1.8 already suggested. The shape of the colloidal particles, however, is already a powerful tool for controlling supraparticle structure that remains largely unexplored.[6;137] New chemical and physical approaches allowed the synthesis of anisotropic colloids including cubes, triangles, prisms, rods, ellipsoids and stars.[6] Among them ellipsoidal colloids have caught many attention by stabilizing interfaces in emulsions and by suppressing the coffee-ring effect in drying suspensions.[7] All these shape anisotropic colloids are potential building blocks that can be incorporated into hierarchical superstructure assemblies for different applications.[6] Nevertheless, assembling nonspherical colloids into supraparticles is quite complex because of their additional orientational degrees of freedom and possible interaction anisotropy.[6;137;138]

Nonspherical colloids can cause interface deformations due to their shape anisotropy.[7;139;8] For instance, ellipsoids at an air-water interface might lead to quadrupolar type deformation by pushing down the interface at the tips and pulling up at the sides.[139] The interface deformation locally creates excess interface area.[139;8] Minimization of this excess interface area induces capillary interactions between colloids.[139;8]Due to the capillary interactions, colloids assemble by rotating into preferred orientations to minimize the total interfacial energy.[8] For ellipsoids, the interface deformation and associated capillary interactions are strongly related to both particle aspect ratio and contact angle.[140] In case of curved interfaces, the degree of confinement also modifies the interactions between the nonspherical colloids, and hence changes the self-assembled structure.[139;8]

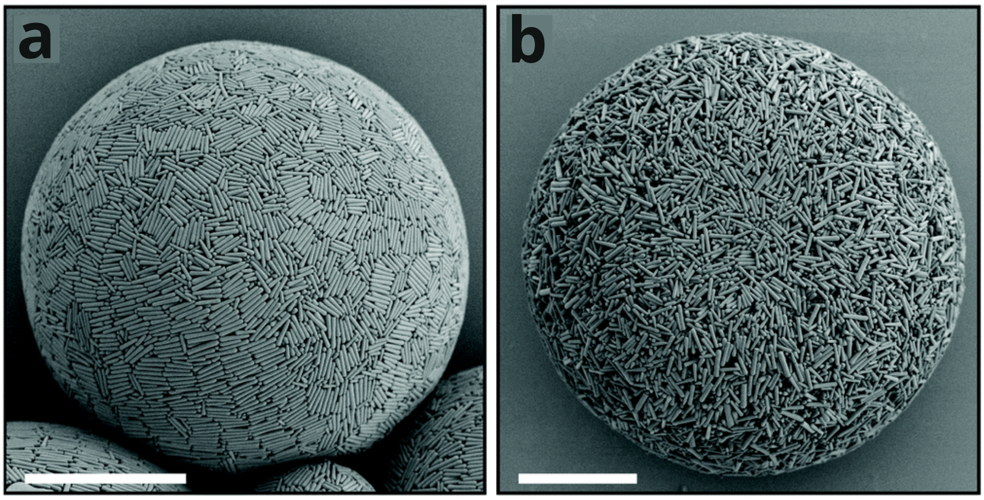

Figure 1.16: SEM images of supraparticles composed of silica nanorods showing a) smectic ordering and b) disorder on the surface. The scale bars correspond to 10 μm. Reprinted with permission from ref.[141] Copyright 2021 The Royal Society of Chemistry.

Confinement of nonspherical (anisotropic) colloids may promote orientational ordering and show rich phase behavior that would determine the functional material properties.[142;143;144] The following few examples from the literature have illustrated these possibilities. Jacucci et al.[141] used silica nanorods to form spherical supraparticles via emulsion evaporation and obtained a core-shell morphology, with a disordered core and an ordered shell. By adding salt into the dispersion, the surface ordering of the nanorods was tuned from smectic to isotropic [Figure 1.16]. This, in turn, resulted in a decrease of reflectance. It was further noted that the light scattering efficiency could be increased by increasing the range of nanorod ordering. Van der Hoeven et al.[145] fabricated silica coated gold nanorod supraparticles. Compared to their sphere counterparts, gold nanorods exhibited superior and highly tunable plasmonic properties due to their longitudinal surface plasmon resonance in the visible and near-infrared spectrum. Therefore, the nanorods enhanced the Raman scattering of analyte molecules. Wang et al.[146] showed the rich phase behavior of supraparticles composed of lanthanide fluoride nanoplatelets by having control over both their positional and orientational order. Assembling into different structures enabled tailoring the optoelectronic properties of supraparticles.

Apart from determining ordering and phase behavior, shape is a crucial parameter in controlling the maximum packing.[140] Instead of using spheres, cubic hematite nanocrystals were used to create supraparticles with a more open, porous structure, which can then be useful for gas sensing and photocatalysis.[147] The shape of colloids, i.e., the aspect ratio of anisotropic particles, therefore, plays an important role in controlling the mechanical properties of the final supraparticle.[140]

Moreover, confinement of binary mixtures, e.g., sphere-ellipsoid mixtures, increases the complexity of self-assembled structures and hence, the ability to vary the final properties.[148] Binary mixtures might lead to stratification of the constituents due to their differences in shape and/or size, altering the distribution and ordering of the components throughout the supraparticle.[148;149] This can potentially lead to multicomponent supraparticles, e.g. core-shell, or Janus.[149;150]

The prior research already indicated that different orientation and packing structures could be achieved by assembling nonspherical colloids under spherical confinement. However, the assembly pathway will be determined by several parameters such as the aspect ratio, surface properties, concentration, particle mixture composition, the degree of confinement, and the solvent evaporation rate.[14;149] Therefore, we need to understand these aspects better through systematic experiments and develop design rules to produce versatile supraparticles.

On this line of thought, I aimed to study the structure formation in supraparticles by investigating the ordering of ellipsoidal building blocks, the influence of mixing ellipsoids with spherical colloids, and the influence of the evaporation rate. In the experiments, I used polystyrene (PS) colloids to distinguish the effect of particle geometry from the effect of the materials properties.[151] Ellipsoidal PS building blocks were prepared at different aspect ratios starting from monodisperse PS spheres by a well-established film-stretching method,[152] which resulted in a good yield of monodisperse colloids. Since the density of an aqueous PS dispersion is close to that of water, and the as-prepared ellipsoids have similar interaction potentials and surface chemistry, I was able to study the physics of supraparticle formation.[151] Supraparticles were fabricated by evaporating dispersion droplets of aqueous PS dispersions, comprising of ellipsoids or sphere-ellipsoid mixtures, on silicone nanofilaments-based superamphiphobic surfaces, the advantages of which were discussed in Subchapter 1.6. The evaporation experiments were conducted inside a chamber with controlled humidity (in the following called humidity chamber) to examine the role of evaporation kinetics on the final supraparticle structure. The evaporation was recorded by a camera in order to track the morphology of the droplet during evaporation and perform image analysis, e.g., to calculate the change in volume and Péclet number. For some experiments, laser scanning confocal microscopy was also used to image the inner structure of the droplet during evaporation. The final supraparticle morphology was imaged by scanning electron microscopy and the images were later analyzed to calculate the orientational order parameter on the supraparticle surface. Particle-based simulations were also performed by our collaborators [redacted] and [redacted] to correlate the evaporation experiments and the ordering and/or the distribution of the colloids within the supraparticle at different evaporation kinetics.

Chapter 2

Experimental Methods

2.1 Materials

The required chemicals to prepare the superamphiphobic coatings, including methyl trichlorosilane (TCMS, 99%) and hexadecane (Reagent Plus, 99%) were purchased from Sigma Aldrich. 1H,1H,2H,2H-Perfluorodecyltrichlorosilane (PFDTS, 96%) was purchased from Alfa Aesar. N-Hexane (≥95%), toluene (≥99.8%), acetone (≥99.8%), and isopropyl alcohol (IPA, ≥99.8%) were purchased from Fisher Chemical. Ethanol (≥99.8%) was provided by Honeywell Research Chemicals. Ultrapure water with a resistivity of 18.2 MΩ·cm was obtained using a Sartorius Arium 611 VF water purification system. Glass slides 25×75 mm^2 in size were provided by Menzel-Gläser, Germany. Polystyrene (PS) colloids (negatively charged ≈ -59 mV, with -COOH groups on the surface) with a diameter of either 408 or 450 nm were synthesized by Gabriele Schaefer following the surfactant-free emulsion polymerization method.[153] The synthesized colloids were purified by several centrifugation cycles and were finally redispersed in ultrapure water. Polyvinyl alcohol (PVA, molecular weight 115000, degree of hydrolysis 86.5 – 89%) to form the matrix film was purchased from VWR Chemicals. Anionic surfactant sodium dodecyl sulphate (SDS, molecular weight 288.4) was purchased from MP Biomedicals. The aqueous suspension of fluorescently labeled spherical PS nanoparticles (carboxylate-modified, fluorescent red, diameter 500 nm) was provided by Sigma Aldrich to be used in confocal measurements.

2.2 Preparation of Superamphiphobic Surfaces

The silicone nanofilaments-based superamphiphobic surfaces were prepared by a grow-from method, as described previously.[115;154;151] Glass slides were first cleaned under ultrasonication in toluene, acetone, and ethanol and dried by a nitrogen flow. Glass slides were then activated by oxygen plasma at 30 W for 2 min (Diener Electronic Femto). To grow silicone nanofilaments from their surfaces, the activated glass slides were immersed in a mixture of 360 mL of toluene (with 166 ppm water content) and 250 µL of TCMS inside a sealed Teflon box. After 14 h of reaction, the silicone nanofilament-grafted glass slides were rinsed with hexane to remove any unreacted TCMS. The glass slides were annealed in a furnace at 200°C for 2 h to obtain a more stable silicone network. To achieve oleophobicity the nanofilaments were fluorinated by first reactivating the glass slides with oxygen plasma at 120 W for 2 min and by consecutively immersing them in 120 mL of hexane with 0.1 mL of PFDTS for 30 min. After the reaction, the substrates were rinsed with hexane to remove any unreacted fluorosilanes. The resultant nanofilament-coated glass substrates were homogeneous over a large area with micropores and overhang nanofilament structures ensuring its nonwettability [Figure 2.1]. Water and hexadecane acquired spherical droplets when dispensed on the resultant nanofilament-coated glass substrates.

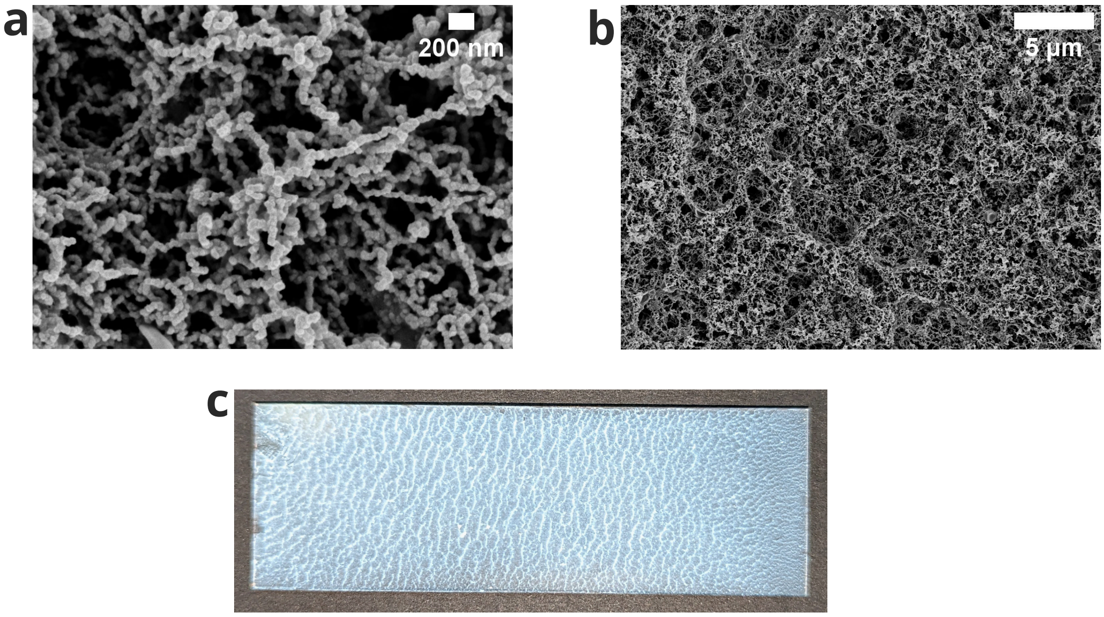

Figure 2.1: a) zoom-in and b) zoom-out SEM images showing the surface morphology of silicone nanofilament-coated glass substrates, c) picture of the 25×75 mm^2 glass substrate. Reprinted with permission from[151]. Copyright 2024 American Chemical Society.

2.3 Preparation of Polystyrene Ellipsoids

Polystyrene ellipsoids were prepared using a film-stretching method, which was established by Keville et al.[155] and Ho et al.[152] In this method, monodisperse spherical PS particles were embedded in a PVA matrix film and stretched in an oven above the glass transition temperature of the particles, which plastically transformed spheres into ellipsoids. After stretching, the films were cooled to room temperature and PVA matrix was dissolved to recover the ellipsoids. The preparation procedure is depicted schematically in Figure 2.2.

A 3.5 wt% aqueous PVA solution was obtained by dissolving 5 g of PVA in 139 mL distilled water at 80°C overnight. The solution was constantly stirred at 375 rpm to avoid foaming. Next, a homogeneous PVA/particle dispersion was prepared by adding 4 g of 10 wt% aqueous PS dispersion at 375 rpm for 5 h. The weight ratio of PS to PVA in the final dispersion was 0.08. The PVA/particle dispersion was then poured into a flat Teflon mold (15 × 28 cm^2) to air-dry for 1 day. The particle-embedded PVA film was cut into small film strips (3 × 8 cm^2 or 3 × 4 cm^2, depending on the desired draw ratio). These film strips were

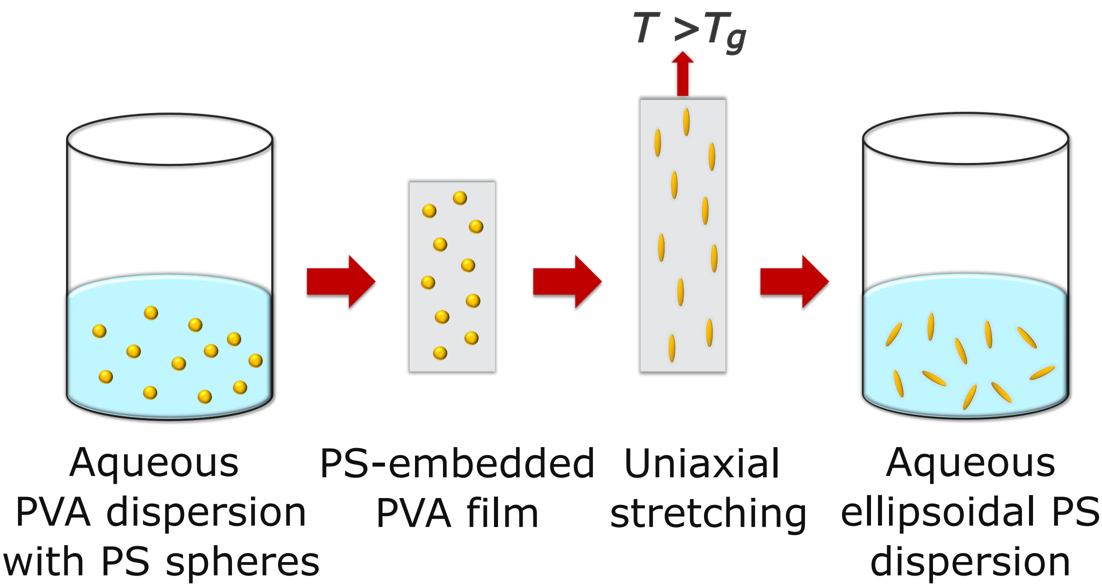

Figure 2.2: Schematic depicting the preparation of PS ellipsoids by mechanically stretching a PVA matrix film embedded with monodisperse PS spheres. Reprinted with permission from[151]. Copyright 2024 American Chemical Society.

stretched in an oven at 140°C by applying uniaxial tension with a tensile test apparatus (Zwick/Roell Z005 Universal Testing Machine). The stretching was performed at a speed of 300 mm/min without applying any extra load. The films were stretched at draw ratios of 100, 200, and 400% which resulted in ellipsoids of varying aspect ratio (λ) of about 4, 6, and 11, respectively. The particle size and aspect ratio were determined by counting 40 particles in a scanning electron microscopy (SEM) image of each batch [Table 2.1].

Draw ratio(%)	L (μm)	d_e(μm)	$\lambda = L/d_e$
100^a	0.92±0.05	0.26±0.01	3.5±0.3
200^a	1.30±0.11	0.21±0.02	6.1±0.8
400^a	1.95±0.21	0.18±0.02	11±2
200^b	1.37±0.10	0.19±0.02	7.2±0.9

Table 2.1: Dimensions (length L and diameter d_e) of the ellipsoids obtained from 408^a nm or 450^b nm PS spheres at different draw ratios. Reprinted with permission from[151]. Copyright 2024 American Chemical Society.

Several washing cycles were applied to extract the PS ellipsoids from the PVA matrix film. The cooled film strips were cut into smaller pieces (1×1 cm^2) omitting the edges, as the edges could be nonuniformly stretched near the metal clamps. The smaller film pieces were dissolved in a IPA/water mixture (3:7) (v:v) overnight under magnetic stirring. Subsequently, this mixture was heated to 85°C for 1 h to fully dissolve the PVA matrix. The dispersion was centrifuged at 10000 rpm for 1 h to sediment the ellipsoidal particles, and the viscous PVA–rich supernatant was decanted. The rest of the washing procedure followed dissolving the sediment again in an IPA/water mixture (3:7) (v:v) and centrifuging at 10000 rpm for 1 h. This cycle was repeated two times. To remove the remaining PVA, the ellipsoids were dispersed in water at 90°C for 1 h and centrifuged one last time. The resultant ellipsoids were redispersed in an appropriate amount of distilled water, depending on the required particle concentration.

2.4 Evaporation of PS Dispersion Droplets on Superamphiphobic Surfaces

The aqueous PS dispersions were prepared before the evaporation experiments. The volume concentration of PS ellipsoids or spheres in the dispersions was kept around 1%. The stabilized dispersions contained a 1 mM aqueous SDS solution with 0.5% PS spheres or ellipsoids. In case of binary supraparticles, the total volume concentration of sphere-ellipsoid dispersions varied between 0.6 – 1% with a volume ratio of ellipsoids to spheres V_e:V_s = 0.4, 1, 2.5, 5, and 10. Approximately 1 μL of these dispersions were dispensed onto the superamphiphobic surfaces with the help of an Eppendorf Research Plus pipet, which was equipped with epT.I.P.S. LoRetention Reloads tips. To perform the evaporation experiments in a controlled manner, a humidity chamber was built in-house [Figure 2.3]. The humidity chamber was equipped with an inlet and an outlet and the humidity was adjusted by mixing a stream of dry nitrogen gas and humidified nitrogen gas. The evaporation process was recorded by a camera (Blackfly S Color 5.0 MP USB3 Camera) through a window on the chamber. A humidity sensor was placed inside the chamber to record the humidity during evaporation experiments. Several droplets were dispensed through the holes on top of the chamber as soon as the humidity inside the chamber was equilibrated. The dispersion droplets evaporated at 23°C, either under ambient conditions (relative humidity RH of 30%) or at a higher relative humidity of either 75% or 90%. The chamber and the holes were kept sealed throughout the evaporation. At the end of evaporation, the supraparticles were easily collected in small vials by slightly tilting the superamphiphobic surfaces. It is important to note that sometimes small amount of the nanofilaments adhered on the supraparticle surface. This is most likely due to a few hydrophilic points that the nanofilaments still might have, which are pinning the contact line.

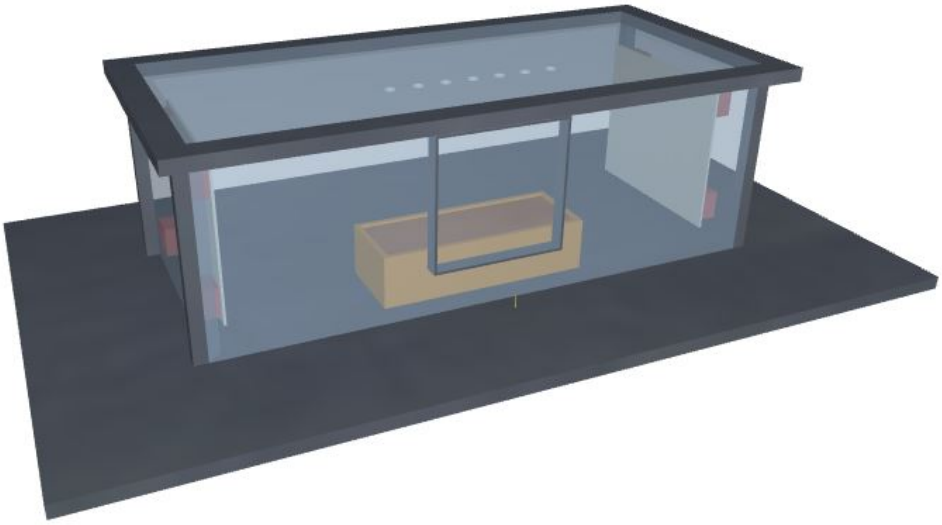

Figure 2.3: The render of the in-house built humidity chamber for evaporation experiments.

2.5 Scanning Electron Microscopy (SEM)

SEM is a conventional instrument to image the sample surface structure [Figure 2.4], which provides a high lateral resolution of typically 1-20 nm and high depth of field.[156] SEM uses an electron gun to produce the electron beam. The electrons are accelerated by an electric potential in the order of 1-30 kV.[156] A series of lenses, such as condenser and objective lens, are used to control the diameter of the beam and to focus the beam on the sample. The beam is raster-scanned by scanning coils over the sample.[156] Once the primary electrons hit the sample surface, they interact with the electrons in the sample giving them part of their energy. This results in the emission of secondary electrons. Such secondary electrons have low energies, which are on the order of $\approx$ 20 eV. Therefore, the only secondary electrons that can escape from the sample are those that are very close to the surface ($\approx$ 1 nm).[156] This is the reason why SEM is a highly surface-sensitive method. Finally, the secondary electrons are collected by a detector and their intensity is displayed versus the position of the primary beam on the sample. The imaging takes place in vacuum environment around $\approx 10^{-7}$ mbar to prevent the scattering of electrons by gas molecules. The samples must either be conductive or they must be coated with a thin metal layer to prevent electric charging by the electron beam.

The morphology of the superamphiphobic surfaces and the supraparticles here in this study were imaged by SEM at 3 kV (low voltage LEO 1530 Gemini, Germany). Prior to imaging, the samples were sputter coated with a 7 nm layer of Pt using a Safematic Compact Coating Unit-010 to avoid charging.

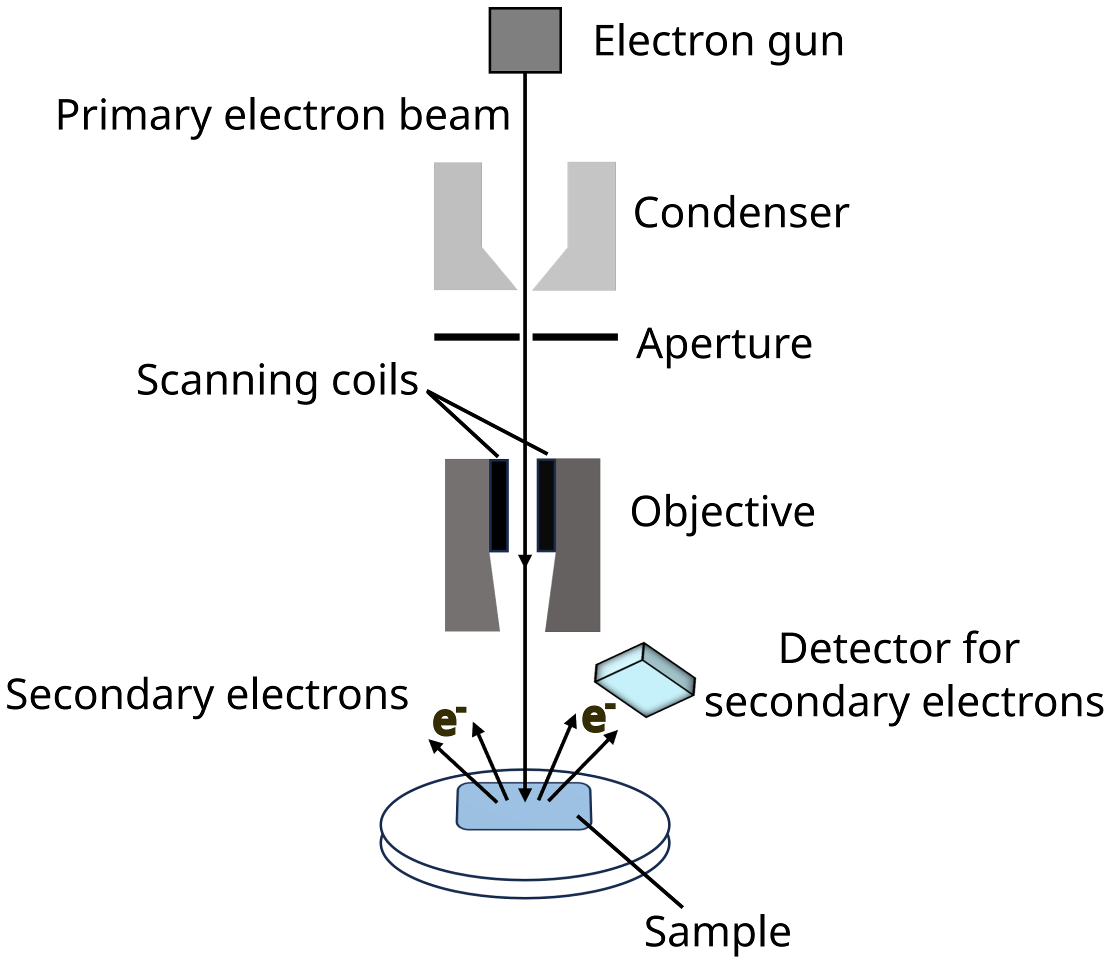

Figure 2.4: Schematic of a scanning electron microscope (SEM).

2.6 Other Characterization Methods

The water concentration of toluene is one of the key parameters to be taken care of when preparing silicone nanofilaments-based superamphiphobic coatings, as it directly effects the contact angles and sliding angles of droplets on the surface.[115] Therefore, before initiating the growth of nanofilaments, the water concentration of toluene was measured by using a Karl Fischer coulometer (Mettler Toledo C20 Compact KF coulometer).

Dynamic light scattering (DLS) measurements were carried on an ALV spectrometer to determine the size and polydispersity of the PS spheres, which was significant in later producing ellipsoids that were as monodisperse as possible. The spectrometer consisted of a goniometer and an ALV–5004 multiple–tau full–digital correlator (320 channels, angular range from 30° to 150°). A He–Ne laser (wavelength of 632.8 nm) was used as the light source. Measurements were conducted at 20°C at 9 varying angles ranging from 30° to 150°.

The zeta potential measurements were performed (Malvern Zetasizer Nano Z) to estimate the stability of the colloidal dispersions.

The evaporation process was further monitored by laser scanning confocal microscope (confocal microscopy, Leica Microsystems TCS SP8). 1 μL dispersion droplet was dispensed on a transparent superamphiphobic surface, which was coated on a high precision microscope cover glass (Carl Roth GmbH, thickness: 170 ± 5 μm). The confocal microscope was operated with a dry objective $10\times/4.5$ or $10\times/2.5$ and with an excitation beam of a Ar laser at 514 nm.

ImageJ software was used to perform image analysis with the evaporation videos of the droplets. The analysis helped recording the change in droplet volume as a function of time. The volume of the droplets was estimated by performing solid of revolution[157] without assuming any predefined droplet shape. To compute the volume, an arc that passes through the circumference of one half of the droplet was determined by using its 2D image. Then, disc–shape slices, which touch this arc and cut the central axis perpendicularly, were integrated around this central axis of the droplet. The method is depicted schematically in Figure 2.5.

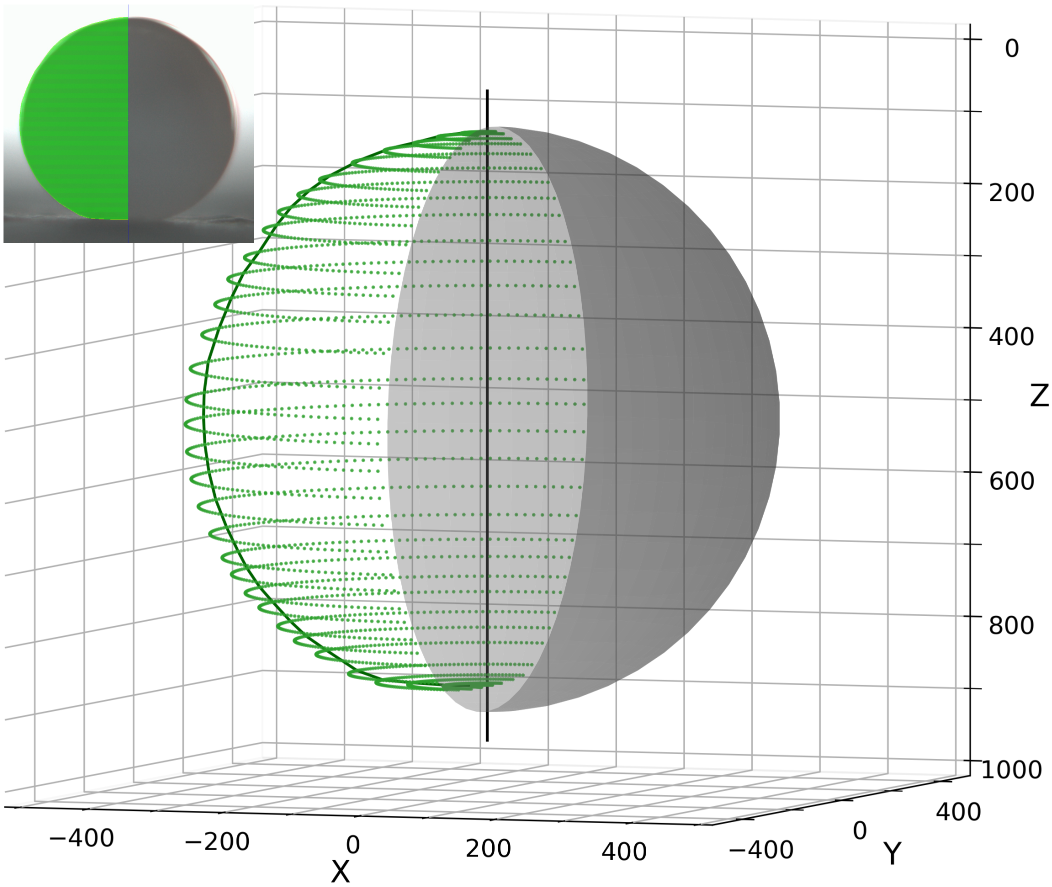

Figure 2.5: 3D reconstruction of a droplet showing the arc and disc–shape slices (green) determined for solid of revolution. A half of a sphere (gray) is depicted for comparison with the droplet. The inset shows an image of an evaporating droplet, on which disc–shape slices are determined to compute the volume. Reprinted with permission from[151]. Copyright 2024 American Chemical Society.

Chapter 3

Supraparticles with Buckled Morphology

3.1 Background: Buckling Phenomenon

Drying of colloidal dispersions is a complex process which involves several phenomena such as solvent diffusion, transfer of particles to the vapor interface, gelation, or glass transition.[158] Kinetics of drying usually occur far from equilibrium, during which the concentration of colloids increases as solvent evaporates.[94] This alters the rheological properties of the medium which, initially fluid, can change into a viscoelastic or brittle solid.[158] As a result, the dried structure might show mechanical instabilities, such as fracture and buckling. In practice, this buckling phenomenon is relevant in spray-drying and in various industrial processes (coatings, cosmetics, detergents, pharmaceuticals, engineering porous materials, etc.).[94;159;95]

High concentration gradients develop at the air-liquid interface during the drying of colloidal droplets.[158] Consequently, a shell layer of colloids might form. If this shell layer undergoes a sol-gel transition, it starts showing an elastic behaviour.[94;158] The elastic shell does not impede evaporation. Instead, this curved shell under external pressure minimizes its energy through extensional and bending deformations and forms a nonspherical buckled geometry (e.g., wrinkled or dimpled sphere).[158;160]

The final morphology of the drying droplets, and hence, the supraparticles will be determined by the interplay of several parameters, including interparticle interactions, evaporation kinetics, the initial colloid volume fraction, the colloid size and the viscosity of the colloidal dispersion.[160;159] The stress on the shell has to exceed a critical value depending on these factors to lead to the buckling instability.[158;94] For instance, varying humidity changes the evaporation rate, which in return, changes the shell thickness and the stress. Depending on the type of application, the desired supraparticle morphology, e.g., spherical or buckled, would differ. Buckled supraparticles might be preferred over spherical ones for catalysis and absorption applications due to larger surface to volume ratios, whereas spherical supraparticles might be used as drug encapsulators.[161] Therefore, governing the final morphology of supraparticles is important and could be achieved by adjusting the aforementioned variables.

Previous studies suggested the effect of primary particle shape on controlling the final supraparticle morphology.[162;98]Harraq et al. observed buckled supraparticles composed of low aspect ratio rods (< 9), whereas they suppressed buckling for supraparticles composed of high aspect ratio rods (> 9).[162] Suppression of buckling was attributed to the increase in shell permeability in case the shell was formed by more elongated rods. Thin and dense shell showed buckling where thick and porous shell did not, as the porosity decreased the capillary pressure causing the buckling instability. In another study, Mondal et al. produced buckled, doughnut-shaped supraparticles with high aspect ratio ($= 4$) ellipsoids, in contrast with spherical supraparticles comprising low aspect ratio ($= 2$) ellipsoids.[98] The stronger van der Waals attraction between the less elongated colloids was shown to result in more stable supraparticles. Meanwhile, the shell that was formed by higher aspect ratio colloids was less porous and the evaporation continued only by buckling of this shell. This prior research clearly highlighted the role of primary particle shape on determining the supraparticle morphology. Yet, it still lacks experimental data showing the effect of colloidal stability, of ellipsoids of different aspect ratios as well as binary mixtures, and of a wide range of Péclet numbers on the supraparticle shape. Continuing Chapter 3, I will discuss experimental results regarding these aspects.

3.2 Péclet Number Calculation

Péclet number is an important quantity to characterize the structure formation in supraparticles, as already discussed in Subchapter 1.3. To estimate the Péclet numbers, we should refer back to equation 1.1, which suggests the linear decrease of $V^{2/3}$ with respect to time. In the experiments, the droplet volume was estimated by video analysis using the solid of revolution method (see Subchapter 2.7). Examples of evaporation curves are given below, which belong to sphere-ellipsoid mixtures (with λ= 4) at slower [Figure 3.1(a)] and faster evaporation kinetics [Figure 3.1(b)]. By knowing the droplet volume and the time, the evaporation speed α can be extracted. Then, taking the time derivative of equation 1.1, one obtains v_{ev} by the following expression[15]

$$v_{ev} = \frac{1}{2}(\frac{3}{4\pi})^{2/3}\frac{\alpha}{R_0} \tag{3.1}$$

Now, each variable to calculate τ_{ev} is known. Next, to calculate τ_d, one needs to find D_0. For a spherical colloid, D_0 can be estimated through the Stokes-Einstein relation as follows

$$D_s = \frac{k_BT}{6\pi\eta d} \tag{3.2}$$

where η is the medium viscosity and d is the radius of a sphere. For the sake of simplicity, the viscosity was taken as that of water (η=$10^{-3}kgm^{-1}s^{-1}$).

For an ellipsoid, the parallel diffusion coefficient ($D_{\parallel}$) and the perpendicular diffusion coefficient ($D_{\perp}$) can be given as[163]

$$D_{\parallel} = \frac{k_BTln(L/d_e)}{2\pi\eta L} \tag{3.3}$$

$$D_{\perp} = \frac{k_BTln(L/d_e)}{4\pi\eta L} \tag{3.4}$$

Using the expressions for $D_{\parallel}$ and $D_{\perp}$, the diffusion coefficient for an ellipsoidal colloid D_e is found by[163]

$$D_e = \frac{(D_{\perp} + 2D_{\parallel})}{3} \tag{3.5}$$

Finally, Péclet number can be calculated as the ratio of τ_d to τ_{ev} (see equation

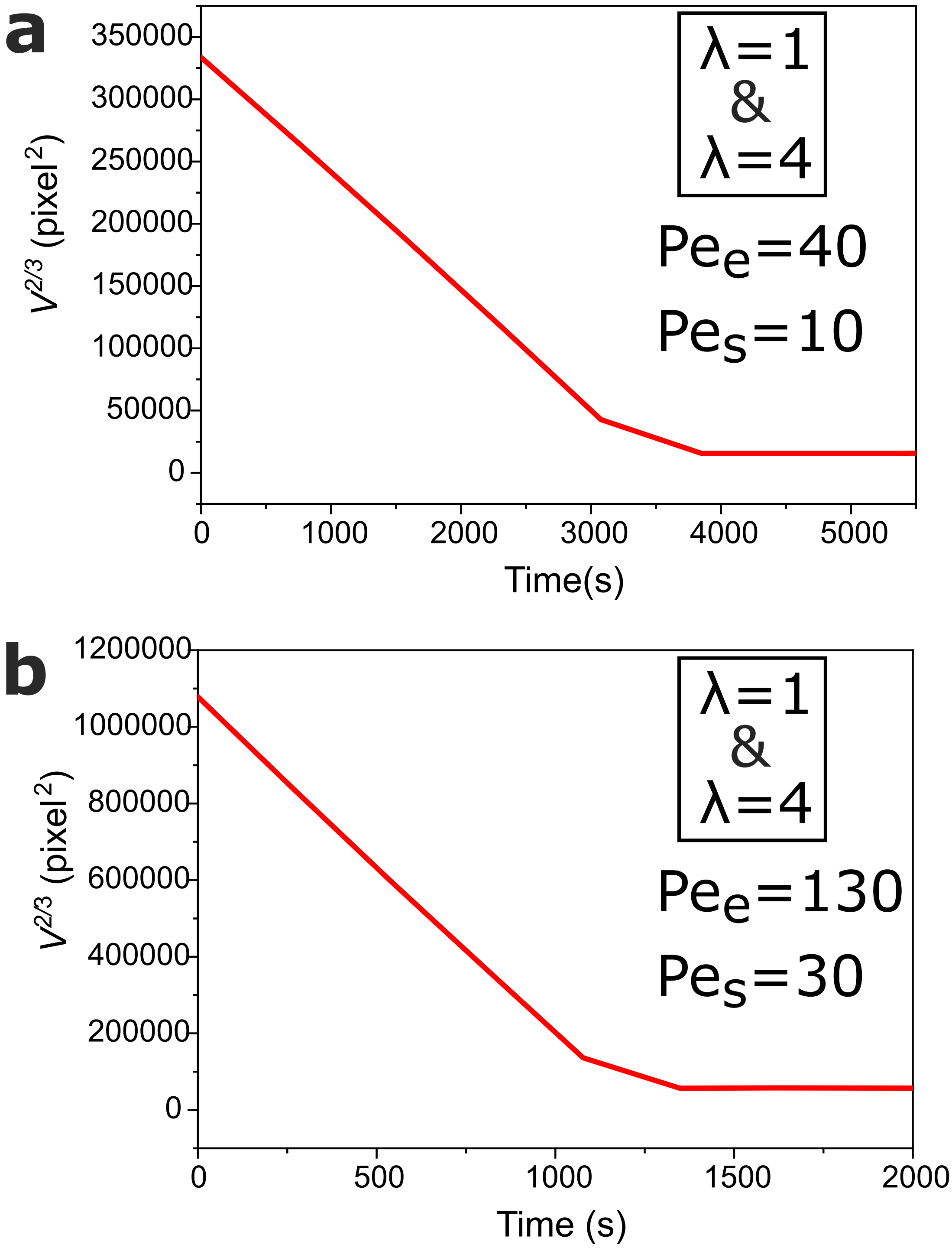

Figure 3.1: Evaporation curves showing the almost linear decrease of droplet $V^{2/3}$ over time for sphere-ellipsoid (λ= 4) mixtures at a) slower and b) faster evaporation rate. The Péclet numbers for ellipsoids (Pe_e) and spheres (Pe_s) are labelled on the plots.

1.2). Throughout this study, $Pe \gg 1$ is defined as the evaporation-limited regime and $Pe \leq 1$ is defined as the diffusion-limited regime. The different Péclet regimes are depicted in the drying simulation snapshots below [Figure 3.2] with $Pe \gg 1$ indicating the concentration gradients inside the droplet due to fast advection and $Pe \leq 1$ showing the almost homogeneous distribution of colloids inside the droplet due to slow advection. For the rest of this thesis, Pe_e and Pe_s refer to the Péclet numbers for the ellipsoids (rods in simulations) and spheres, respectively.

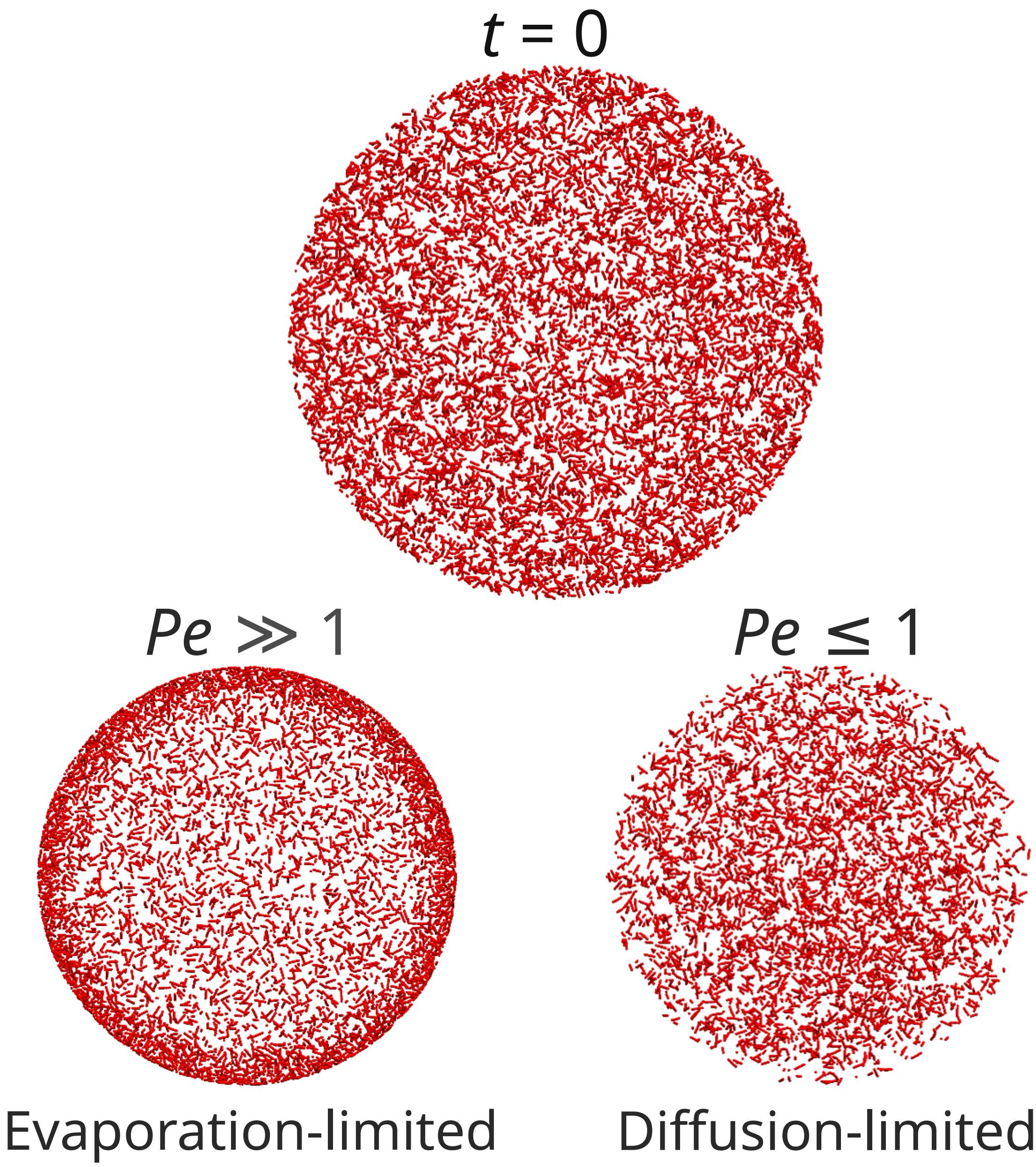

Figure 3.2: Drying simulation snapshots depicting the evaporation-limited regime ($Pe \gg 1$), where evaporation is fast, and the diffusion-limited regime ($Pe \leq 1$), where evaporation is slow.

3.3 Buckled Supraparticles Composed of Varying Colloid Shape

Aqueous dispersion droplets of PS ellipsoids of varying aspect ratios (λ= 4, 6, and 11, corresponding to approximate lengths 0.92 μm , 1.30 μm, and 1.95 μm, see Table 2.1) were used to observe the effect of primary particle shape on the final supraparticle shape. The colloidal droplets were evaporated on silicon nanofilaments-based superamphiphobic surfaces inside a humidity chamber. The humidity chamber ensured a constant humidity by providing continuous nitrogen flow. In this set of experiments, the humidity inside the chamber was set to RH=75% which led to 50$\leq Pe_e \leq$60. Accordingly, the droplets were completely dried in about 90 minutes. The supraparticles formed an irregular final shape that varied for each aspect ratio [Figure 3.3(a-c)]. Each supraparticle showed at least one dimpled region and a wrinkled surface texture. The surfaces corresponding to each supraparticle are given in the second column [Figure 3.3(d-f)]. The ellipsoids formed small bundles which were locally and laterally aligned on the supraparticle surface. For λ= 4 and 6, most ellipsoids oriented in plane, while for λ= 11 there appeared some out of plane-oriented ellipsoids. To image their internal structure by SEM, the supraparticles were cut with the help of a scalpel. The left image of Figure 3.4 shows a broken irregular-shaped supraparticle. As can be observed from the interior SEM image on the right [Figure 3.4], the ellipsoids inside the supraparticle showed a random orientation. Ellipsoids packed randomly for all the aspect ratios studied.

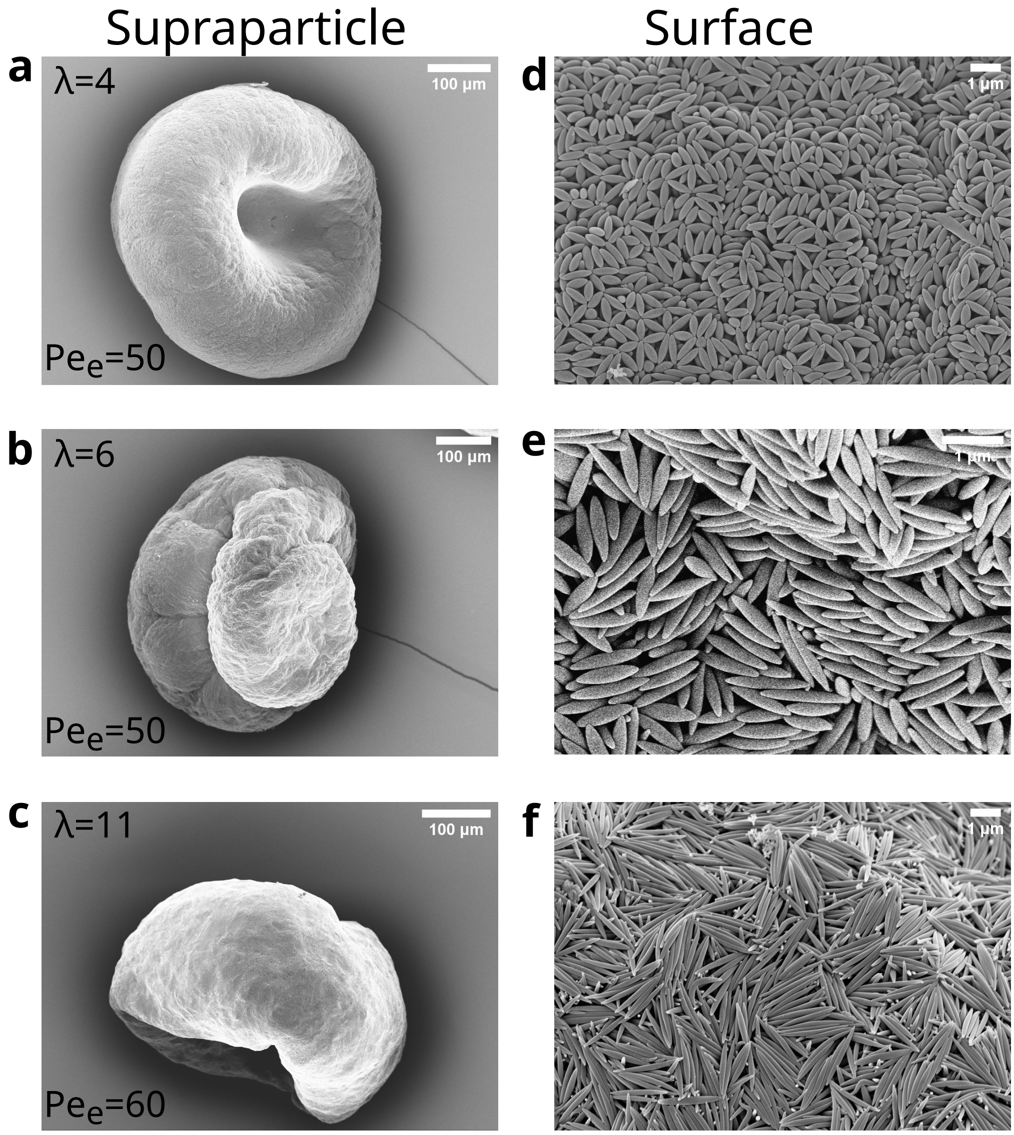

Figure 3.3: SEM images showing the final supraparticle morphology and their corresponding surfaces, composed of ellipsoids of λ= (a,d) 4, (b,e) 6, and (c,f) 11. The supraparticles were evaporated at RH=75%, in which the complete drying took almost 90 minutes with $50 \leq Pe_e \leq 60$.

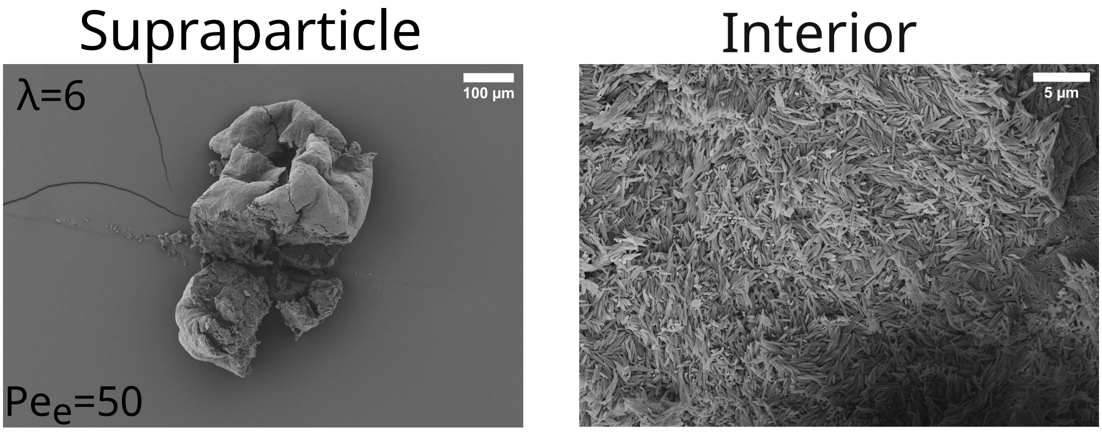

Figure 3.4: SEM image of a cut supraparticle (left) composed of λ= 6 ellipsoids at Pe_e=50. SEM image on the right exemplifies the interior structure of the supraparticles formed under the given conditions.

As I already introduced in Subchapter 3.1, the deterioration from spherical shape is a common phenomenon for drying colloidal dispersion droplets, which can be named as buckling. The buckling phenomenon was also captured through the videos recording the evaporation experiments and is schematically depicted with spherical building blocks in Figure 3.5 below. Initially, the droplets shrink isotropically on the superamphiphobic surface behaving like a pure liquid and maintaining their spherical shape. As water evaporates, the overall particle concentration increases during which the colloidal stability of the system decreases. For large Péclet numbers, especially in the evaporation-limited regime, the air-water interface recedes way faster than the particles could diffuse inside the droplet. This could lead to the formation of a dense shell layer of particles near the air-water interface.[94;158] As the shell thickens, the droplet cannot shrink isotropically. Instead, the droplet flattens and later forms an irregular shape, which appears like a deflated ball. In my experiments, this flattening and successively buckling of the droplets occurred towards the end of the evaporation (at time= 85 minutes) and was rather fast (in almost 5 minutes). The buckling is attributed to the formation of a shell layer, which starts behaving elastically and deforms after a certain pressure.[94] This shell layer tends to emerge in case the attractive forces between the colloids exceed the stabilizing electrostatic forces.[94] Once the colloids start accumulating on the receding air-water interface, they will be objected to strong capillary forces. The attractive capillary forces might densify the shell layer and increase the capillary pressure inside the droplet. Such strong capillary pressure results with the buckling of the shell, since this is how the shell could to relieve its stress.[164;165]

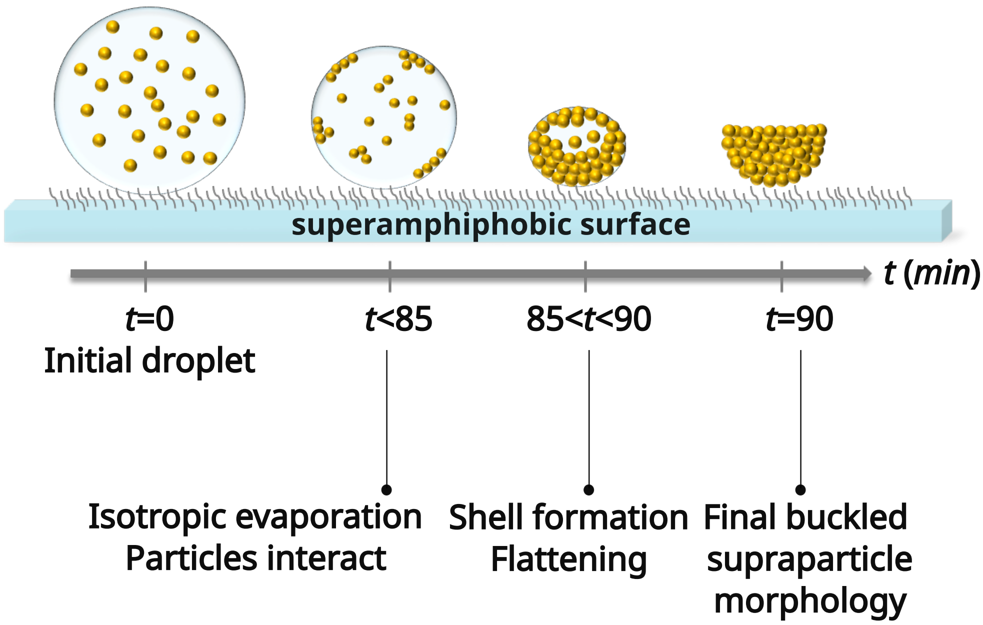

Figure 3.5: Schematic depicting the buckling process of an evaporating colloidal dispersion droplet on superamphiphobic surface. The times at which the certain events occurred were deduced by analyzing the recorded videos of evaporation experiments.

Sufficiently long micron-sized ellipsoids at liquid interfaces have been shown to possess strong, shape-induced, long-range capillary attraction.[166;167;168] In fact, the ellipsoidal particles are found to interact over distances several times longer than their major axis.[166] This leads to an attractive strength of about several orders of magnitude larger than the thermal energy k_BT near contact.[166;167] For this reason, ellipsoids have been used to stabilize interfaces in emulsions.[7] The self-assembly of ellipsoids are governed mainly by these strong lateral capillary interactions, which are highly dependent on their aspect ratio and contact angle.[166;167;168] If at a planar interface, spherical colloids do not experience lateral capillary interactions and their self-assembly are dominated by direct interactions, such as electrostatic or van der Waals interactions.[139;168] However, at a curved interface, although not as strong as ellipsoids, spherical colloids will also induce capillary interactions.[139;169] Therefore, ellipsoids inducing strong lateral capillary interactions may drive the deformation of a shell way easier compared to spheres.

With this in mind, I made supraparticles composed of PS spheres (of 408 nm in diameter and are shown with λ= 1). The evaporation experiments were again conducted inside the humidity chamber at RH=75% starting with 1% initial volume fraction. The complete drying of the droplets took about 90 minutes again corresponding to Pe_s=10. The use of spherical building blocks did not actually suppress buckling. At the end of drying, the supraparticles formed a small buckled region from the top, but remained otherwise spherical [Figure 3.6 (left)]. In contrast to the wrinkled supraparticle surfaces composed of ellipsoids, the surfaces here in this case showed a rather smooth texture [Figure 3.6 (right)]. Crystalline regions of PS spheres with some line and point defects were observed on the supraparticle surface.

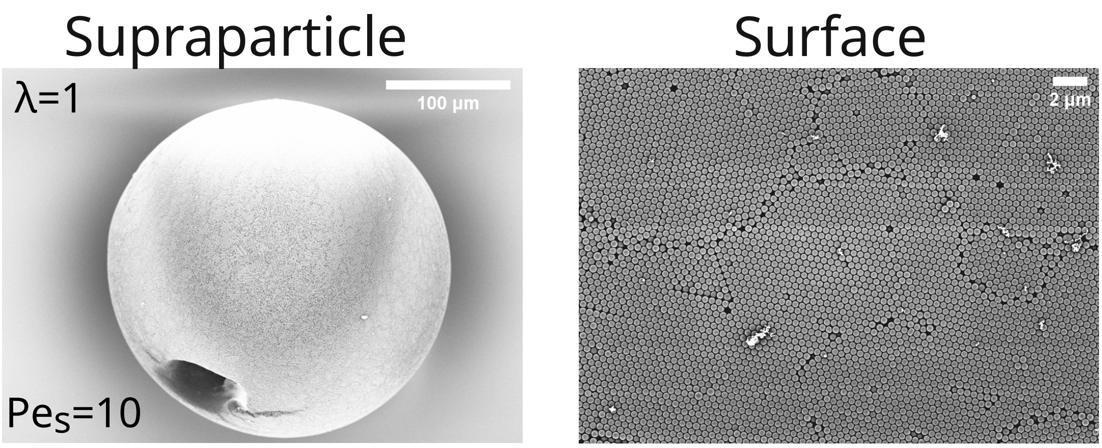

Figure 3.6: SEM images showing the supraparticle (left) and the supraparticle surface (right) composed of PS spheres (408 nm in size). The supraparticles were evaporated at RH=75%, in which the complete drying took almost 90 minutes with Pe_s=10.

After making supraparticles composed solely of ellipsoids or spheres to see if the primary particle shape affects buckling, the idea of using sphere-ellipsoid mixtures arose. A theoretical study previously showed that there could be capillary attraction between an ellipsoid and a sphere at a planar interface.[139] The capillary attraction originated by spheres interacting with the interface deformation around the ellipsoid, which generated a locally curved interface. Hence, using binary mixtures of different shapes might change the capillary interactions and the final supraparticle structure. The binary supraparticles were fabricated by evaporating dispersion droplets of sphere-ellipsoid mixtures. The PS spheres were 450 nm in diameter and the λ= 7 ellipsoids had a corresponding length of about 1.37 μm. The total initial colloid volume fraction was 0.6% with an equal volume ratio of ellipsoids to spheres (v_e:v_s = 1). The evaporation experiments were done under the same conditions as before at RH=75%. The drying of droplets were completed in 90 minutes with Pe_e=50 and Pe_s=10. The supraparticles were ill-shaped and showed a large buckled region from the top [Figure 3.7 (left)]. The surface of the binary supraparticles [Figure 3.7 (right)] consisted mostly of ellipsoids. The ellipsoids oriented randomly on the surface. Some spheres appeared as well and filled in the interstitial spaces between ellipsoids.

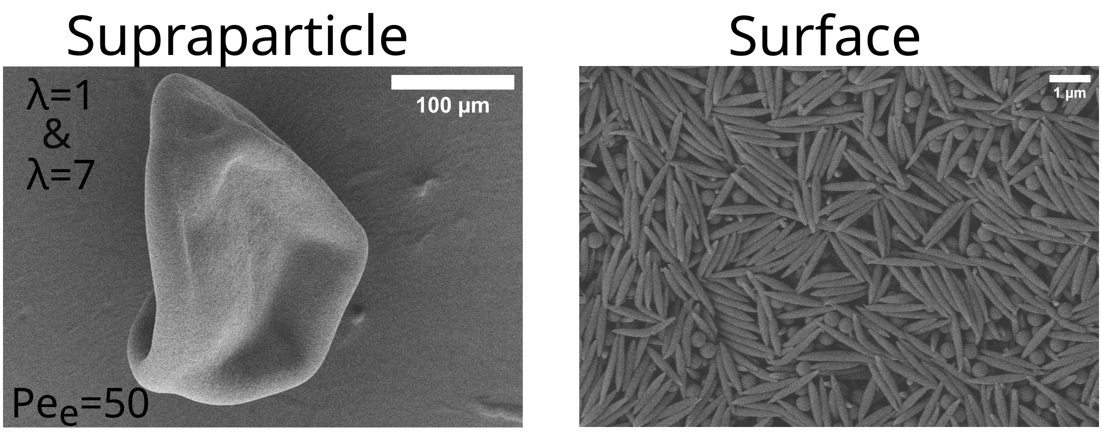

Figure 3.7: SEM images showing the binary supraparticle (left) and the supraparticle surface (right) composed of sphere-ellipsoid mixture. The spheres (450 nm in size) and the ellipsoids (λ= 7) had an equal volume ratio. The supraparticles were evaporated at RH=75%, in which the complete drying took almost 90 minutes with Pe_e=50 and Pe_s=10.

To better visualize the buckling and the how colloids distribute within the droplet, the evaporation experiments were monitored by laser scanning confocal microscopy. The evaporation of the droplets took place at ambient conditions (RH=30%), since the humidity chamber could not be coupled with the microscope. Thus, the evaporation rate increased compared to the previous experiments and the droplets were completely dried in 30 minutes. The droplets were evaporated on the superamphiphobic surface, which was coated on a thin, high precision microscope cover glass to allow imaging with the confocal microscope from below. The initial colloid volume fraction of the droplets were kept much more dilute to prevent refractive index mismatch during the confocal imaging. In the first set of experiments, supraparticles were made by using commercial aqueous dispersion of spherical PS particles. The PS spheres were fluorescently labeled and 500 nm in size. The droplets containing spheres (0.1% initial volume fraction) showed a distinct accumulation of particles at the droplet-air interface at time=20 minutes [Figure 3.8(a)]. At the end of drying, time=30 minutes, the droplet formed an almost spherical supraparticle [Figure 3.8(b)]. In the second set of experiments, binary supraparticles were made by using a mixture of these fluorescently labeled spheres and non-labeled ellipsoids of $\lambda = 4$. The total initial volume fraction of aqueous mixture droplets was 0.2% with equal volume ratio of ellipsoids to spheres (v_e:v_s = 1). At time=25 minutes of evaporation, the droplet showed a layer of accumulated particles at the droplet-air interface [Figure 3.8(c)]. In the core, there appeared a distinct particle jamming of fluorescently labeled spheres and non-labeled ellipsoids. The droplet was still spherical at this stage. The deterioration from sphericity happened quite fast. Figure 3.8(d) displays a shell that was already buckled at time=30 minutes, in which the droplet core still showed jamming of colloids. The colloids finally consolidated into an irregular shaped supraparticle, which looked like a deflated ball, at time=32 minutes [Figure 3.8(e)].

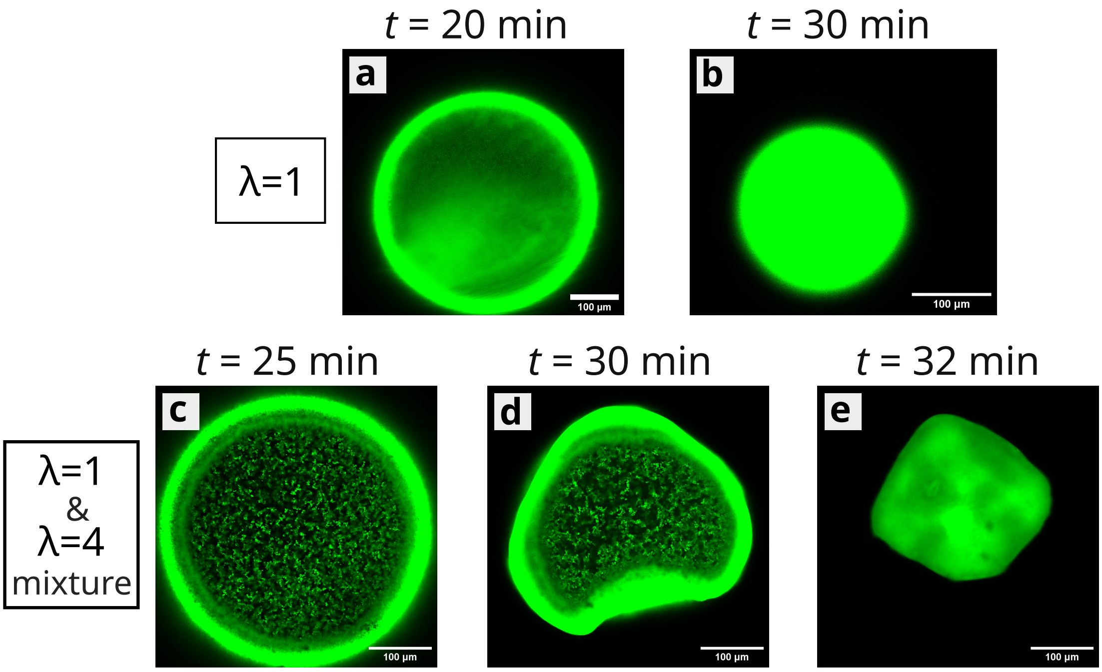

Figure 3.8: Confocal microscopy snapshots of an evaporating droplet of fluorescently labeled commercial PS spheres after a) t=20 minutes, and b) the resultant supraparticle after t=30 minutes. Snapshots of an evaporating droplet of sphere-ellipsoid mixture after c) t=25 minutes d) t=30 minutes, and e) the resultant buckled supraparticle after t=32 minutes. The mixture droplet contained fluorescently labeled commercial PS spheres and non–fluorescent ellipsoids of λ= 4.

3.4 Buckled Supraparticles Obtained at Different Evaporation Kinetics

The process conditions during evaporation, e.g., temperature and humidity, play an important role on the final morphology of the supraparticle. Close to the diffusion-limited regime, $Pe \leq 1$, the evaporation is slow and the colloids inside the droplet distribute more homogeneously during evaporation.[160;94] This finally leads to the formation of a spherical supraparticle morphology. However, in the evaporation-limited regime, where $Pe \gg 1$, the evaporation is way faster than the diffusion of colloids. Eventually, advection develops concentration gradients inside the droplet, which might drive the formation of a shell. For this reason, buckling, and hence, the formation of crumpled, irregular shaped supraparticles is more prone to form under fast evaporation conditions.[160;94] The study of Biswas et al.[170] illustrated the effect of evaporation kinetics, as they tuned the final morphology of spray- dried microcapsules by changing the drying temperature. At lower temperature, the nanoparticles assembled into a compactly packed spherical granule. By increasing the drying temperature, the nanoparticles packed into thin shells and led to the formation of hollow capsules that finally buckled into a toroidal shape.

To probe the effect of evaporation rate on the final supraparticle structure, I performed evaporation experiments at different humidity, leading to different Péclet numbers. By decreasing the humidity, the same evaporation experiments occurred at a faster evaporation rate. Aqueous droplets of λ= 4, 6, and 11 ellipsoids were evaporated at RH=30% leading to $170 \leq Pe_e \leq 200$. In this case, the complete drying of dispersion droplets took 30 minutes. As the Péclet numbers were even higher than those in Figure 3.3, all the supraparticles eventually buckled. Figure 3.9(a-c) shows the crumpled final supraparticle with at least one dimpled region for each aspect ratio. The respective supraparticle surfaces [Figure 3.9(d-f)] had a wrinkled texture. As before, ellipsoids formed local regions of laterally oriented bundles on the supraparticle surface.

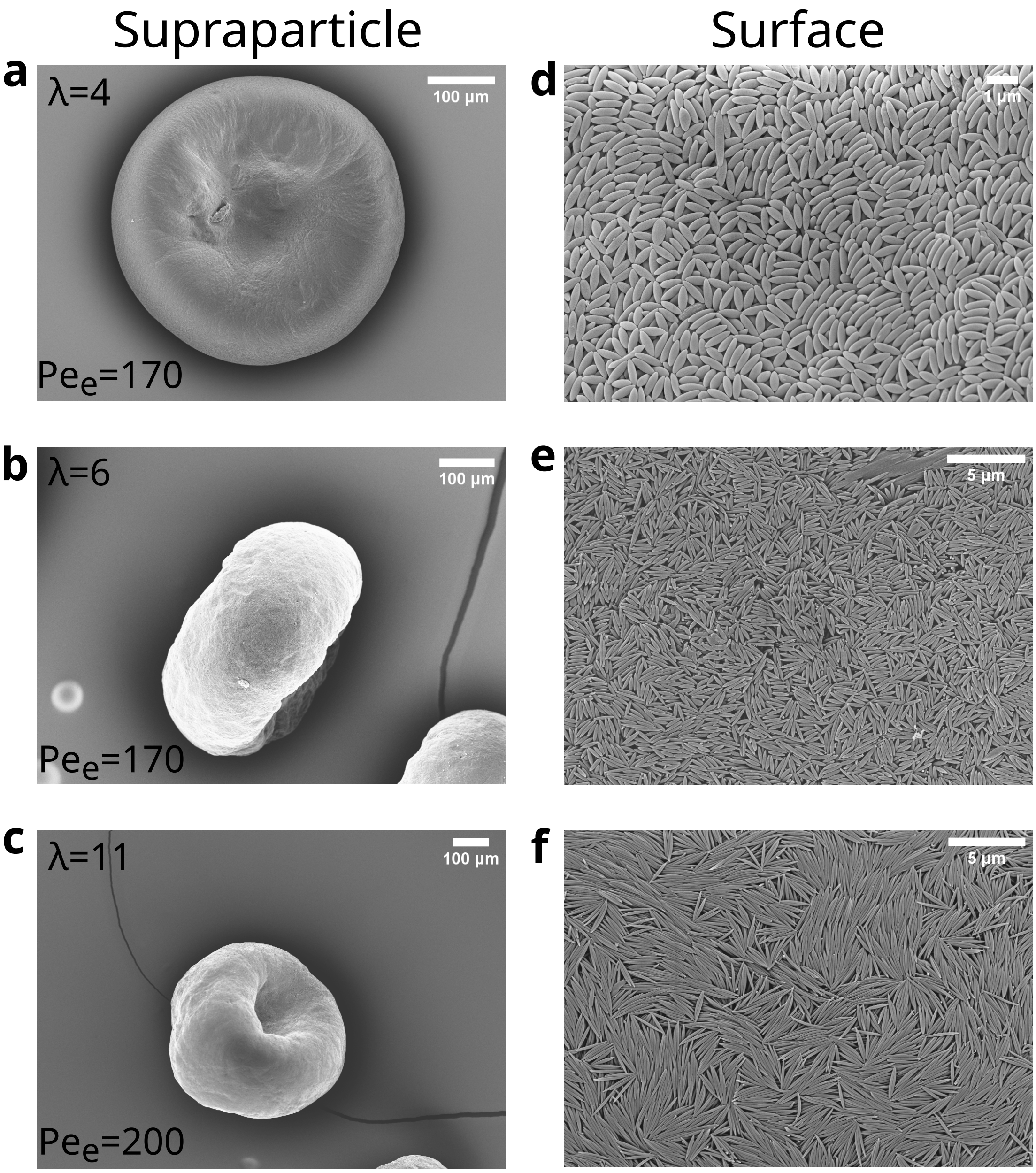

Figure 3.9: SEM images showing the final supraparticle morphology and their corresponding surfaces, composed of ellipsoids of λ= (a,d) 4, (b,e) 6, and (c,f) 11. The supraparticles were evaporated at RH=30%, in which the complete drying took almost 30 minutes with $170 \leq Pe_e \leq 200$.

As a next step, I performed the evaporation experiments at a higher relative humidity to slow down the evaporation rate. The diffusion-limited regime ($Pe \leq 1$) is experimentally difficult to achieve, because the colloids have small translational diffusion coefficients, which are on the order of 10^{-13} m^{2}s^{-1} for ellipsoids.[95] $Pe \leq 1$ requires the evaporation rate $v_{ev} \leq 10^{-9}$ ms^{-1}, which is at least one order of magnitude smaller than the current conditions. In the end, the closest value I could reach experimentally was Pe_e=10 (with v_{ev} on the order of 10^{-8} ms^{-1}). In this case, the evaporation experiments were performed at RH=90% by placing several water containers around the superamphiphobic substrate inside the humidity chamber. The humidity value was no longer precise under these conditions, as the humidity sensor was not sensitive enough to specify such high humidity. The complete drying of the dispersion droplets of PS λ= 7 ellipsoids took almost 315 minutes. Although the evaporation was four times longer than in Figure 3.3, the obtained supraparticle morphology was still irregular and resembled a deflated ball [Figure 3.10 (top)]. As was already the case for previously buckled supraparticles above, these also showed a wrinkled surface texture [Figure 3.10 (bottom)]. It is worth mentioning here that the ellipsoids on the surface seemed more aligned compared to those obtained at 50≤Pe_e≤60. From the SEM images, it seems that the λ= 7 ellipsoids ordered along their short axis direction up to three ellipsoid diameters and did not show any ordering along their long axis direction.

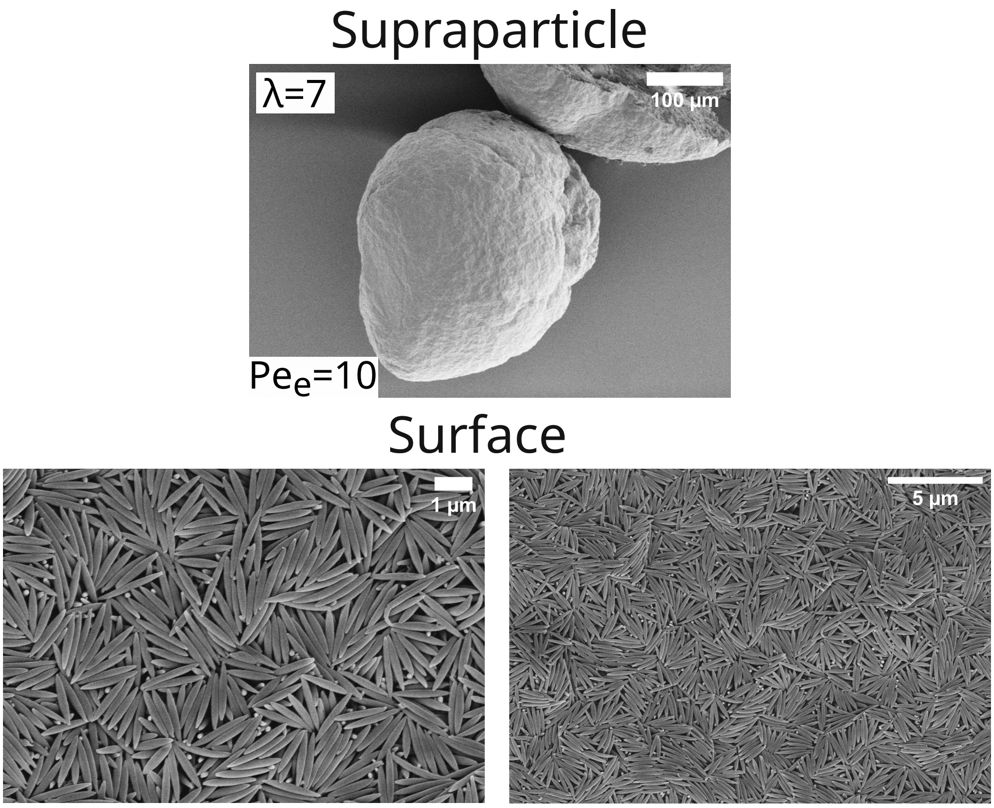

Figure 3.10: SEM images showing the supraparticle (top) and the supraparticle surface (bottom) composed of λ= 7 ellipsoids. The supraparticles were evaporated at RH=90%, in which the complete drying took almost 315 minutes with Pe_e=10.

I further cut the supraparticles to image the interior. Figure 3.11 (left) below depicts several buckled supraparticles obtained at a slower evaporation rate (Pe_e=10), with one of them cut to expose the interior. The ellipsoids oriented randomly inside the supraparticles [Figure 3.11 (right)] similar to those obtained at Pe_e=50 [Figure 3.4].

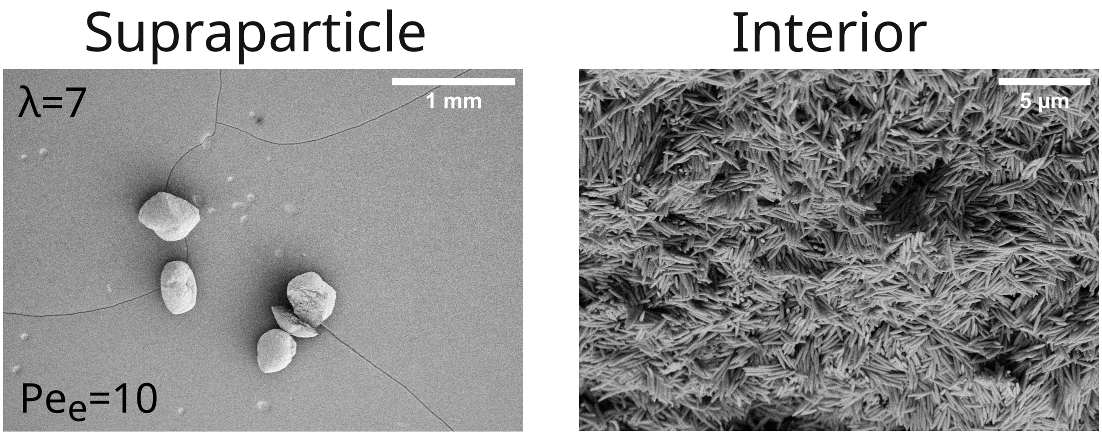

Figure 3.11: SEM image of many supraparticles and a cut supraparticle (left) composed of λ= 7 ellipsoids at Pe_e=10. SEM image on the right shows the interior structure of the supraparticles formed under the given conditions.

3.5 Buckled Supraparticles at Increased Initial Volume Fraction

The initial volume fraction of colloidal particles is another significant parameter that will determine the final supraparticle morphology. For instance, the morphology of 1% and 2% spray-dried alumina colloids was tuned from buckled doughnut-shaped into a sphere provided that the initial concentration was increased to 5%.[171] Increase of colloid volume fraction decreased the probability of buckling due to the inherent spatial constraint. A variety of final supraparticle shapes (pancakes, buckled clusters, and unbuckled spheroids, respectively) were obtained by evaporating droplets of PS colloids on superhydrophobic substrate when initial particle concentration increased systematically.[124] The prevention of buckling can be attributed to an effectively lower Pe at increased particle concentration. When a droplet with lower initial volume fraction reaches the same volume fraction as a droplet with higher initial volume fraction, the prior is already shrunken to a smaller size and is evaporating faster. This would mean a higher effective Pe at this point, which makes the droplet more prone to buckling.

Since increasing the initial colloidal volume fraction was previously shown to hinder buckling, I performed evaporation experiments with droplets that contained 8% initial volume fraction of PS spheres (408 nm in diameter) at RH=75%. I made these preliminary experiments with spherical colloids, as it was difficult to obtain high concentration of ellipsoidal particles with the used synthesis method. Nevertheless, the eight times-increased colloidal volume fraction did not lead to the formation of spherical supraparticles. The resultant supraparticles still showed a small buckled region [Figure 3.12].

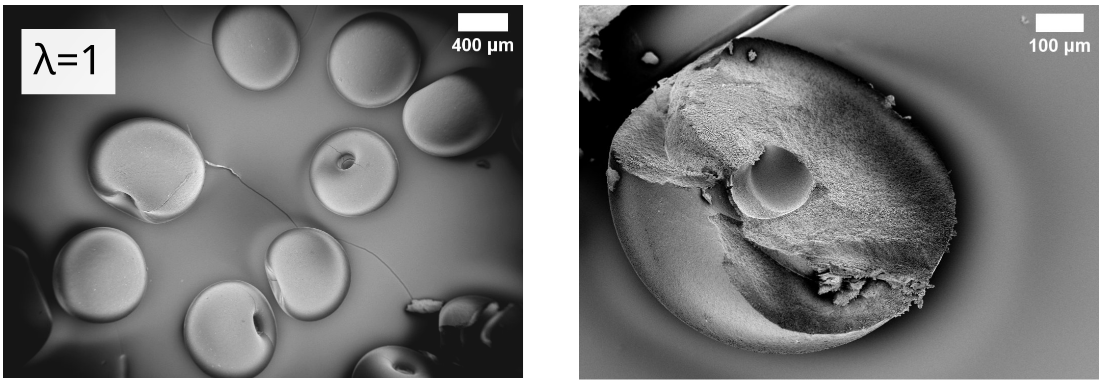

Figure 3.12: SEM images showing many supraparticles (left) and a supraparticle cut in half (right) composed of PS spheres (408 nm in size). The initial PS volume fraction was increased to 8%. The supraparticles were evaporated at RH=75%, in which the complete drying took almost 90 minutes.

3.6 Conclusions

Chapter 3 introduced an important phenomenon commonly observed in drying colloidal dispersions, which is the so-called buckling. Buckling indicated the formation of a shell layer at the receding droplet-air front, which later deformed into an irregular shape to release its stress. Buckling of supraparticles was observed with primary building blocks of different shapes, including λ= 4, 6, 11 ellipsoids and spheres. Each aspect ratio resulted in a different nonspherical final morphology of supraparticle with a wrinkled surface texture and a random orientation of ellipsoids in the interior (at $50 \leq Pe_e \leq 60$). Using spherical colloids somewhat improved the sphericity of the final supraparticle morphology, yet still showed a buckled region from the top. The binary supraparticles composed of sphere-ellipsoid mixtures also displayed a highly deformed final shape.

The effect of evaporation rate as well as initial volume fraction on the final supraparticle shape was further investigated. The evaporation rate was regulated by changing the humidity and was characterized through the dimensionless Péclet number, which was estimated by analyzing the evaporation videos. Decreasing the evaporation rate (Pe_e=10) was shown to reduce buckling but not preventing it completely for the pure-ellipsoid supraparticles. Moreover, the evaporation experiments done with spherical colloids at increased initial particle concentration still formed a buckled region.

Having tuned all the above-mentioned parameters, buckling was attributed to the insufficient colloidal stability of the dispersions used in the experiments. This was because buckling indicated the stress-induced deformation of the shell in case the attractive capillary forces dominated the stabilizing electrostatic forces between colloids. The formation and the subsequent deformation of this shell layer was further evidenced by the confocal experiments. The results suggest that buckling of supraparticles could be prevented by increasing the colloidal stability of the dispersion systems.

Chapter 4

Supraparticles with Spherical Morphology

4.1 Suppressing Buckling During Supraparticle Formation

Chapter 3 showed the influence of primary colloid shape, initial colloid volume fraction and evaporation rate on the formation of buckled supraparticles. Buckling was attributed to the formation of a shell due to the dominating attractive interactions between colloids. Towards the end of evaporation, the capillary stress caused by the shell became higher than the colloidal repulsive stress inside the droplet.[95] As a result, the shell buckled. Tsapis et al. even showed that the drying time until the onset of buckling could be shortened for levitated PS colloidal droplets once the net repulsive force between the colloids decreased with the addition of salt.[94]

This, of course, brought the idea of increasing the colloidal repulsive stress, i.e., increasing the stabilizing repulsive interactions between colloids. Colloids might carry surface groups that stabilize them against aggregation due to van der Waals forces.[56] These surface groups could be either polymer chains, which provide a short-range steric stabilization between the colloids, or charged groups.[56] The charged groups provide an electrostatic stabilization by dissociating in water. The range of this electrostatic barrier might vary from a few nanometers to a hundred nanometers, depending on the dissolved salt concentration.[56] In my experiments, PS colloids carried charged -COOH surface groups to ensure this electrostatic barrier. This was evidenced by their zeta potential of ≈ -59 mV. Yet, the electrostatic stabilization did not seem to be strong enough to prevent aggregation at high particle density. Even at slow evaporation kinetics (where Pe_e=10) the supraparticles ended with a buckled morphology due to colloidal aggregation on the droplet surface [Figure 3.10].

To increase the colloidal stability, i.e., to further increase the repulsive electrostatic interaction between the colloids, I added the anionic surfactant SDS to each dispersion. As surfactants are known to change interparticle interactions, they might be used in aggregation or stabilization of a system. For instance, an ionic surfactant like SDS provides electrostatic stabilization through electrostatic and steric effects.[172] SDS possesses a hydrophobic alkyl tail and a hydrophilic sulphate head [Figure 4.1]. The PS colloids used in the experiments were slightly hydrophobic in nature. Hence, once SDS was added to the aqueous dispersion, its hydrophobic alkyl tail adsorbed on the PS colloids. The electrostatic repulsion between the polar sulphate head groups of SDS prevented aggregation and kept the PS colloids well dispersed. It should be noted here that not all SDS might be adsorbing on the PS colloids. Some excess SDS might adsorb at the air-water interface with the hydrocarbon chains oriented towards the vapor phase.[173] However, we cannot observe the adsorption behavior of the surfactant inside the evaporating droplet directly. The adsorbed surfactant layers are usually only a few nanometers thick.[174] This would mean that we cannot detect them with SEM.

SDS concentration continuously increased, as water evaporated. This increase in concentration actually increases the capability of SDS to solubilize another hydrophobic substance like PS.[173] However, this would be limited by the very high concentrations. Above the critical micelle concentration (which is about 8 mM for SDS[175]) the non-adsorbed surfactant can behave similarly to a polymer which induces depletion attraction between the colloids.[176] When two colloids approach each other in a solution of non-adsorbed surfactant, the smaller surfactant is excluded from the vicinity of the larger colloids. Consequently, the increased osmotic pressure in the liquid medium surrounding the colloids causes them to

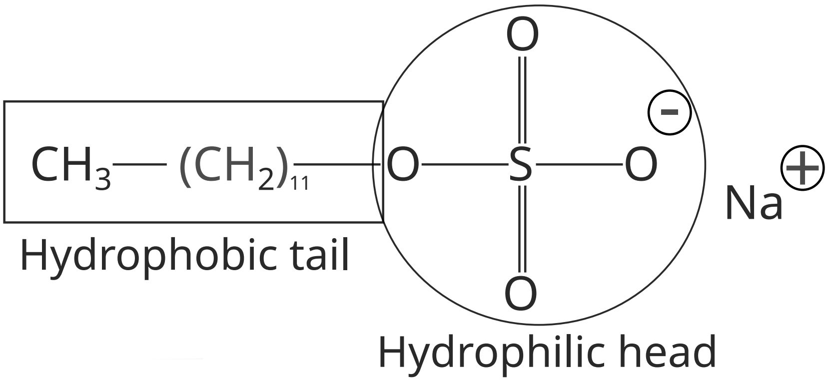

Figure 4.1: The molecular structure of the anionic surfactant sodium dodecyl sulphate (SDS) shown with its hydrophobic alkyl tail and a hydrophilic sulphate head.

aggregate via attractive depletion forces.[176] During the evaporation experiments, the concentration of SDS increased from 1 mM up to almost 240 mM. Yet, any destabilization, as proposed by such depletion mechanism, was not observed, since the droplets maintained their spherical morphology throughout evaporation. This showed that the addition of SDS increased the colloidal stability of the dispersion droplets. It is also plausible that the presence of SDS changed the nature of any shell that might form to be more permeable and less rigid so that it can reconfigure its shape instead of buckling.

I did some trial experiments to figure out the initial SDS concentration required to stabilize the dispersions. While doing so, I calculated the increase of surface area of an ellipsoid, relative to that of a sphere. To reach the same surface coverage as for a sphere with the same volume, I needed 50%, 75%, and 160% more surfactant, for ellipsoids of λ= 4, 6, and 11, respectively. The spherical PS colloids were already stabilized with 0.1 mM SDS. This required the use of 0.15 mM, 0.175 mM, and 0.26 mM SDS for ellipsoids of λ= 4, 6, and 11, respectively. These estimated surfactant concentrations, however, were not sufficient to prevent buckling especially for ellipsoids of λ= 6 and 11. In the end, all dispersion systems were well stabilized with 1 mM SDS. While doing these systematic experiments, I kept the SDS concentration well below 3 mM, as above this concentration the surface tension decreased significantly.[177] After stabilizing the dispersion droplets with 1 mM SDS, the obtained supraparticles resulted in

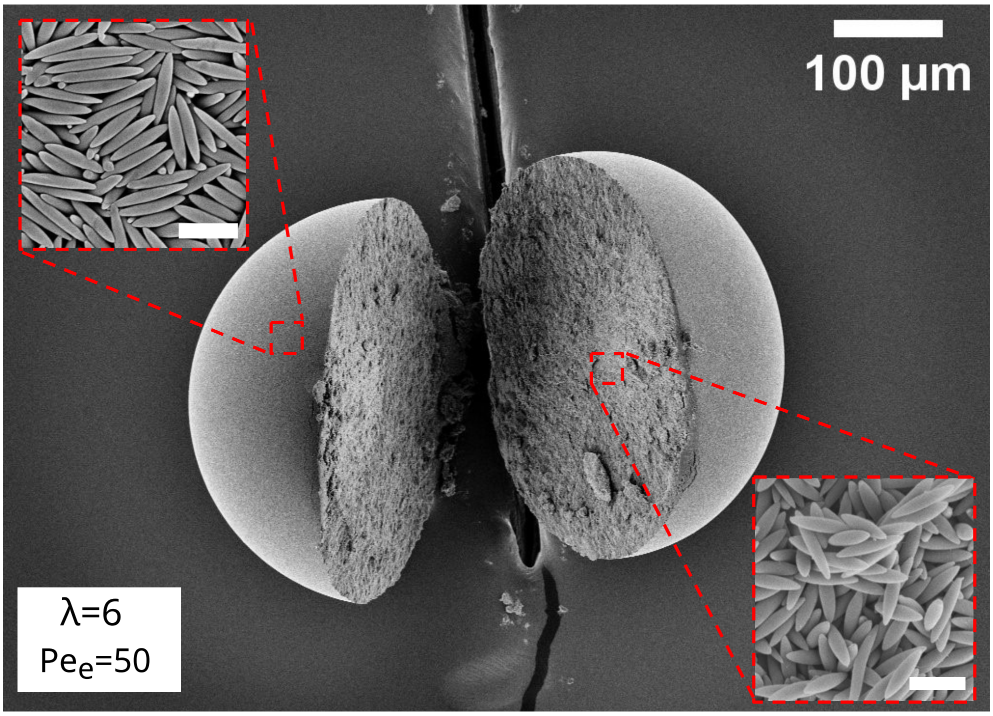

Figure 4.2: SEM image of a cut supraparticle showing the final spherical morphology after stabilizing the dispersion droplets with SDS. The supraparticle in the image was composed of λ= 6 ellipsoids and obtained at Pe_e=50. Insets show the supraparticle surface and interior at higher magnification. Scale bar in the insets corresponds to 1 μm. Reprinted with permission from[151]. Copyright 2024 American Chemical Society.

an almost spherical shape, for all the aspect ratios investigated [Figure 4.2].

4.2 Buckling Re-Initiated at Fast Evaporation

The role of evaporation rate on the final morphology was already discussed in Subchapter 3.4. Therefore, it was worth questioning whether the final shape of SDS-stabilized dispersion droplets of PS ellipsoids could be altered at faster evaporation kinetics. Aqueous dispersion droplets of λ= 4, 6, and 11 ellipsoids were evaporated at RH=30% on superamphiphobic surfaces, leading to 170$\leq Pe_e \leq$200. The decrease of humidity, i.e., the increase of evaporation rate, re-initiated the buckling of stabilized-droplets near the end of evaporation. Faster advection of air-water interface facilitated the formation of a shell and prevented the relaxation of accumulated colloids by diffusion. As a result, the final supraparticles were not spherical anymore [Figure 4.3(a-c)]. Buckling typically occurred from the top.

The ellipsoids on the buckled supraparticle surface did not seem to align much [Figure 4.3(d-f)]. A lot of ellipsoids oriented out of plane on the supraparticle surfaces.

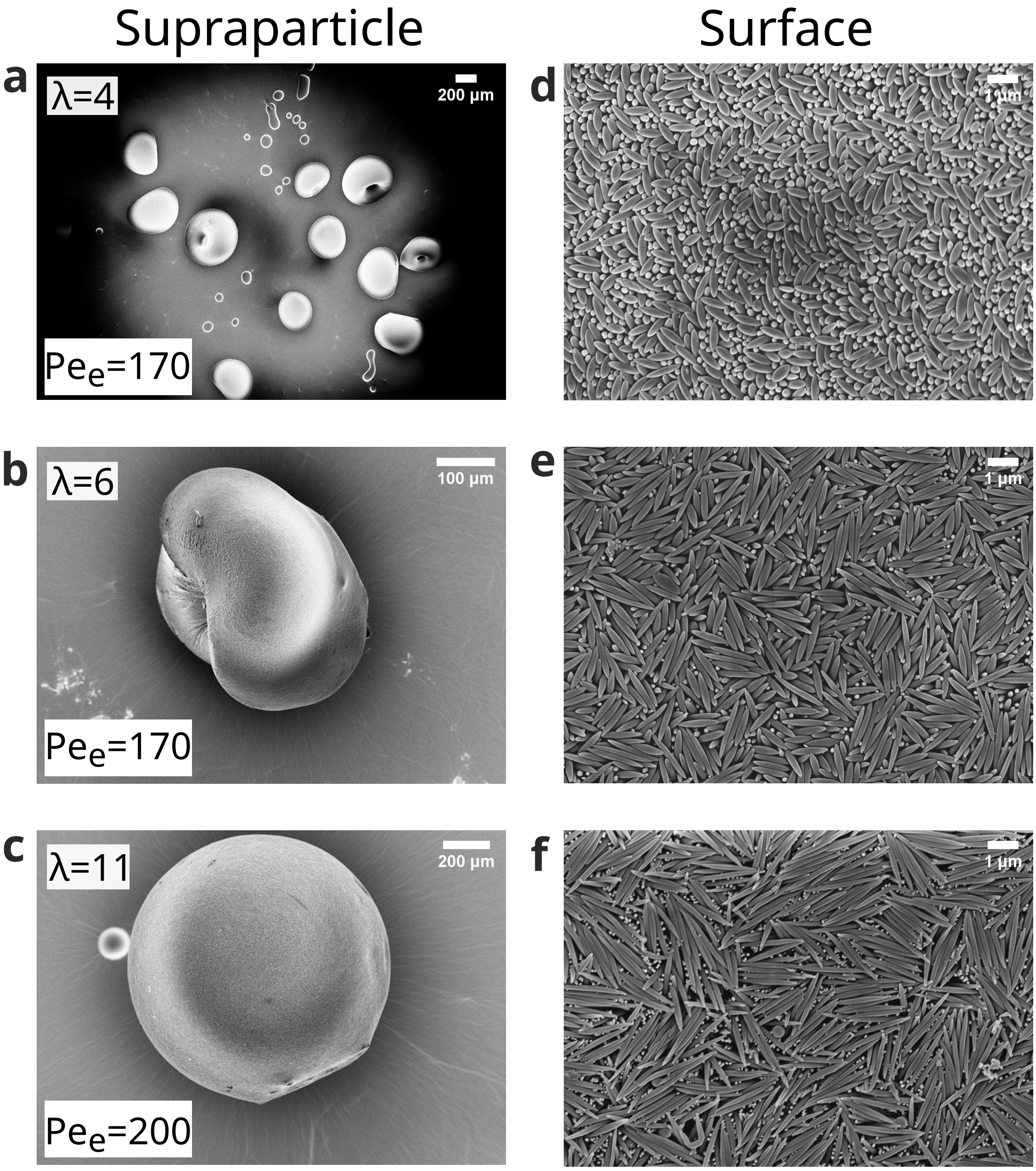

Figure 4.3: SEM images showing the final supraparticle morphology and their corresponding surfaces, composed of ellipsoids of $\lambda=$ (a,d) 4, (b,e) 6, and (c,f) 11. The dispersion droplets contained 1 mM SDS. The supraparticles were evaporated at RH=30%, in which the complete drying took almost 30 minutes with $170 \leq Pe_e \leq 200$. Reprinted with permission from[151]. Copyright 2024 American Chemical Society.

4.3 Surface Ordering of Ellipsoids

The orientational order of anisotropic colloids has a significant impact on many technological applications. An evident example of this is liquid crystals, where the orientation of elongated rod-like molecules dictates the macroscopic behavior of a sample.[178] The long-range orientational order (as in a nematic phase) that anisotropic colloids like ellipsoids displays is usually accompanied by a remarkable change in material's elastic, optical or conductivity properties along the direction of orientation.[178;179] Therefore, to gain control over the orientation of ellipsoids is required in many devices.

Prompted by this reasoning, I examined the supraparticle surfaces with SEM. As of now, the surfaces were easier to evaluate, since the spherical supraparticles had a smooth texture with most ellipsoids oriented in plane. Figure 4.4(a-c) shows the supraparticle surfaces composed of ellipsoids of λ= 4, 6, and 11. The ellipsoids showed a short-range lateral ordering upon drying at RH=75% with $40 \leq Pe_e \leq 70$. Most ellipsoids oriented in plane on the supraparticle surfaces. The supraparticle that showed the most out of plane oriented ellipsoids was the one with the highest aspect ratio (λ= 11).

To quantify the ordering of the ellipsoids on the supraparticle surface, the orientational order parameter $S^\dagger$ was computed as follows,[151]

$$S^\dagger(\mathbf{r}_i, \mathbf{r}_j) = \langle 2\cos^2\theta_{ij} - 1\rangle \tag{4.1}$$

where θ_{ij} is the angle between the long axes of two ellipsoids i and j, whose centers of mass are separated by distance $r = \mid \mathbf{r}_j - \mathbf{r}_i \mid$ with $\mathbf{r}_i$ being the position of ellipsoid i. The orientational order parameter was calculated using the surface SEM images of supraparticles. The interior ordering of ellipsoids could only be observed visually. This was because the supraparticle cross-sections resulted in a rough, non-planar interface due to the random breakage of the supraparticles during cutting. $S^\dagger = 1$ indicates a fully parallel ordering of ellipsoids, whereas $S^\dagger = 0$ would mean a random configuration.[151] The lateral and longitudinal ordering of the ellipsoids was plotted on a spatially resolved two-dimensional heat map as in Figure 4.4(d-f) below. The width and height of each cell on the heat map corresponded to the diameter (d_e) and length (L) of one single ellipsoid, respectively. This way, adjacent cells represented adjacent ellipsoids.

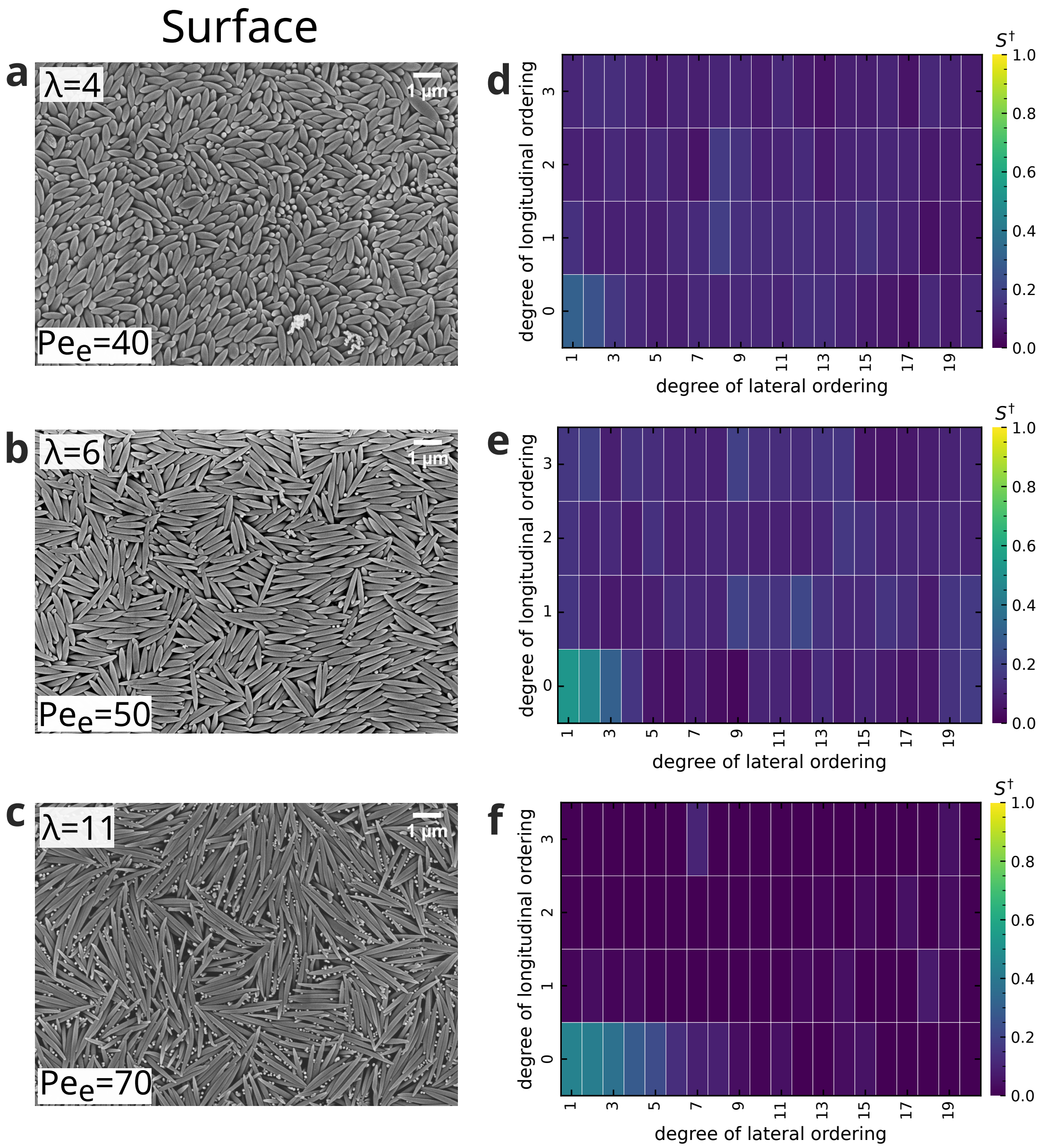

Figure 4.4: SEM images of supraparticle surfaces composed of $\lambda=$ a) 4, b) 6, c) 11 ellipsoids. The supraparticles were obtained at $40 \leq Pe_e \leq 70$. The 2D heat map for the orientational order parameter $S^\dagger$ (d-f), computed from the corresponding surface images shown in (a-c). Reprinted (adapted) with permission from[151]. Copyright 2024 American Chemical Society.

The 2D heat map in Figure 4.4(d-f) was computed using the SEM images of the supraparticle surfaces shown in Figure 4.4(a-c) for the supraparticles composed of $\lambda=$ 4, 6, and 11 ellipsoids, respectively. Accordingly, no ordering was found for $\lambda= 4$ (Pe_e=40). For $\lambda= 6$ (Pe_e=50), the ellipsoids were ordered along the short axis up to three ellipsoid diameters. For $\lambda= 11$ (Pe_e=70), the ordering along the short axis increased to about four ellipsoid diameters. The ellipsoids did not show any ordering along their long axis direction irrespective of the aspect ratio.

Now, the question that emerged naturally was whether we could change the ordering of ellipsoids on the supraparticle surface. Therefore, we wanted to understand if and to what extent the evaporation rate could influence the surface structure. For that reason, our collaborators [redacted] and [redacted] performed computer simulations of drying droplets composed of rods both in the evaporation- ($Pe \gg 1$) and diffusion-limited regime ($Pe \leq 1$).[151] Simulations were performed with and without including hydrodynamic interactions, which yielded nearly identical structures. Hence, simulations could be carried out with excluded hydrodynamic interactions, which enabled larger scale simulations with droplets of radius $R_0= 100d_e$.

The experimental and simulation results could be compared, since the corresponding Péclet numbers are on the same order of magnitude. The results are largely in good agreement [Figure 4.4 and 4.5] with some differences.[151] The simulation model considers a purely repulsive harmonic potential at the droplet-air interface, which might be suppressing the out of plane orientation of colloids observed in the experiments. In addition to that, simulations model the ellipsoids as (nearly) hard rods which would influence the packing behaviour.

The evaporation-limited regime that was investigated with the simulations ($70 \leq Pe_e \leq 140$) [Figure 4.5(a-c)] showed small, ordered bundles of rods on the supraparticle surfaces in all cases. Orientationally ordered clusters of rods are colored differently to distinguish them on the supraparticle surface. The diffusion-limited regime (Pe_e=1) showed long-range orientation of rods along their short and long axis directions [Figure 4.5(d-f)]. This dramatic increase in particle orientation can be explained by the entropy-driven ordering of liquid-crystalline phases, as first introduced by Onsager.[180] Onsager's theory states that at sufficiently high concentrations hard rods interacting with repulsive forces may show orientational ordering and prefer to align nematically. Because the increase in

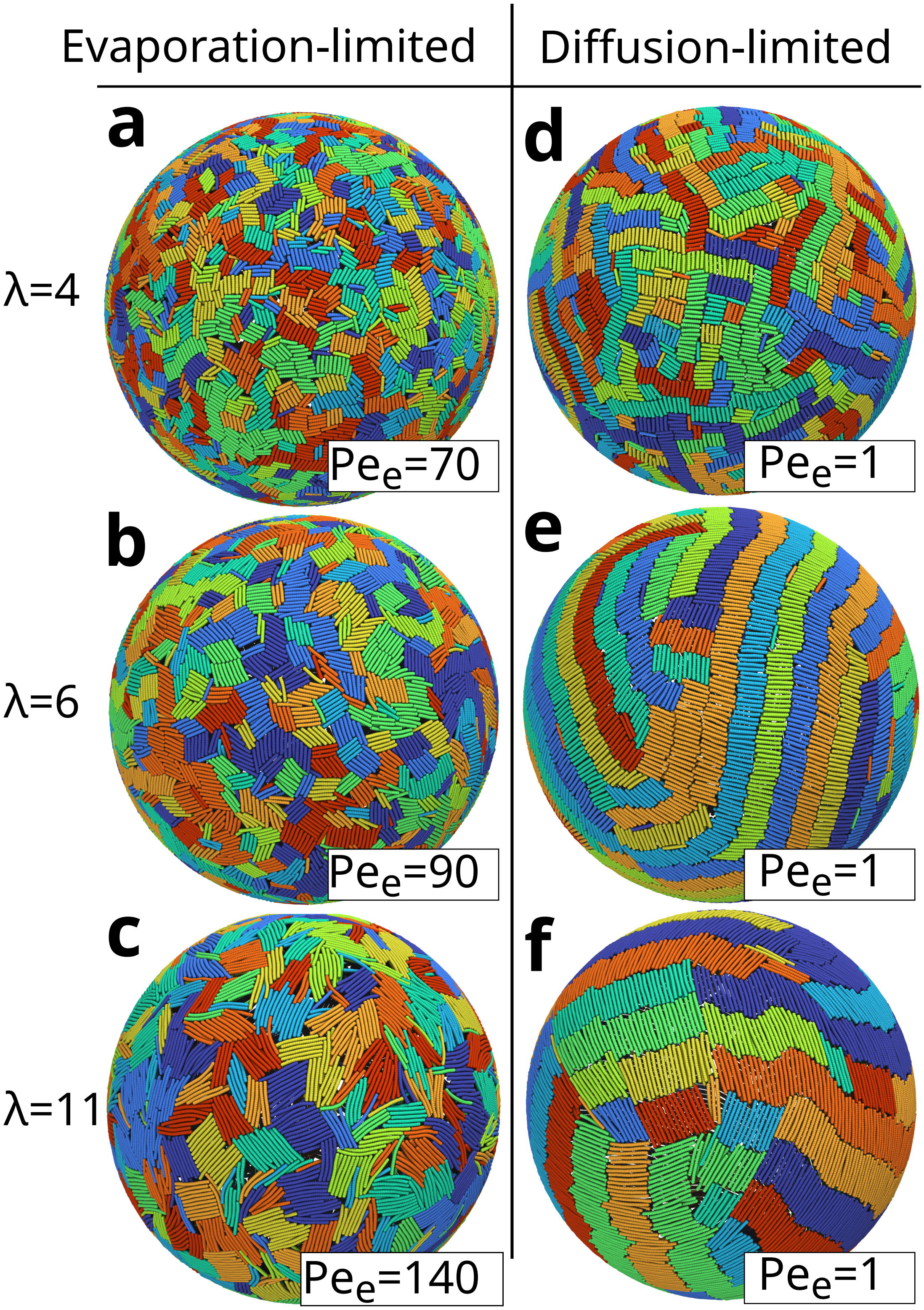

Figure 4.5: Simulation snapshots showing the supraparticle surfaces obtained in the (a-c) evaporation-limited ($Pe \gg 1$) and (d-f) diffusion-limited ($Pe \leq 1$) drying regimes for λ= 4, 6, and 11 rods (from top to bottom). Orientationally ordered clusters of rods are shown in different colors to guide the eye. Reprinted with permission from[151]. Copyright 2024 American Chemical Society.

translational entropy owing to particle alignment dominates over the loss in orientational entropy. Monte Carlo simulations indicated that the nature of this isotropic-nematic transition differed depending on the aspect ratio.[181] For short rigid rods (of aspect ratio of about 5) the transition has a weak first-order character. Therefore, at a certain compression, it resulted in small nematic clusters of each having its own orientation.[181] For longer rigid rods (of aspect ratio of about 15), however, the isotropic-nematic transition is strongly first-order. This allowed the spontaneous transformation of the whole isotropic phase into the nematic phase with a nearly uniform orientation.[181] Increasing the aspect ratio decreases the concentration at which this transition takes place.[182] It is important to note that Onsager's theory describes a bulk system at equilibrium, so it is not sufficient to fully explain the non-equilibrium behavior of drying droplets. The decrease of the range of ordering observed at $Pe \gg 1$ could be explained by rods not finding enough time to reorient when the droplet was dried fast.[151]

The simulation results suggested that the extent of surface ordering of rods depended strongly on the drying kinetics. For this reason, we further calculated the radially averaged $S^{\dagger}$ of rods on the supraparticle surface at varying Péclet numbers [Figure 4.6]. The largest Péclet numbers ($70 \leq Pe_e \leq 140$) used in the simulations matched quite well with the experiments done at RH=75% ($40 \leq Pe_e \leq 70$), which are shown as dashed lines on the plots. The range of orientational ordering of rods increased rapidly with increasing aspect ratio. In line with the experiments, $\lambda = 4$ rods exhibited on average no lateral ordering [Figure 4.6(a)]. The $\lambda = 11$ rods showed long-range ordering, which decayed with increasing Péclet numbers [Figure 4.6(c)].

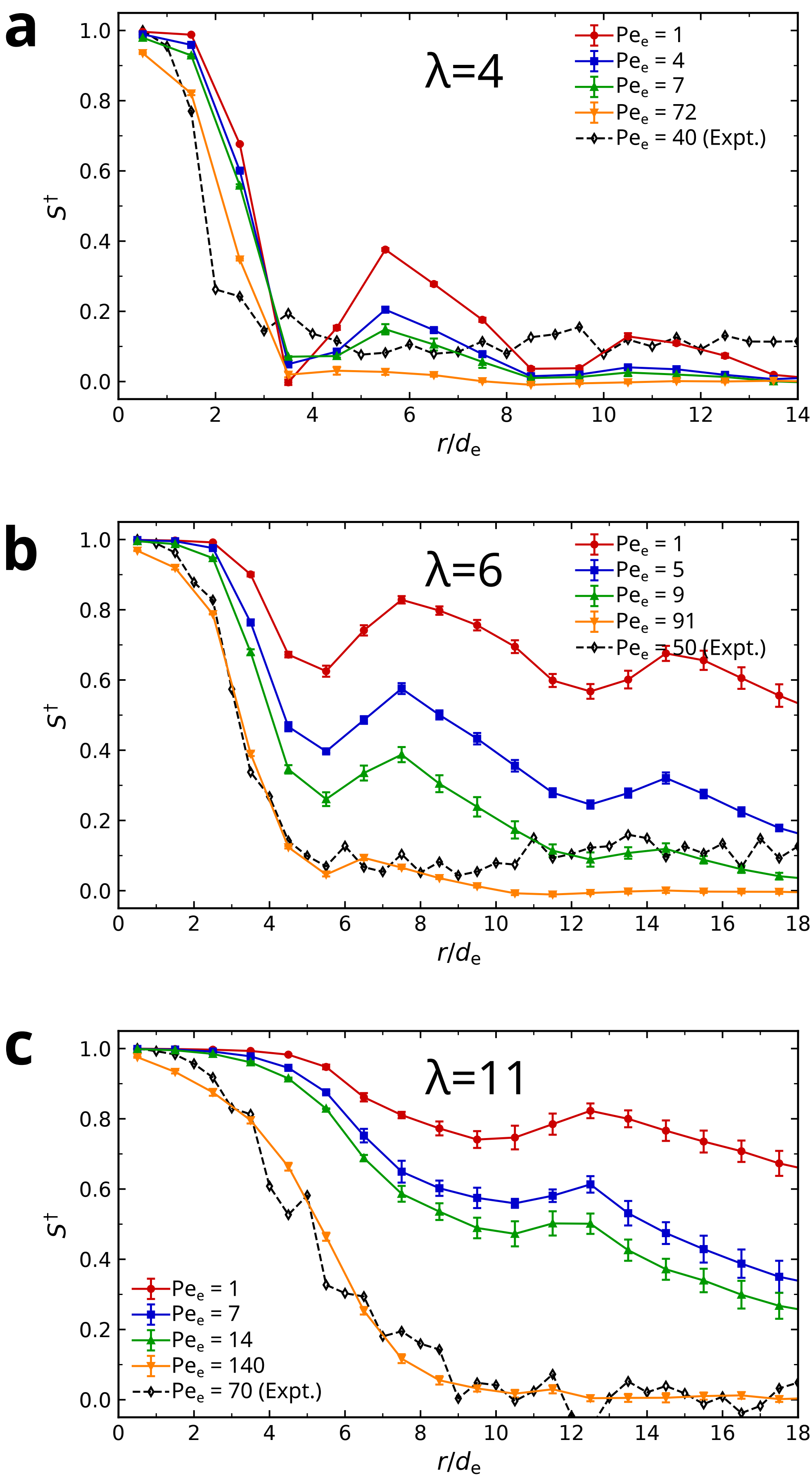

Figure 4.6: Plots showing the Péclet number dependence of orientational order parameter for rods of λ= a) 4, b) 6, and c) 11. The experimental results are plotted with dashed lines. Reprinted with permission from[151]. Copyright 2024 American Chemical Society.

Thus far, the simulations showed that we could increase the surface ordering of elongated colloids in the direction of diffusion-limited regime. Hence, I performed experiments under slower evaporation kinetics at RH=90% and reached to Pe_e=10, as described previously. After stabilizing the dispersion droplets with SDS, the supraparticles formed an almost spherical morphology [Figure 4.7(a)] at Pe_e=10 with a smooth surface [Figure 4.7(b)]. The 2D heat map [Figure 4.7(c)] quantified the ordering of λ= 7 ellipsoids on these surfaces. The orientational ordering of ellipsoids increased along both short and long axis direction compared to the buckled supraparticles at Pe_e=10 [Figure 3.10] and to the spherical supraparticles at 40≤Pe_e≤70 [Figure 4.4]. On these supraparticles, the lateral degree of ordering extended up to five ellipsoid diameters.

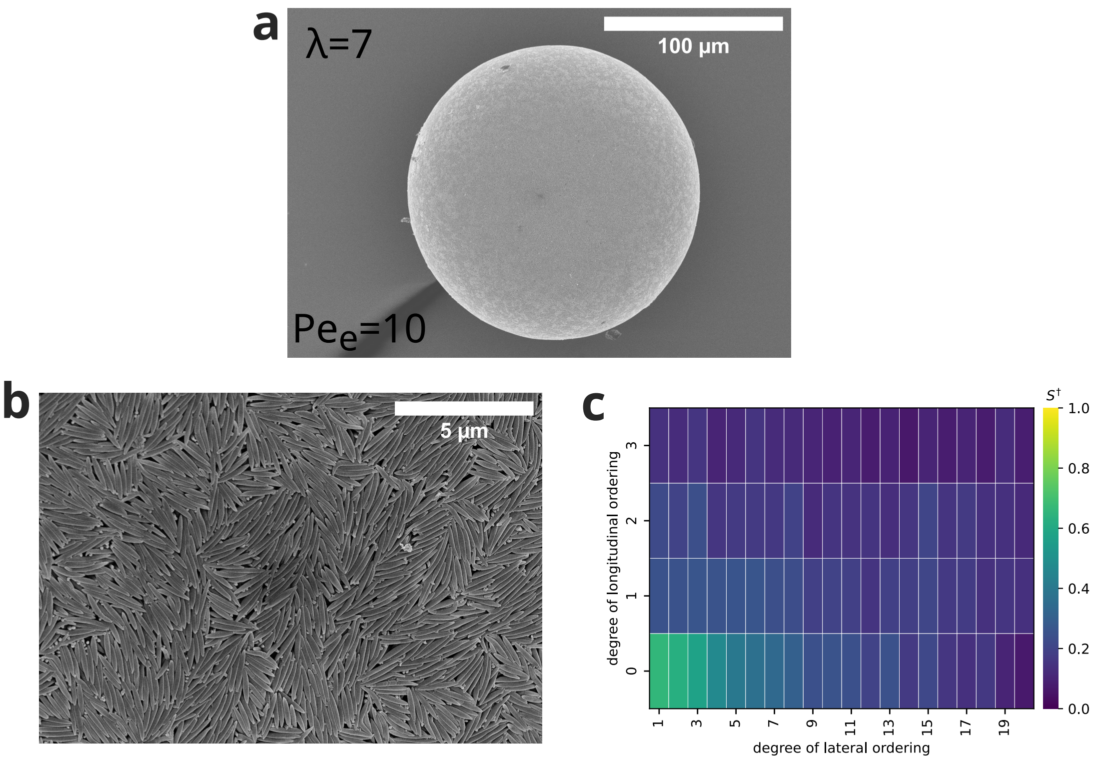

Figure 4.7: SEM images showing a) the final supraparticle morphology and b) the corresponding surface, composed of ellipsoids of λ= 7. The SDS-stabilized dispersion droplets were evaporated at RH=90%, leading to Pe_e=10. c) The 2D heat map for the orientational order parameter $S^\dagger$ was computed using the surface image shown in b).

4.4 Interior Ordering of Ellipsoids

The ordering of ellipsoids inside the supraparticles was imaged by SEM after cutting the supraparticles with a scalpel. The buckled supraparticles at $10 \leq Pe_e \leq 60$ previously showed random distribution of ellipsoids in the interior [Figures 3.4 and 3.11]. Likewise, the cross-section images of spherical supraparticles at $40 \leq Pe_e \leq 70$ also revealed randomly packed ellipsoids irrespective of aspect ratio [see the inset in Figure 4.2 and Figure 4.8].

Experiments[183] and simulations[184] of bulk systems have shown that the random packing of rod-like particles typically forms more open structures in comparison to that of spherical particles. Moreover, increasing the aspect ratio has been shown to decrease the packing efficiency of oriented elongated particles.[183] With this in mind, we computed the packing volume fraction ϕ of ellipsoids inside the supraparticles as a measure of porosity.[151] In order to calculate the packing volume fraction, we first estimated the initial and final droplet volume through image analysis, as described in Subchapter 2.7. Solid of revolution method was used to calculate the droplet volume, after determining an arc through the circumference of the 2D image of one half of the droplet. This method assumed rotational symmetry, but ruled out a specific droplet shape. Therefore, it canceled any systematic error coming from the deviation of sphericity.[151] The final volume fraction of ellipsoids inside the supraparticles was then computed as

$$\phi_f = \frac{\phi_0 V_0}{V_f} \tag{4.2}$$

where ϕ_0 is the initial colloid volume fraction and V_0 and V_f are the initial and final droplet volumes, respectively. Table 4.1 below shows the ϕ_f calculated for λ= 1, 4, 6, and 11, together with corresponding ϕ_0 and theoretically predicted values of random packing in bulk dispersions.[151] The supraparticles composed of spherical colloids (λ= 1) were also calculated to set a reference point. As expected, the final volume fraction of ellipsoids decreased with increasing ellipsoid aspect ratio. The results were coherent with bulk simulation studies of randomly oriented rods.[184;185;186;187] The decrease in random packing efficiency of ellipsoids inside the supraparticles can be ascribed to the increase of orientationally averaged

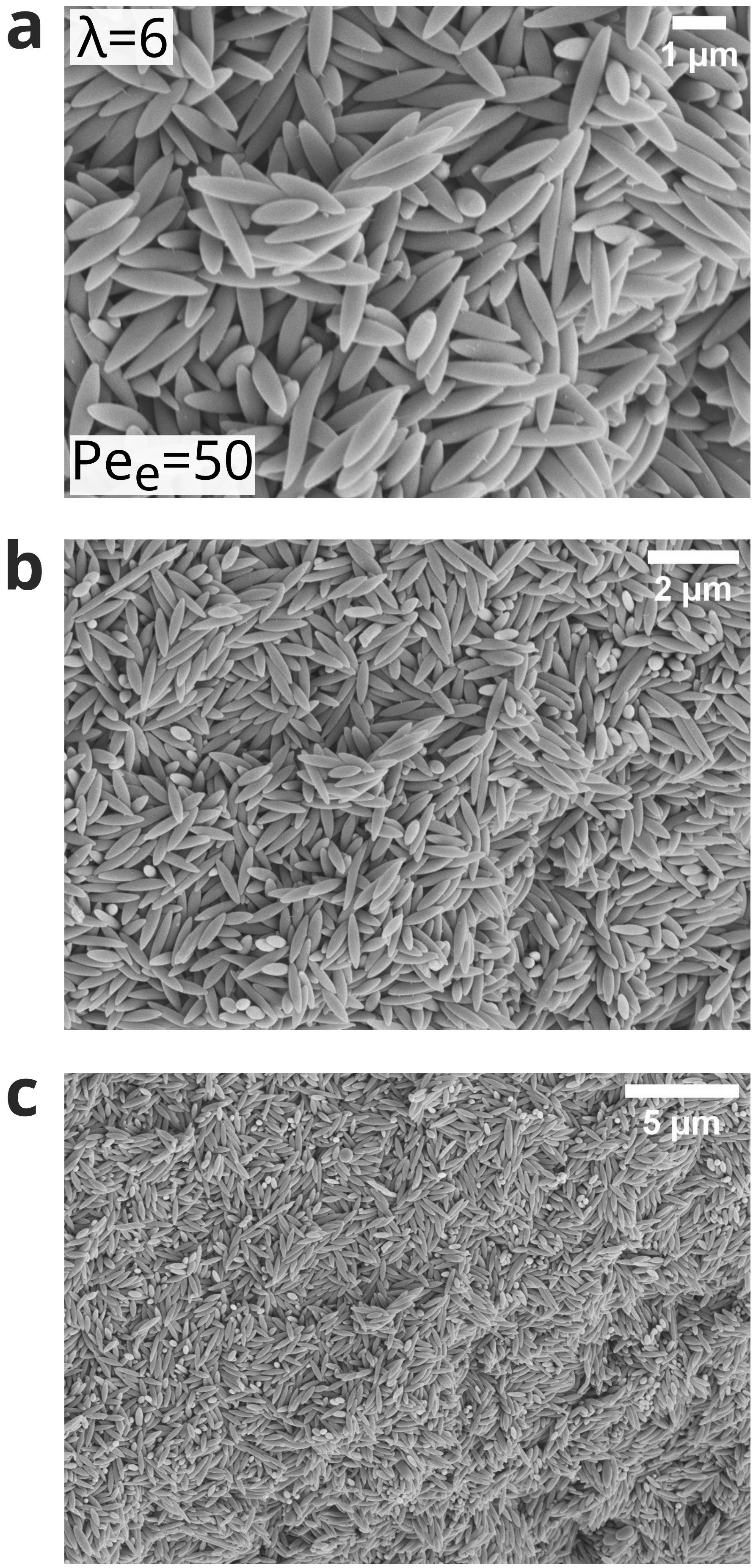

Figure 4.8: The cross-section SEM images of supraparticles composed of λ= 6 ellipsoids at Pe_e=50. Images show the same region of interest by zooming out from (a-c). Reprinted with permission from[151]. Copyright 2024 American Chemical Society.

excluded volume for particles with higher aspect ratios.[183;184] A sphere of diameter d can find its contacting neighbors in an excluded volume of order d^3.[183] For a rod of length L, the mechanical stability is ensured by about the same number of neighbors, however, with their centers in a much larger excluded volume of order dL^2.[183] Thus, the packing fraction will be essentially lowered. Our results suggest that the supraparticle porosity can be further increased (ϕ_f decreased) by assembling ellipsoids of higher aspect ratio.[151]

λ	ϕ_0	ϕ_f	Theoretically expected ϕ_f
1	0.011±0.001	0.61±0.06	0.66[184], 0.68[186;188], 0.69[187]
4	0.011±0.001	0.59±0.03	0.53[184], 0.55[186], 0.59[185], 0.61[187]
6	0.013±0.002	0.57±0.08	0.51[188], 0.55[187]
11	0.081±0.001	0.52±0.04	0.40[188], 0.43[186], 0.44[185], 0.48[187]

Table 4.1: Final volume fractions of spheres and ellipsoids composing the supraparticles at $10 \leq Pe \leq 70$. The last column corresponds to the theoretically estimated values of random packing in bulk dispersions. Reprinted with permission from[151]. Copyright 2024 American Chemical Society.

Simulations of the supraparticle cross-sections performed in the evaporation-limited regime ($70 \leq Pe_e \leq 140$) indicated the random orientation of rods in the interior [Figure 4.9(a-c)], just as in the experiments. On the other hand, the simulations in the diffusion-limited regime ($Pe \leq 1$) showed local nematic ordering of rods inside the supraparticles [Figure 4.9(d-f)]. The change in particle orientation can be attributed to the entropy-driven isotropic-nematic transition of elongated particles, as already discussed in Subchapter 4.3. This transition requires the reorientation of individual particles and nematic bundles, which is more probable when the droplet is dried slowly, i.e., $Pe \leq 1$.[151] Having observed orientationally ordered bundles of rods inside the supraparticles, our collaborators computed the global nematic order parameter of the drying droplet at various stages and compared this to the bulk simulations of rods.[151] The bulk simulations indicated an isotropic-nematic transition for rods of all aspect ratio, where there was a decreasing tendency in the volume fraction of the transition with increasing λ. Further, the simulations of the drying droplets suggested that the long-range nematic ordering of rods was hindered because of the spherical confinement. The finding was consistent with prior studies of confined nematic systems.[144;189] Nevertheless, small nematic bundles were observed at volume fractions close to those of isotropic-nematic transition in bulk.

The SDS-stabilized supraparticles prepared under slower evaporation kinetics at Pe_e=10 (at RH=90%) showed the local nematic ordering of ellipsoids in the interior [Figure 4.10]. Interestingly, this increase of orientation was only observed after the stabilization, as ellipsoids oriented randomly inside the buckled supraparticles formed at Pe_e=10 [Figure 3.11]. The orientational ordering of ellipsoids during evaporation could be suppressed with increasing Péclet numbers as well as confinement. Hence, we observe local nematic ordering of elongated particles in the interior at Pe_e=10 with the experiments and $Pe \leq 1$ with the simulations.

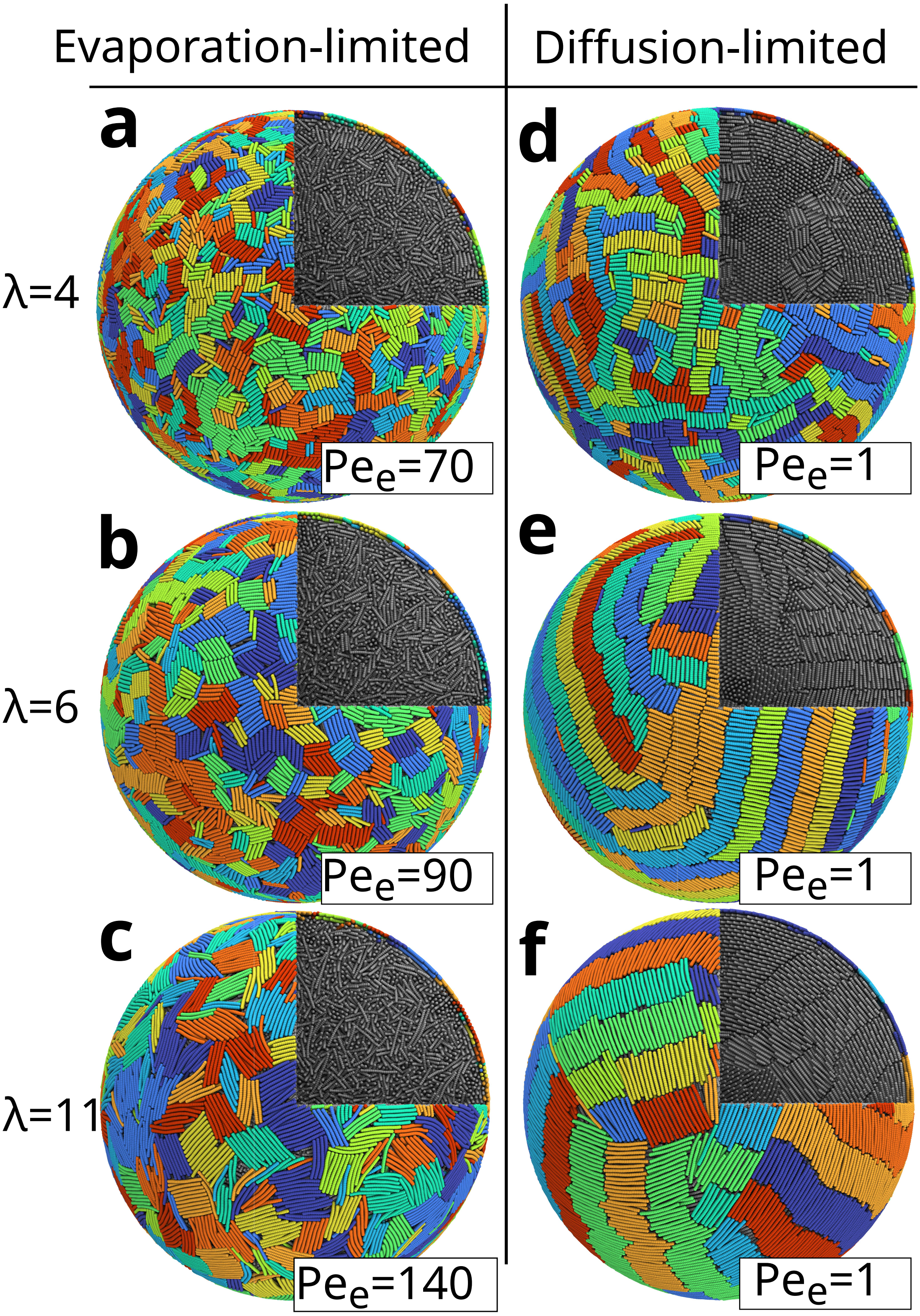

Figure 4.9: Simulation cross-sections are shown with the upper right corner of each supraparticle obtained in the (a-c) evaporation-limited ($Pe \gg 1$) and (d-f) diffusion-limited ($Pe \leq 1$) drying regimes for λ= 4, 6, and 11 rods (from top to bottom). Reprinted with permission from[151]. Copyright 2024 American Chemical Society.

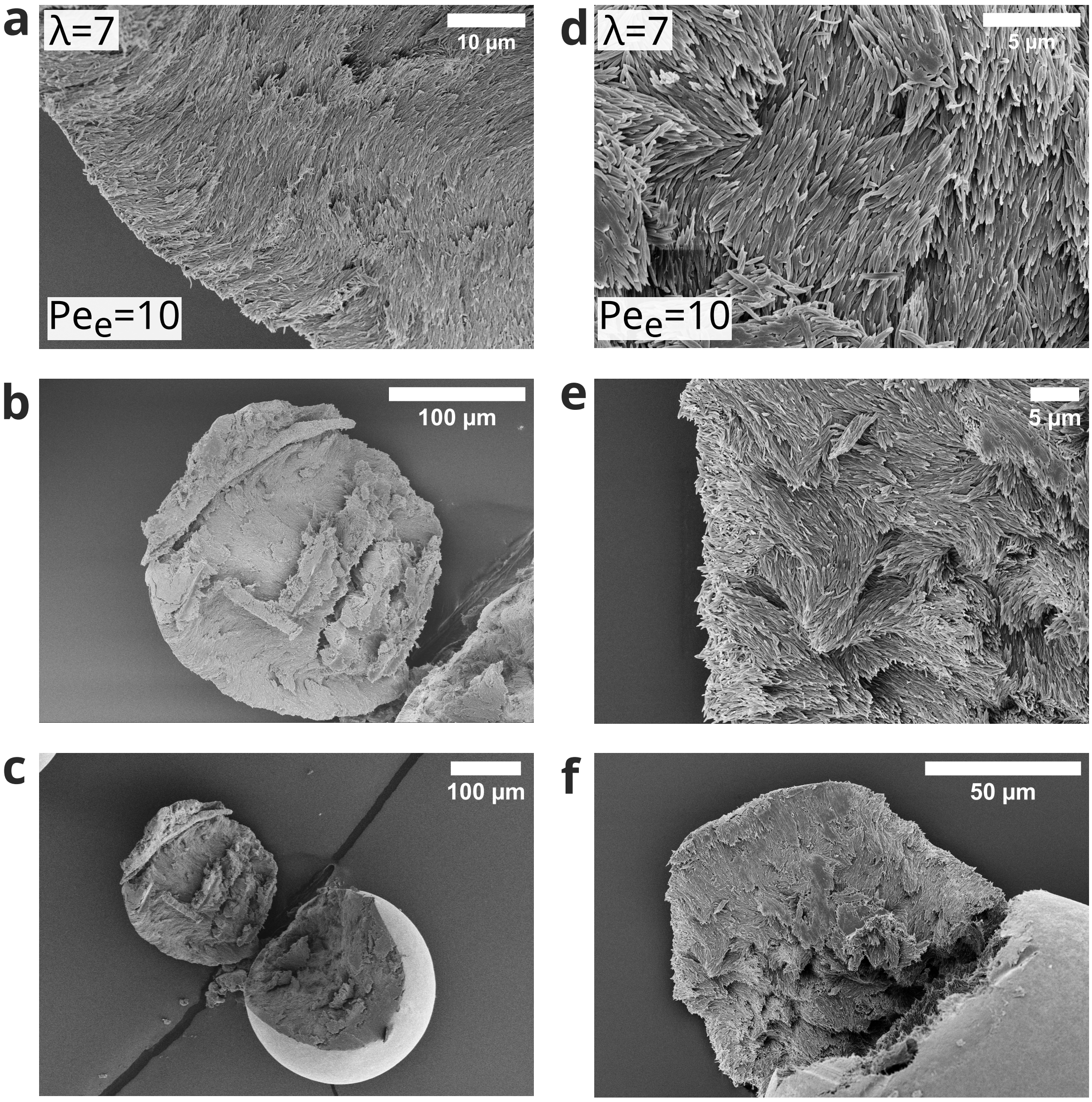

Figure 4.10: The cross-section SEM images of supraparticles composed of λ= 7 ellipsoids at Pe_e=10. Images show the supraparticle interior by zooming out from (a-c) and (d-f).

4.5 Conclusions

Since the prior experimental results conveyed the colloidal instability as the cause of buckling, the stability of the dispersions was increased with the addition of SDS. SDS increased the repulsive interactions between colloids and suppressed buckling. As a result, spherical supraparticles, showing smooth surface texture, were obtained starting from ellipsoids of varying aspect ratio, spheres, and sphere-ellipsoid mixtures. Increasing the evaporation rate (with $170 \leq Pe_e \leq 200$) was shown to re-induce the buckling of pure-ellipsoid supraparticles.

The orientational ordering of ellipsoids on supraparticle surfaces and interiors was studied, as this was relevant in many technological applications, such as optics. The ellipsoids only showed short-range lateral ordering on the surface and no ordering along their long axis ($40 \leq Pe_e \leq 70$). This lateral ordering of ellipsoids tended to increase with increasing aspect ratio. Complementary drying simulations were performed for a broad Péclet range, which suggested a strong influence of drying rate on the surface ordering of rods. The evaporation-limited regime ($70 \leq Pe_e \leq 140$) displayed small, ordered bundles of rods, whereas the diffusion-limited regime ($Pe \leq 1$) showed the long-range surface ordering of rods. Along the same lines, with the experimental supraparticles that were obtained at the slowest evaporation rate (Pe_e=10), the lateral degree of ordering extended up to five ellipsoid diameters on the surface. This increase in ellipsoid ordering can be explained by the increase of the overall entropy, analogous to the isotropic-nematic transition observed with liquid-crystalline phases. However, the formation of nematic ordering could be suppressed with increasing drying rate as well as spherical confinement.

In the evaporation-limited regime, the spherical supraparticles showed random interior ordering of ellipsoids (at $40 \leq Pe_e \leq 70$) both for experiments and simulations (at $70 \leq Pe_e \leq 140$). The final packing fraction of ellipsoids inside the experimental supraparticles decreased with increasing aspect ratio, which conveyed the possibility of controlling supraparticle porosity. The local nematic ordering of rods observed with the drying simulation cross-sections in the diffusion-limited regime ($Pe \leq 1$) was also achieved in the interior of the pure-ellipsoid supraparticles at Pe_e=10.

All in all, the findings in Chapter 4 demonstrate (i) the importance of colloidal stability and evaporation speed in determining the final supraparticle shape, (ii) the potential to control the degree of ordering of ellipsoids (and rods) by tailoring their aspect ratio and/or the evaporation rate, (iii) regulating the supraparticle porosity by changing the ellipsoid aspect ratio.

Chapter 5

Binary Supraparticles with Spherical Morphology

5.1 Motivation behind Using Binary Mixtures

Utilizing components of different shapes, e.g, sphere-ellipsoid mixtures, increases the intricacy of the assembly process. To date, equilibrium conditions have shown the phase separation of sphere-rod mixtures both experimentally and theoretically.[190;191;192] Phase separation happens when excluded volume effects lead to depletion interactions.[192] The strength and range of these depletion interactions depend on the size, aspect ratio and the concentration of the particles.[191]

The evaporation-induced self assembly of colloids is a non-equilibrium advection-diffusion process. Therefore, the established equilibrium concepts cannot fully predict the assembly pathway, but might be useful indeed. Confinement during the evaporation process creates an additional complexity. Confinement of binary mixtures can change the distribution and ordering of the components, which would alter the supraparticle properties.[149] For instance, simulation studies of sphere-rod mixtures confined between two hard walls showed the destabilization of orientational ordering of rods by spherical colloids.[138] Phase separation can be used in spherical confinement to produce a variety of multicomponent supraparticles such as Janus or core-shell supraparticles.[150] Previously, Xiao et al. induced phase separation in a binary mixture of magnetic ellipsoids and nonmagnetic spheres and obtained Janus photonic crystal supraparticles by the subsequent crystallization of ellipsoids.[193] Therefore, studying structure formation in binary supraparticles is complex and requires certain parameters such as ellipsoid aspect ratio, evaporation rate, and particle volume concentration to be addressed.

5.2 Supraparticle Surfaces at Different Evaporation Kinetics

Dispersion droplets of SDS-stabilized sphere-ellipsoid mixtures were evaporated on superamphiphobic surfaces by varying the relative humidity, which led to different Péclet numbers. In all cases, the obtained supraparticles formed an almost spherical morphology.[151] In Subchapter 5.2 and 5.3, the total initial volume fraction of colloids was 0.6% with equal volume ratio of the components v_e:v_s = 1. Drying conditions of binary mixtures were characterized using two Péclet numbers (Pe_e and Pe_s), as long-time self-diffusion coefficients of ellipsoids and spheres would differ. The surface SEM images were analyzed by counting the number of ellipsoids and spheres. Knowing the number and sizes of particles, their relative area fractions, denoted as σ_e for ellipsoids and σ_s for spheres, were calculated.

In the first set of experiments, supraparticles were prepared under higher humidity (at RH=75%), which led to $40 \leq Pe_e \leq 50$ and Pe_s=10. In this case, supraparticle surfaces were predominantly covered by the ellipsoids for all aspect ratios ($82 \leq \sigma_e \leq 96$ and $4 \leq \sigma_s \leq 18$) [Figure 5.1(a-c)]. In the second set of experiments, supraparticles were prepared under lower humidity (at RH=30%), which led to $120 \leq Pe_e \leq 200$ and $30 \leq Pe_s \leq 50$. The increase in evaporation rate drastically changed the distribution of the components on the supraparticle surface. Under such conditions, the surfaces were occupied by ellipsoids and spheres almost evenly [Figure 5.1(d-f)].

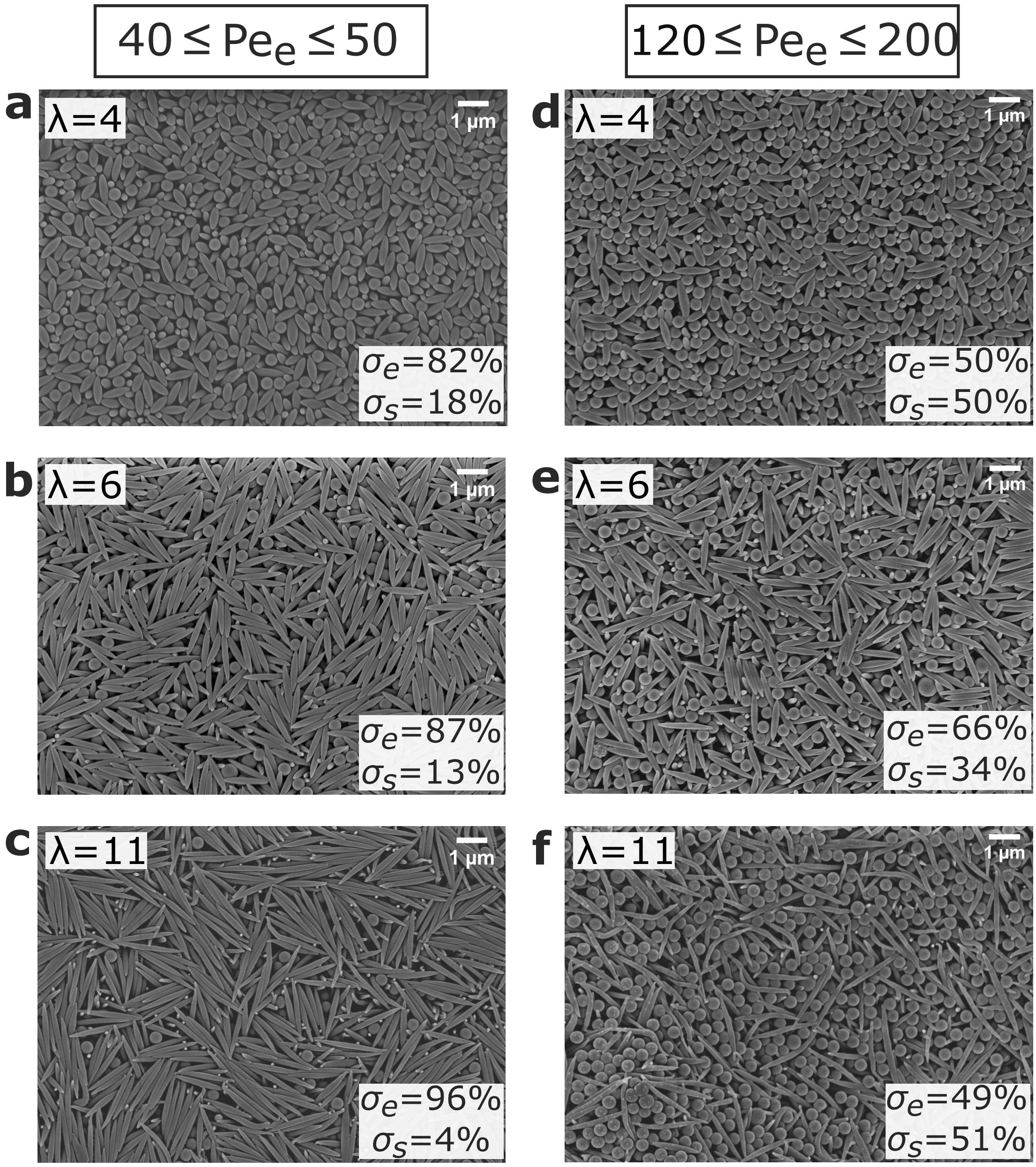

Figure 5.1: SEM images of the surface of supraparticles composed of sphere-ellipsoid mixtures, with ellipsoids having a) $\lambda=4$ (at Pe_e=40), b) $\lambda=6$ (at Pe_e=50), c) $\lambda=11$ (at Pe_e=50), d) $\lambda=4$ (at Pe_e=130), e) $\lambda=6$ (at Pe_e=120), and f) $\lambda=11$ (at Pe_e=200). The left column corresponds to slower evaporation experiments performed at RH=75%, whereas the right one shows faster evaporation experiments performed at RH=30%. The relative area fractions σ_e and σ_s are indicated on the SEM images. Reprinted with permission from[151]. Copyright 2024 American Chemical Society.

By slowing down the evaporation further, sphere-ellipsoid ($\lambda=7$) binary supraparticles were obtained at RH=90%, leading to Pe_e=15 and Pe_s=5. Figure 5.2 (left) depicts the spherical morphology of the cut supraparticle. As was the case with slower evaporation above, the surface was mostly occupied by ellipsoids with σ_e=86% and σ_s=14% [Figure 5.2 (right)].

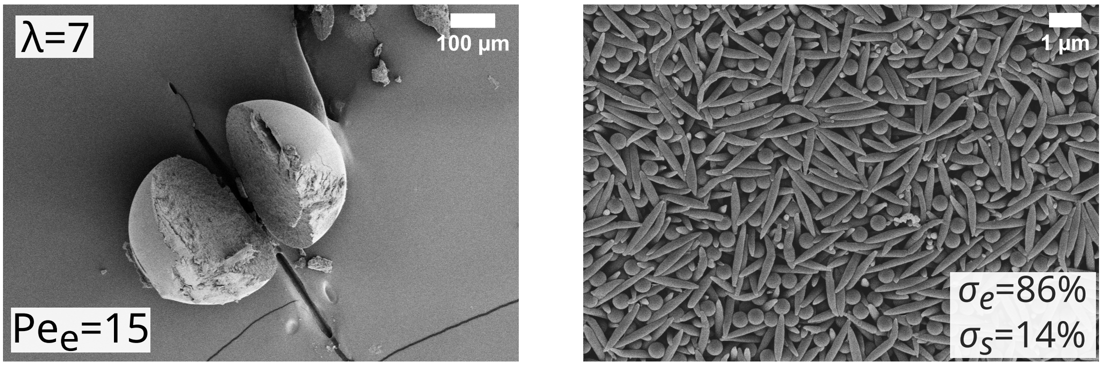

Figure 5.2: SEM images showing the final morphology of a binary supraparticle cut in half (left) and the corresponding surface (right), composed of λ= 7 ellipsoids. The evaporation experiments were performed at RH=90%, leading to Pe_e=15 and Pe_s=5. The relative area fractions σ_e and σ_s are indicated on the surface SEM image.

5.3 Supraparticle Interior at Different Evaporation Kinetics

The interior distribution of the constituent particles at different evaporation kinetics was imaged by SEM after cutting the supraparticles with a scalpel. Under higher relative humidity conditions (at RH=75% with 40$\leq Pe_e \leq$50 and Pe_s=10), i.e., slower evaporation rate, the cross-section images displayed a single layer of ellipsoids oriented parallel to the interface [Figure 5.3(b)]. This layer was followed by a homogeneous mixture of ellipsoids and spheres inside the supraparticle, independent of the ellipsoid aspect ratio [Figure 5.3(a)].[151] Upon evaporation under lower relative humidity (at RH=30% with 120$\leq Pe_e \leq$200 and 30$\leq Pe_s \leq$50), the single shell layer of the sphere-ellipsoid mixture was observed [Figure 5.3(c)]. Following this, ellipsoids and spheres showed a random distribution inside the supraparticles for all aspect ratios [Figure 5.3(d)].[151]

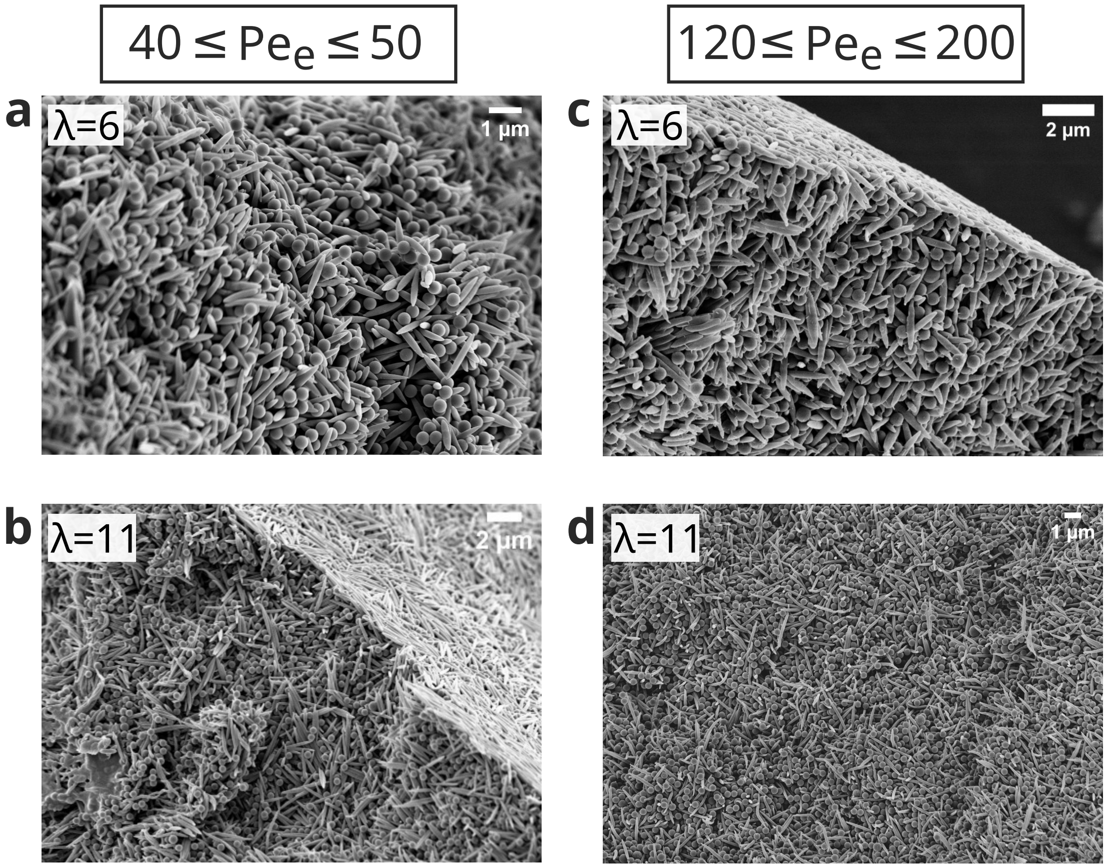

Figure 5.3: The cross-section SEM images of the supraparticles composed of sphere-ellipsoid mixtures, with ellipsoids having a) λ= 6 (at Pe_e=40), b) λ= 11 (at Pe_e=50), c) λ= 6 (at Pe_e=120), and d) λ= 11 (at Pe_e=200). The left column corresponds to slower evaporation experiments performed at RH=75%, whereas the right one shows faster evaporation experiments performed at RH=30%. Reprinted with permission from[151].

To analyze the effect of using binary mixtures on the final colloid volume fraction inside the supraparticles, we further calculated ϕ_f by performing image analysis of the evaporation videos as described in Subchapter 4.4. Table 5.1 shows the total initial volume fractions (ϕ_0) and the ϕ_f computed for slower and faster evaporation rates for sphere-ellipsoid mixtures (of λ= 4, 6, and 11 ellipsoids). Accordingly, ϕ_f exhibited a decreasing trend with increasing aspect ratio of ellipsoids in the binary supraparticles. The decrease in ϕ_f can be explained by the random orientation of ellipsoids, which restricts the packing of spheres. ϕ_f values obtained at faster evaporation rate (under lower relative humidity conditions) were slightly lower than those at slower evaporation rate. This showed that fast evaporation can prevent the systems from relaxing into a close-packed configuration.[151]

λ	ϕ_0	ϕ_f slow	ϕ_f fast
4	0.0066±0.0002	0.59±0.02	0.54±0.02
6	0.0066±0.0004	0.52±0.03	0.50±0.03
11	0.0066±0.0004	0.48±0.03	0.45±0.03

Table 5.1: Final volume fractions of binary supraparticles at slower evaporation rate ($40 \leq Pe_e \leq 50$ and $Pe_s = 10$) and at faster evaporation rate ($120 \leq Pe_e \leq 200$ and $30 \leq Pe_s \leq 50$). Reprinted with permission from[151]. Copyright 2024 American Chemical Society.

Drying simulations of sphere-rod mixtures were performed by our collaborators [redacted] and [redacted] to further examine the distribution of colloids at different Péclet regimes. The total initial volume fraction was set as $\phi_0 = 0.08$, with equal volume fractions of rods ($\phi_{0,e}$) and spheres ($\phi_{0,s}$). Simulations were performed with and without hydrodynamic interactions, as was the case for pure rod systems, however, no major differences were observed with the results.[151] Hence, the following simulation results excluded the hydrodynamic interactions between particles to save computing time.

One half of the cross-section snapshots below showed the evaporation-limited drying simulations ($70 \leq Pe_e \leq 140$) and the other half showed the diffusion-limited drying simulations ($Pe_e = 1$) for sphere-rod mixtures (of $\lambda = 4$, 6, and 11 rods) [Figure 5.4]. The evaporation-limited regime showed randomly packed rods inside the supraparticles with spheres filling the interstitial spaces. In contrast, the diffusion-limited regime showed small nematic bundles of rods together with some randomly packed rods and spheres for $\lambda = 6$ and 11. Additional bulk simulations of sphere-rod mixtures with volume fractions ranging from 0.10 to 0.60 were performed to better comprehend the distribution and alignment of colloids.[151] For mixtures containing $\lambda = 4$ and 6 rods, the system always remained mixed. For the largest aspect ratio ($\lambda = 11$), however, phase separation started at $\phi = 0.40$. At $\phi = 0.50$, the mixture was demixed and the rods were nematically aligned. The global nematic ordering of rods in the bulk simulations was almost completely suppressed in the presence of spheres for $\lambda = 4$ and 6.[151]

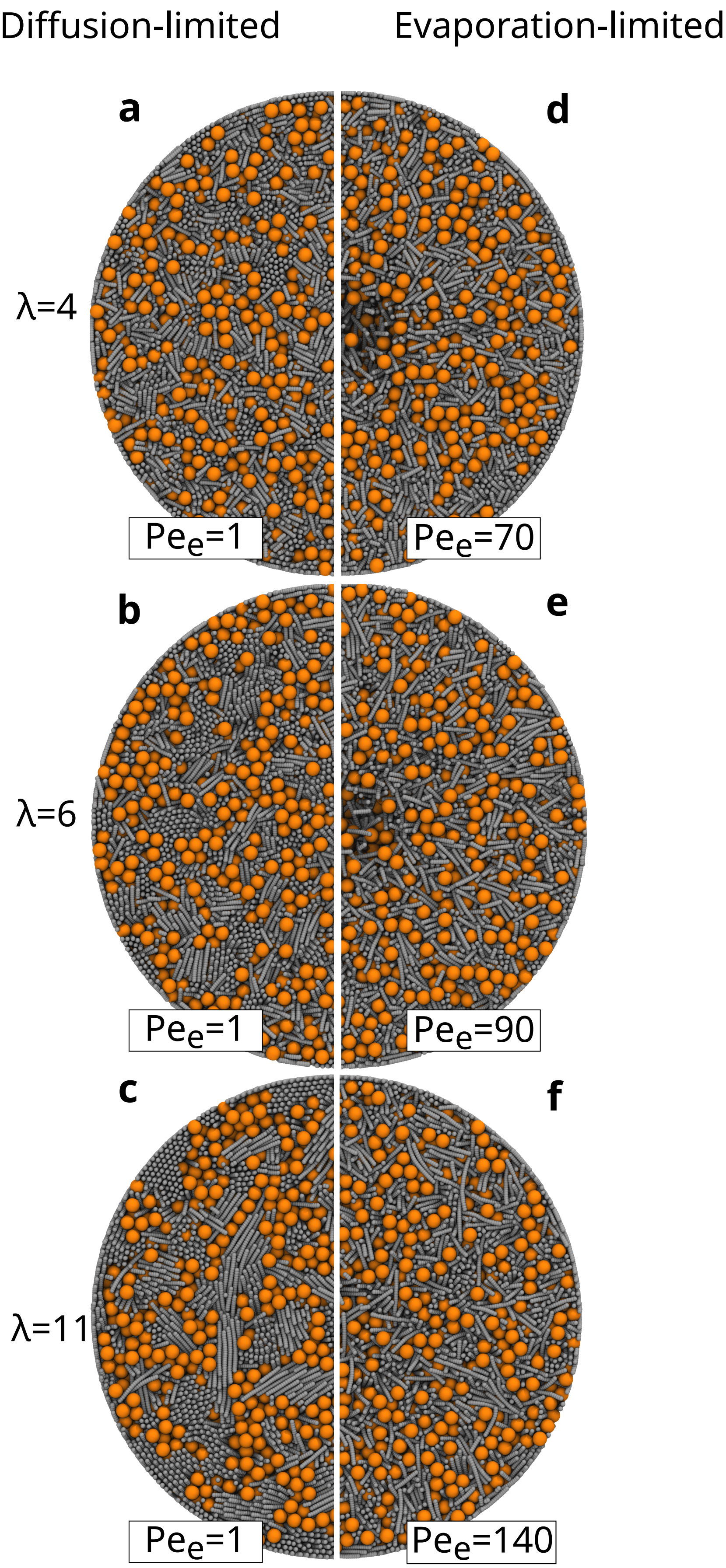

Figure 5.4: The cross-section simulation snapshots of (a-c) diffusion-limited ($Pe \leq 1$) and (d-f) evaporation-limited ($Pe \gg 1$) drying regimes for sphere-rod supraparticles, having λ= 4, 6, and 11 rods (from top to bottom). Reprinted with permission from[151]. Copyright 2024 American Chemical Society.

Drying simulations were used to compute the sphere and rod volume fractions as a function of radial position in the supraparticle from their respective number density profiles.[151] Figure 5.5 shows the volume-fraction profiles at initial, intermediate and final stages of drying for $\lambda = 11$ rods in both Péclet regimes (Pe_e=1 and Pe_e=140). In both cases, supraparticle surfaces were occupied by a thin shell of rods, which was subsequently followed by a sphere dominated region. This segregation behaviour was consistent for all drying speeds as well as when varying rod aspect ratio.[151] This result was different from our experiments, in which fast evaporation rates (low relative humidity experiments) indicated a homogeneous distribution of ellipsoids and spheres on the supraparticle surface. A source of discrepancy between experiments and simulations was related to finite-size effects. In simulations, the ratio between the characteristic size of the supraparticle and the colloidal particles was about 10 for the longest rods, whereas this was close to 150 in the experiments. Another important difference was the interfacial effects that might be present after stabilizing the dispersions with SDS. Such interfacial interactions were not captured by the simulation model and could be changing the surface structure.

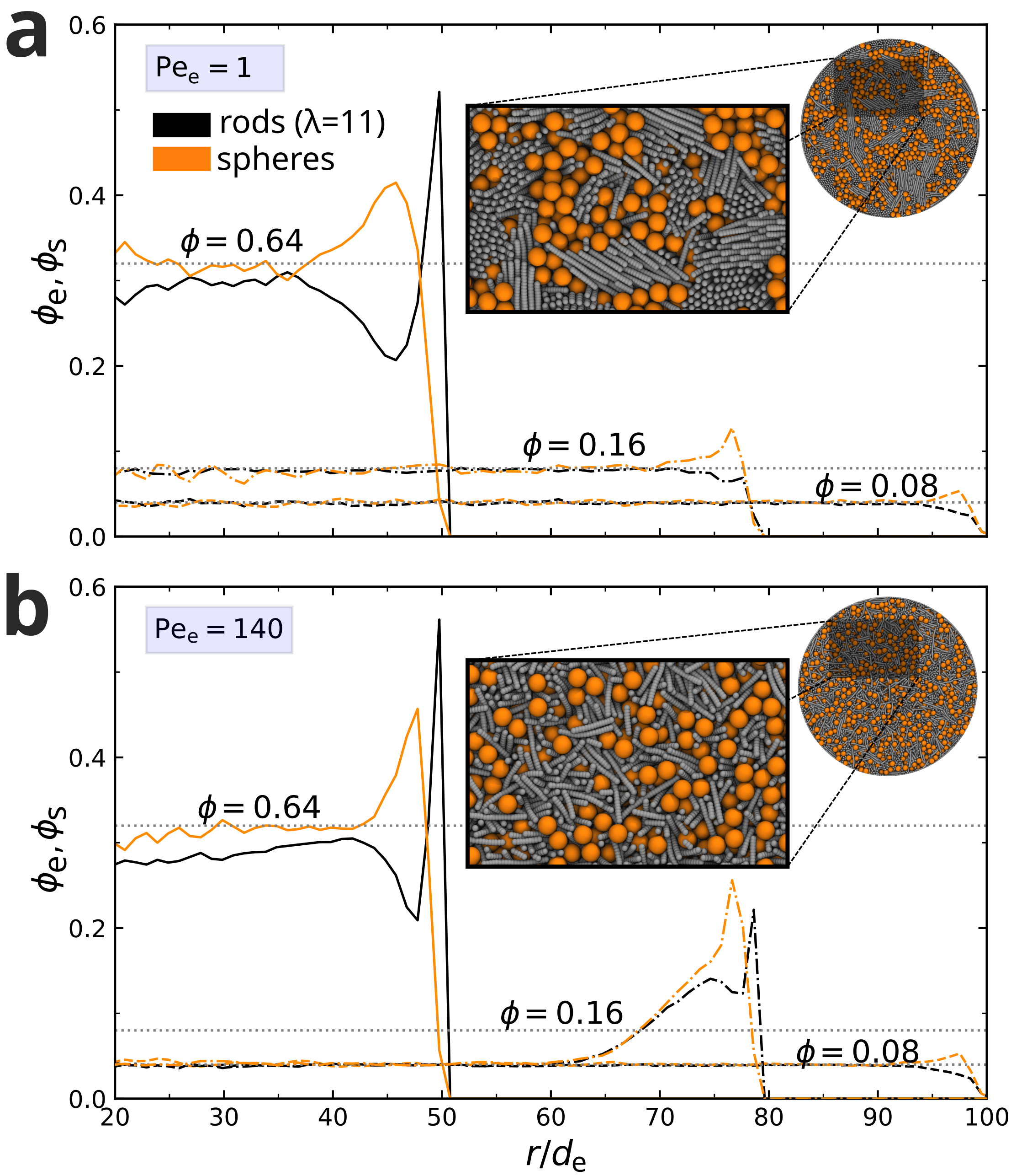

Figure 5.5: Volume fraction profiles computed from drying simulations at a) diffusion-limited regime (Pe_e=1) and b) evaporation-limited regime (Pe_e=140) for mixtures of spheres (ϕ_s, orange) and rods (ϕ_e, black) with λ= 11. The total colloid volume fraction in the droplet (ϕ= 0.08, 0.16, 0.64), corresponding to the computed volume fraction profiles, are shown with dotted gray lines. Insets indicate the cross-section snapshots of supraparticles at ϕ= 0.64. Reprinted with permission from[151]. Copyright 2024 American Chemical Society.

The binary supraparticles (containing λ= 7 ellipsoids) obtained close to diffusion-limited regime with Pe_e=15 and Pe_s=5 (at RH=90%) also exhibited a random distribution of ellipsoids and spheres in the supraparticle interior [Figure 5.6]. No region with aligned ellipsoids or phase separation of ellipsoids and spheres were observed.

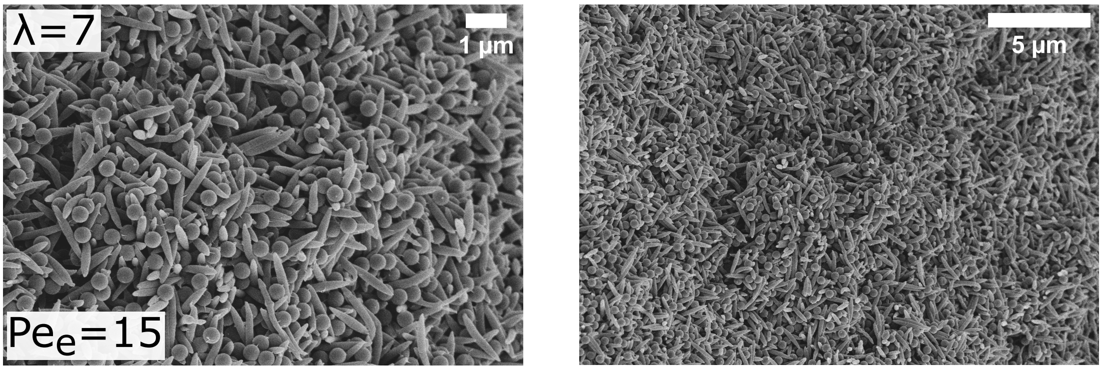

Figure 5.6: The cross-section SEM images of binary supraparticles, composed of spheres and λ= 7 ellipsoids. The evaporation experiments were performed at RH=90%, leading to Pe_e=15 and Pe_s=5. Images are obtained by zooming out from the same region of interest from left to right.

5.4 Supraparticles Obtained by Varying Ellipsoid to Sphere Volume Ratio

Volume concentration of the constituent particles is another important parameter to study apart from the particle sizes or evaporation rate. For that reason, I prepared sphere-ellipsoid (λ= 7) binary supraparticles at different volume ratio of the components (v_e:v_s = 0.4, 2.5, 5, and 10) to analyze any changes in ellipsoid ordering with the addition of spheres. While doing so, the evaporation experiments were conducted at the slowest rate (at RH=90%, with Pe_e=15 and Pe_s=5) to be as close to the diffusion-limited Péclet regime as possible.

As before, the SDS-stabilized binary mixtures formed spherical supraparticles in all cases [Figure 5.7(a)]. For v_e:v_s = 0.4, the supraparticle surfaces were mostly occupied by spheres (σ_s=79%) that showed no crystalline regions [Figure 5.7(b)]. The ellipsoids that appeared on the surface were about σ_e=21% and filled in the interstitial spaces. In the case of binary supraparticles having initially v_e:v_s = 2.5, 5, and 10, the surfaces were predominantly occupied by the ellipsoids ($92 \leq \sigma_e \leq 99$ and $1 \leq \sigma_s \leq 8$) [Figure 5.7(c-e)]. It is important to signify here that the orientational ordering of ellipsoids on the surface was reduced in binary supraparticles compared to pure ellipsoid supraparticles. The 2D heat map shown in Figure 5.7(f) was computed for the v_e:v_s = 2.5 case considering the SEM image in Figure 5.7(c). The heat map displayed almost no longitudinal and no lateral ordering of ellipsoids on the supraparticle surface.

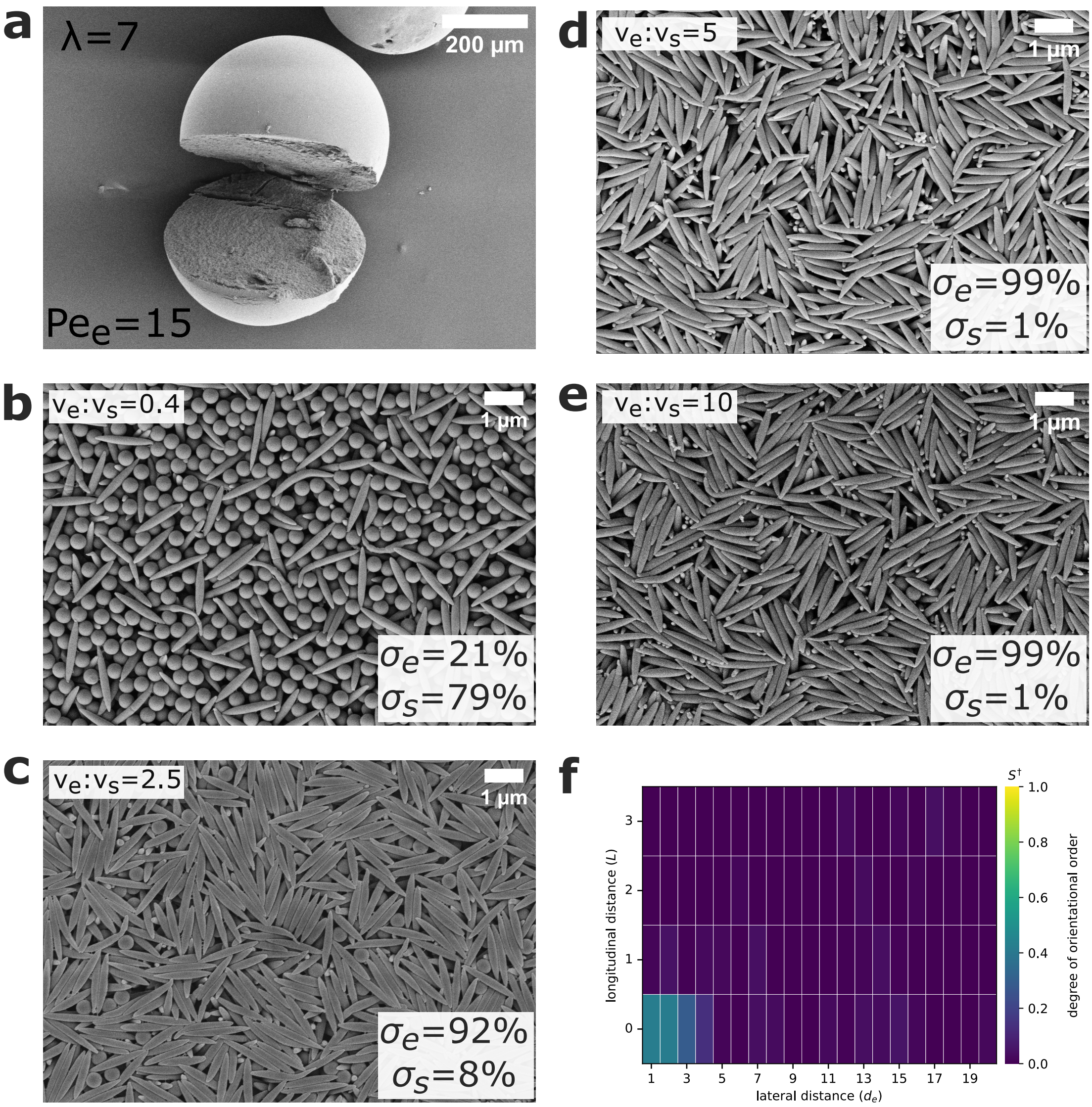

Figure 5.7: SEM images showing a) the final morphology of a binary supraparticle cut in half, and the surface of sphere-ellipsoid (λ= 7) binary supraparticles when v_e:v_s = b) 0.4, c) 2.5, d) 5, e) 10. The relative area fractions σ_e and σ_s are indicated on the images. The supraparticles were prepared at Pe_e=15 and Pe_s=5. f) The 2D heat map for the order parameter $S^\dagger$ was computed from the SEM image of the supraparticle surface shown in c).

Visual inspection of the cross-section SEM images revealed the formation of a thin shell layer of colloids [Figure 5.8], as was observed previously. The local nematic ordering of ellipsoids, which was obtained with pure ellipsoid supraparticles under the same evaporation conditions, was fully suppressed in this case by the presence of spheres. For all volume ratio of the components investigated, ellipsoids and spheres showed a random distribution and did not phase separate in the interior. The hindrance of phase separation might be stemming from the non-equilibrium state of the drying droplet and by the spherical confinement, which would lead to different behavior compared to bulk.[179]

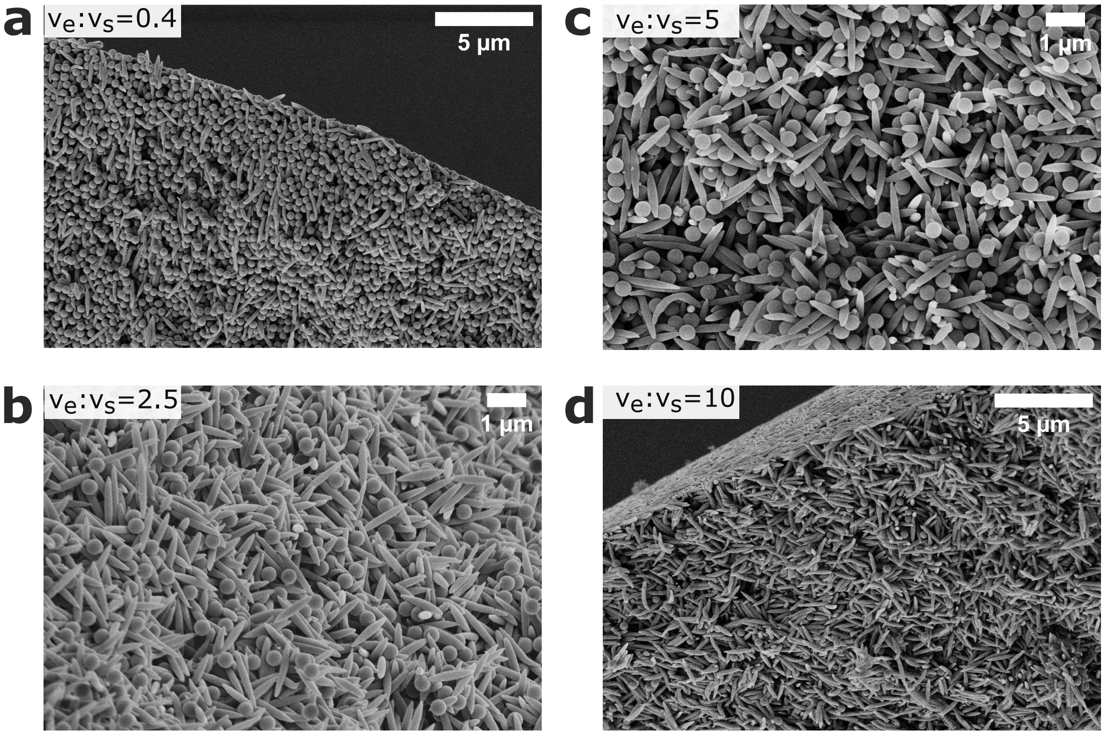

Figure 5.8: The cross-section SEM images of sphere-ellipsoid (λ= 7) supraparticles when v_e:v_s = a) 0.4, b) 2.5, c) 5, d) 10. The supraparticles were prepared at Pe_e=15 and Pe_s=5.

5.5 Conclusions

Chapter 5 showed the formation of sphere-ellipsoid binary supraparticles with a spherical morphology, during which the ellipsoid aspect ratio (λ= 4, 6, 7, and 11), the evaporation rate and the volume ratio of the components varied. The relative area fractions of spheres and ellipsoids on the supraparticle surfaces were altered dramatically by changing the evaporation rate. The binary supraparticle surfaces obtained at higher relative humidity ($15 \leq Pe_e \leq 50$) were composed largely of ellipsoids, whereas those obtained at lower relative humidity ($120 \leq Pe_e \leq 200$) showed an almost even accumulation of both constituents.

The cross-sections of binary supraparticles indicated an ellipsoid-rich surface monolayer ($15 \leq Pe_e \leq 50$). Drying simulations of binary mixtures also exhibited this thin layer of rods at the surface, which was consecutively followed by an additional sphere-rich region. Ellipsoids (rods in case of simulation results) and spheres packed randomly inside the binary supraparticles formed at $15 \leq Pe_e \leq 200$ with the experiments and at $70 \leq Pe_e \leq 140$ with the simulations. The diffusion-limited drying simulations ($Pe \leq 1$) exhibited the formation of small, nematic bundles of rods in the supraparticle interior for $\lambda = 6$ and 11. Furthermore, the experimental binary supraparticles showed an increase in porosity with increasing ellipsoid aspect ratio, as was predicted for random packing of pure ellipsoids.

More binary supraparticles were studied by tuning the ellipsoid to sphere volume ratio (V_e:V_s = 0.4, 2.5, 5, and 10) at Pe_e=15 and Pe_s=5. For the case of V_e:V_s = 0.4, the surfaces were covered mostly with spheres, while for V_e:V_s = 2.5, 5, and 10, the surfaces consisted mostly of ellipsoids. In comparison with pure-ellipsoid supraparticles, the orientational ordering of ellipsoids on the binary supraparticle surfaces decreased in the presence of spheres. The local nematic ordering of ellipsoids in the interior was already disrupted in case of V_e:V_s = 1 (at Pe_e=15). Likewise, the ellipsoids and spheres were randomly distributed in the interiors despite varying the volume ratio of the components. I observed no phase separation of ellipsoids and spheres inside the supraparticles in any case, which was attributed to the non-equilibrium state of the confined droplet.

Chapter 6

Summary and Outlook

During my doctoral studies, I worked on the structure formation in supraparticles composed of ellipsoids and sphere-ellipsoid mixtures under varying ellipsoid aspect ratio and evaporation rates. To focus on studying the physics of supraparticle formation, I used PS colloids to differentiate the effects of particle shape from those of material properties. I fabricated supraparticles by evaporating the respective aqueous dispersion droplets on silicone nanofilaments-based superamphiphobic surfaces. The superamphiphobic surfaces allowed using polymeric and surfactant dispersions as well as monitoring the evaporation process in a slow and controlled manner. The effect of evaporation rate on the structure formation was characterized through the dimensionless Péclet number Pe.

Chapter 3 demonstrated the formation of nonspherical supraparticles independent of the primary colloid shape, initial colloid volume fraction and evaporation rate in case of low colloidal stability. The evaporation videos and confocal imaging showed that the droplets buckled like an elastic shell towards the end of evaporation. Buckling was attributed to the stress-induced deformation of a shell of particles at the droplet surface occurring when the attractive interactions between the particles dominated the stabilizing electrostatic forces. Probing the final supraparticle shape was important, as different applications would require a different shape. For instance, buckled anisotropic supraparticles could be favorable in dynamic flows as self-propelling materials and they can orient in external stimuli (magnetic, electric or shear).[132]

On the other hand, spherical supraparticles might be desired for drug delivery and encapsulation. Therefore, I made further evaporation experiments, which were discussed in Chapter 4, aiming to prevent buckling. This was achieved by adding the surfactant SDS to the dispersion droplets, which increased the stabilizing repulsive interactions between the colloids. The resultant supraparticles were spherical with a smooth surface texture, which facilitated quantifying the range of orientational ordering of ellipsoids. Increasing humidity decreased the evaporation rate leading to Pe_e=10, at which the ellipsoids exhibited an increase of ordering on the supraparticle surface and local nematic ordering in the interior. Complementary drying simulations corroborated the experimental results showing long-range surface ordering and interior local nematic ordering of rods in the diffusion-limited drying regime ($Pe \leq 1$). Both experimental and simulation results indicated that the degree of ordering of elongated particles increased by increasing their aspect ratio. Thus, the orientational ordering of ellipsoids in the experiments can still be improved by increasing the aspect ratio and/or decreasing the evaporation rate. The findings in this study shows the potential to control the degree of ordering of elongated colloids, which is highly desired for various applications such as optics, photonics, and sensing.[194] Such applications can be realized by conducting similar evaporation experiments on superamphiphobic surfaces to create supraparticles using functional elongated colloids, e.g. silica or gold rods.[151]

The final volume fraction of ellipsoids in the supraparticles was calculated for those obtained at $40 \leq Pe_e \leq 70$ by analyzing the evaporation videos. A decreasing tendency in the final volume fraction of the randomly packed ellipsoids was found with increasing aspect ratio. These results indicate that porous supraparticles can be produced by utilizing more elongated ellipsoids, which can then be used in catalysis.[2]

To examine how the ordering and distribution of ellipsoids composing the supraparticles might differ with the addition of spheres, I fabricated binary supraparticles using sphere-ellipsoid mixtures. Chapter 5 showed the spherical final morphology of such binary supraparticles obtained at higher relative humidity ($15 \leq Pe_e \leq 50$) and at lower relative humidity ($120 \leq Pe_e \leq 200$), after stabilizing the dispersions with SDS. The supraparticle surfaces were occupied by ellipsoids in the former, i.e., with slower evaporation, whereas an almost even distribution of constituents were observed in the latter case. The ellipsoid-rich surface monolayer (at $15 \leq Pe_e \leq 50$) indicated by the cross-section SEM images was further confirmed with drying simulations of binary mixtures, which showed a rod-rich surface layer with an additional sphere-rich region underneath. This finding suggests the possibility of creating core-shell supraparticles provided that the ellipsoid aspect ratio and the sphere diameter are adjusted finely.[151]

Binary supraparticles exhibited random distribution of ellipsoids/rods and spheres in the interior at the evaporation-limited regime (at $15 \leq Pe_e \leq 200$ with the experiments and $70 \leq Pe_e \leq 140$ with the simulations). In the diffusion-limited drying simulations ($Pe \leq 1$), $\lambda = 6$ and 11 rods showed small nematic bundles inside the supraparticle. The randomly packed binary supraparticles displayed an increase in porosity with increasing ellipsoid aspect ratio. A way to further increase the porosity of these supraparticles could be by subsequently sacrificing the constituent spheres by calcination, as previously shown for bidisperse sphere mixtures.[2;195]

The presence of spheres in the binary supraparticles decreased the orientational ordering of ellipsoids on the surface as well as in the interior, when compared to pure-ellipsoid supraparticles. Despite varying the ellipsoid to sphere volume ratio (V_e:V_s = 0.4, 2.5, 5, and 10) in the binary mixtures, there was no phase separation between spheres and ellipsoids, which remained randomly distributed inside the supraparticles. Phase separation of the components during supraparticle formation can be attained by fine-tuning the degree of spherical confinement, the initial colloidal volume fractions and the size of the colloids. The phase separation behavior is important to study, as it can be utilized for producing multicomponent supraparticles, such as core-shell and Janus.

The presented work in this thesis is a fundamental study that emphasizes the significance of several parameters on the structure formation of superparticulate matter. One of these parameters is shape, i.e., the aspect ratio of ellipsoids, which changes the orientational ordering and supraparticle porosity. Another important parameter is the interparticle interactions, which directly influence the final supraparticle morphology. The addition of spheres, for instance, has proven to be another way to alter the ordering of ellipsoids within the supraparticle. Finally, the evaporation rate has a dramatic effect on buckling, the ordering of elongated colloids, and particle distribution in case of binary supraparticles. All of such aspects should be taken into consideration when designing supraparticles from anisotropic colloids, as they alter the morphology and ordering which in turn define the functionality of the assembled structure. I hope the key findings in this study inspires the utilization of ellipsoidal particles into highly defined supraparticles to be used in several research areas in the future.

Acknowledgements

[redacted]

[redacted]

[redacted]

[redacted]

[redacted]

[redacted]

Bibliography

[1] Susanne Wintzheimer, Tim Granath, Maximilian Oppmann, Thomas Kister, Thibaut Thai, Tobias Kraus, Nicolas Vogel, and Karl Mandel. Supraparticles: Functionality from uniform structural motifs. *ACS Nano*, 12(6):5093–5120, 2018.

[2] Wendong Liu, Michael Kappl, and Hans-Jürgen Butt. Tuning the porosity of supraparticles. *ACS Nano*, 13(12):13949–13956, 2019.

[3] Bruno D. Mattos, Luiz G. Greca, Blaise L. Tardy, Washington L. E. Magalhães, and Orlando J. Rojas. Green formation of robust supraparticles for cargo protection and hazards control in natural environments. *Small*, 14(29):1801256, 2018.

[4] Wendong Liu, Michael Kappl, Werner Steffen, and Hans-Jürgen Butt. Controlling supraparticle shape and structure by tuning colloidal interactions. *Journal of Colloid and Interface Science*, 607:1661–1670, 2022.

[5] Nicolas Vogel, Markus Retsch, Charles-André Fustin, Aranzazu del Campo, and Ulrich Jonas. Advances in colloidal assembly: The design of structure and hierarchy in two and three dimensions. *Chemical Reviews*, 115(13):6265–6311, 2015.

[6] Sharon Glotzer and Michael Solomon. Anisotropy of building blocks and their assembly into complex structures. *Nature materials*, 6:557–62, 2007.

[7] Stijn Coertjens, Raf De Dier, Paula Moldenaers, Lucio Isa, and Jan Vermant. Adsorption of ellipsoidal particles at liquid–liquid interfaces. *Langmuir*, 33(11):2689–2697, 2017.

[8] Thriveni G. Anjali and Madivala G. Basavaraj. Shape-anisotropic colloids at interfaces. *Langmuir*, 35(1):3–20, 2019.

[9] Hans-Jürgen Butt, Karlheinz Graf, and Michael Kappl. *Introduction*, chapter 1, pages 1–3. John Wiley Sons, Ltd, 2003.

[10] Vinothan N. Manoharan. Colloidal matter: Packing, geometry, and entropy. *Science*, 349:1253751, 2015.

[11] Valerie Anderson and Henk Lekkerkerker. Insights into phase transition kinetics from colloid science. *Nature*, 416:811–5, 2002.

[12] Wilson Poon. Colloids as big atoms. *Science*, 304(5672):830–831, 2004.

[13] Hans-Jürge Butt and Michael Kappl. *Electrostatic Double-Layer Forces*, chapter 4, pages 93–125. John Wiley Sons, Ltd, 2010.

[14] Marek Grzelczak, Jan Vermant, Eric M. Furst, and Luis M. Liz-Marzán. Directed self-assembly of nanoparticles. *ACS Nano*, 4(7):3591–3605, 2010.

[15] Wendong Liu, Jiarul Midya, Michael Kappl, Hans-Jürgen Butt, and Arash Nikoubashman. Segregation in drying binary colloidal droplets. *ACS Nano*, 13(5):4972–4979, 2019.

[16] Shan Jiang, Antony Van Dyk, Alvin Maurice, James Bohling, David Fasano, and Stan Brownell. Design colloidal particle morphology and self-assembly for coating applications. *Chem. Soc. Rev.*, 46:3792–3807, 2017.

[17] Alexander F Routh. Drying of thin colloidal films. *Reports on Progress in Physics*, 76(4):046603, 2013.

[18] M. Schulz and J. L. Keddie. A critical and quantitative review of the stratification of particles during the drying of colloidal films. *Soft Matter*, 14:6181–6197, 2018.

[19] Robert Deegan, Olgica Bakajin, Todd Dupont, Greb Huber, Sidney Nagel, and Thomas Witten. Capillary flow as the cause of ring stains from dried liquid drops. *Nature*, 389:827–829, 1997.

[20] Khellil Sefiane. Patterns from drying drops. *Advances in colloid and interface science*, 206, 2013.

[21] Robert D. Deegan. Pattern formation in drying drops. *Physical review. E, Statistical physics, plasmas, fluids, and related interdisciplinary topics*, 61(1):475–85, 2000.

[22] Robert D. Deegan, Olgica Bakajin, Todd F. Dupont, Greg Huber, Sidney R. Nagel, and Thomas A. Witten. Contact line deposits in an evaporating drop. *Phys. Rev. E*, 62:756–765, 2000.

[23] Peter Yunker, Tim Still, Matthew Lohr, and A Yodh. Suppression of the coffee-ring effect by shape-dependent capillary interactions. *Nature*, 476:308–11, 2011.

[24] Ronald Larson. Re-shaping the coffee ring. *Angewandte Chemie (International ed. in English)*, 51:2546–8, 2012.

[25] Yanshen Li, Cunjing Lv, Zhaohan Li, David Quéré, and Quanshui Zheng. From coffee rings to coffee eyes. *Soft Matter*, 11:4669–4673, 2015.

[26] Venkateshwar Rao Dugyala and Madivala G. Basavaraj. Evaporation of sessile drops containing colloidal rods: Coffee-ring and order–disorder transition. *The Journal of Physical Chemistry B*, 119(9):3860–3867, 2015.

[27] Venkateshwar Rao Dugyala and Madivala G. Basavaraj. Control over coffee-ring formation in evaporating liquid drops containing ellipsoids. *Langmuir*, 30(29):8680–8686, 2014.

[28] Dong-Ook Kim, Min Pack, Han Hu, Hyoungsoo Kim, and Ying Sun. Deposition of colloidal drops containing ellipsoidal particles: Competition between capillary and hydrodynamic forces. *Langmuir*, 32(45):11899–11906, 2016.

[29] Changdeok Seo, Daeho Jang, Jongjin Chae, and Sehyun Shin. Altering the coffee-ring effect by adding a surfactant-like viscous polymer solution. *Scientific Reports*, 7, 2017.

[30] Liying Cui, Yingfeng Li, Jingxia Wang, Entao Tian, Xingye Zhang, Youzhuan Zhang, Yanlin Song, and Lei Jiang. Fabrication of large-area patterned photonic crystals by ink-jet printing. *J. Mater. Chem.*, 19:5499–5502, 2009.

[31] Tak-Sing Wong, Ting-Hsuan Chen, Xiaoying Shen, and Chih-Ming Ho. Nanochromatography driven by the coffee ring effect. *Analytical Chemistry*, 83(6):1871–1873, 2011.

[32] Berend-Jan de Gans and Ulrich S. Schubert. Inkjet printing of well-defined polymer dots and arrays. *Langmuir*, 20(18):7789–7793, 2004.

[33] Junping Jing, Jason Reed, John Huang, Xinghua Hu, Virginia Clarke, Joanne Edington, Dan Housman, Thomas S. Anantharaman, Edward J. Huff, Bud Mishra, Brett Porter, Alexander Shenker, Estarose Wolfson, Catharina Hiort, Ron Kantor, Christopher Aston, and David C. Schwartz. Automated high resolution optical mapping using arrayed, fluid-fixed dna molecules. *Proceedings of the National Academy of Sciences*, 95(14):8046–8051, 1998.

[34] D.E. Walton and C.J. (Member. Spray dried products—characterization of particle morphology. *Chemical Engineering Research and Design*, 77:21–38, 1999.

[35] Reinhard Vehring, Willard Foss, and David Lechuga. Particle formation in spray drying. *Journal of Aerosol Science*, 38:728–746, 2007.

[36] Maarten A.I. Schutyser, Jimmy Perdana, and Remko M. Boom. Single droplet drying for optimal spray drying of enzymes and probiotics. *Trends in Food Science Technology*, 27(2):73–82, 2012.

[37] Zonglin Chu and Stefan Seeger. Superamphiphobic surfaces. *Chem. Soc. Rev.*, 43:2784–2798, 2014.

[38] Robin H. A. Ras and Abraham. Marmur, editors. *Non-wettable Surfaces: Theory, Preparation, and Applications*. The Royal Society of Chemistry, 2017.

[39] Irving Langmuir. The evaporation of small spheres. *Phys. Rev.*, 12:368–370, 1918.

[40] R.G Picknett and R Bexon. The evaporation of sessile or pendant drops in still air. *Journal of Colloid and Interface Science*, 61(2):336–350, 1977.

[41] Alexander F Routh and William B Zimmerman. Distribution of particles during solvent evaporation from films. *Chemical Engineering Science*, 59(14):2961–2968, 2004.

[42] Joseph L. Keddie. Film formation of latex. *Materials Science and Engineering: R: Reports*, 21(3):101–170, 1997.

[43] Michael A. Boles, Michael Engel, and Dmitri V. Talapin. Self-assembly of colloidal nanocrystals: From intricate structures to functional materials. *Chemical Reviews*, 116(18):11220–11289, 2016.

[44] C. Jeffrey Brinker, Yunfeng Lu, Alan Sellinger, and Hongyou Fan. Evaporation-induced self-assembly: Nanostructures made easy. *Advanced Materials*, 11(7):579–585, 1999.

[45] Sidney Diamond. Microstructure and pore structure of impact-compacted clays. *Clays and Clay Minerals - CLAYS CLAY MINER*, 19:239–249, 1971.

[46] Darren Lawless, Sudhir Kapoor, and Dan Meisel. Bifunctional capping of cds nanoparticles and bridging to tio2. *The Journal of Physical Chemistry*, 99(25):10329–10335, 1995.

[47] O. D. Velev, K. Furusawa, and K. Nagayama. Assembly of latex particles by using emulsion droplets as templates. 1. microstructured hollow spheres. *Langmuir*, 12(10):2374–2384, 1996.

[48] Orlin D. Velev, Kunio Furusawa, and Kuniaki Nagayama. Assembly of latex particles by using emulsion droplets as templates. 2. ball-like and composite aggregates. *Langmuir*, 12:2385–2391, 1996.

[49] O. D. Velev and K. Nagayama. Assembly of latex particles by using emulsion droplets. 3. reverse (water in oil) system. *Langmuir*, 13(6):1856–1859, 1997.

[50] Nicolas Vogel, Stefanie Utech, Grant T. England, Tanya Shirman, Katherine R. Phillips, Natalie Koay, Ian B. Burgess, Mathias Kolle, David A. Weitz, and Joanna Aizenberg. Color from hierarchy: Diverse optical properties of micron-sized spherical colloidal assemblies. *Proceedings of the National Academy of Sciences*, 112(35):10845–10850, 2015.

[51] Rafal Klajn, Kyle J. M. Bishop, and Bartosz A. Grzybowski. Light-controlled self-assembly of reversible and irreversible nanoparticle suprastructures. *Proceedings of the National Academy of Sciences*, 104(25):10305–10309, 2007.

[52] Christian M. Heil, Anvay Patil, Bram Vanthournout, Saranshu Singla, Markus Bleuel, Jing-Jin Song, Ziying Hu, Nathan C. Gianneschi, Matthew D. Shawkey, Sunil K. Sinha, Arthi Jayaraman, and Ali Dhinojwala. Mechanism of structural colors in binary mixtures of nanoparticle-based supraballs. *Science Advances*, 9(21):eadf2859, 2023.

[53] M. P.” Pileni. Supraballs as spherical solid 3d superlattices of hydrophobic nanocrystals dispersed in water: nanoarchitectonics and properties. *Phys. Chem. Chem. Phys.*, 24:14140–14149, 2022.

[54] Esteban Piccinini, Diego Pallarola, Fernando Battaglini, and Omar Azzaroni. Self-limited self-assembly of nanoparticles into supraparticles: towards supramolecular colloidal materials by design. *Molecular Systems Design Engineering*, 1:155–162, 2016.

[55] Rhutesh K. Shah, Jin-Woong Kim, and David A. Weitz. Janus supraparticles by induced phase separation of nanoparticles in droplets. *Advanced Materials*, 21(19):1949–1953, 2009.

[56] Vinothan N. Manoharan. Colloidal spheres confined by liquid droplets: Geometry, physics, and physical chemistry. *Solid State Communications*, 139(11):557–561, 2006.

[57] Tobias Bollhorst, Kurosch Rezwan, and Michael Maas. Colloidal capsules: nano- and microcapsules with colloidal particle shells. *Chem. Soc. Rev.*, 46:2091–2126, 2017.

[58] Siyu Li, Leendert G.J. van der Ven, Rick R.M. Joosten, Heiner Friedrich, Remco Tuinier, and A. Catarina C. Esteves. Assembly of partially covered strawberry supracolloids in dilute and concentrate aqueous dispersions. *Journal of Colloid and Interface Science*, 627:827–837, 2022.

[59] Mohammad-Amin Moradi, E. Deniz Eren, Massimiliano Chiappini, Sebastian Rzadkiewicz, Maurits Goudzwaard, Mark van Rijt, Arthur Keizer, Alexander Routh, Marjolein Dijkstra, G. With, Nico Sommerdijk, Heiner Friedrich, and Joe Patterson. Spontaneous organization of supracolloids into three-dimensional structured materials. *Nature Materials*, 20:1–7, 2021.

[60] Jai Il Park, Trung Dac Nguyen, Gleiciani De Queirós Silveira, Joong Hwan Bahng, Sudhanshu Srivastava, Gongpu Zhao, Kai Sun, Peijun Zhang, Sharon C. Glotzer, and Nicholas A. Kotov. Terminal supraparticle assemblies from similarly charged protein molecules and nanoparticles. *Nature communications*, 5, 2014.

[61] Gaoling Yang, Haizheng Zhong, Ruibin Liu, Yongfang Li, and Bingsuo Zou. In situ aggregation of znse nanoparticles into supraparticles: Shape control and doping effects. *Langmuir*, 29(6):1970–1976, 2013.

[62] Shoushan Yu, Jiaqi Wan, and Kezheng Chen. A facile synthesis of superparamagnetic fe3o4 supraparticles@mil-100(fe) core–shell nanostructures: Preparation, characterization and biocompatibility. *Journal of Colloid and Interface Science*, 461:173–178, 2016.

[63] Ke Hou, Jianyu Han, and Zhiyong Tang. Formation of supraparticles and their application in catalysis. *ACS Materials Letters*, 2(1):95–106, 2020.

[64] Xiang Li, Nikunjkumar Visaveliya, Lars Hafermann, G. Alexander Gross, Andrea Knauer, and J. Michael Köhler. Hierarchically structured particles for micro flow catalysis. *Chemical Engineering Journal*, 326:1058–1065, 2017.

[65] Yuanjin Zhao, Yao Cheng, Luoran Shang, Jie Wang, Zhuoying Xie, and Zhongze Gu. Microfluidic synthesis of barcode particles for multiplex assays. *Small*, 11(2):151–174, 2015.

[66] Jin-Gyu Park, Shin-Hyun Kim, Sofia Magkiriadou, Tae Min Choi, Young-Seok Kim, and Vinothan N. Manoharan. Full-spectrum photonic pigments with non-iridescent structural colors through colloidal assembly. *Angewandte Chemie International Edition*, 53(11):2899–2903, 2014.

[67] Nicolas Vogel, Stefanie Utech, Grant T. England, Tanya Shirman, Katherine R. Phillips, Natalie Koay, Ian B. Burgess, Mathias Kolle, David A. Weitz, and Joanna Aizenberg. Color from hierarchy: Diverse optical properties of micron-sized spherical colloidal assemblies. *Proceedings of the National Academy of Sciences*, 112(35):10845–10850, 2015.

[68] H.-J. Koo, Y.J. Kim, Y.H. Lee, W.I. Lee, K. Kim, and N.-G. Park. Nano-embossed hollow spherical tio2 as bifunctional material for high-efficiency dye-sensitized solar cells. *Advanced Materials*, 20(1):195–199, 2008.

[69] Xiaolin li, Meng Gu, Shenyang Hu, Rhiannon Kennard, Pengfei Yan, Xilin Chen, Chongmin Wang, Michael Sailor, Ji-Guang Zhang, and Jun Liu. Mesoporous silicon sponge as an anti-pulverization structure for high-performance lithium-ion battery anodes. *Nature communications*, 5:4105, 2014.

[70] Vinayak Rastogi, Sonia Melle, Oscar G. Calderón, Antonio A. García, Manuel Marquez, and Orlin D. Velev. Synthesis of light-diffracting assemblies from microspheres and nanoparticles in droplets on a superhydrophobic surface. *Advanced Materials*, 20(22):4263–4268, 2008.

[71] J.H. Moon, G.-R. Yi, S.-M. Yang, D.J. Pine, and S.B. Park. Electrospray-assisted fabrication of uniform photonic balls. *Advanced Materials*, 16(7):605–609, 2004.

[72] Renhua Deng, Lisong Yang, and Colin D. Bain. Combining inkjet printing with emulsion solvent evaporation to pattern polymeric particles. *ACS Applied Materials & Interfaces*, 10(15):12317–12322, 2018.

[73] G.-R. Yi, V.N. Manoharan, S. Klein, K.R. Brzezinska, D.J. Pine, F.F. Lange, and S.-M. Yang. Monodisperse micrometer-scale spherical assemblies of polymer particles. *Advanced Materials*, 14(16):1137–1140, 2002.

[74] C Charcosset, I Limayem, and H Fessi. The membrane emulsification process—a review. *Journal of Chemical Technology & Biotechnology*, 79(3):209–218, 2004.

[75] Andrew Utada, Liang-Yin Chu, Alberto Fernandez-Nieves, Darren Link, C. Holtze, and D. Weitz. Dripping, jetting, drops, and wetting: The magic of microfluidics. *MRS Bulletin*, 32:702–708, 2007.

[76] K. Landfester. Synthesis of colloidal particles in miniemulsions. *Annual Review of Materials Research*, 36(1):231–279, 2006.

[77] Katharina Landfester. Miniemulsion polymerization and the structure of polymer and hybrid nanoparticles. *Angewandte Chemie International Edition*, 48(25):4488–4507, 2009.

[78] Johann Lacava, Ahmed-Amine Ouali, Brice Raillard, and Tobias Kraus. On the behaviour of nanoparticles in oil-in-water emulsions with different surfactants. *Soft Matter*, 10:1696–1704, 2014.

[79] Thomas Kister, Marko Mravlak, Tanja Schilling, and Tobias Kraus. Pressure-controlled formation of crystalline, janus, and core–shell supraparticles. *Nanoscale*, 8:13377–13384, 2016.

[80] Emanuele Marino, Thomas Kodger, Gerard Wegdam, and Peter Schall. Revealing driving forces in quantum dot supercrystal assembly. *Advanced Materials*, 30:1803433, 2018.

[81] Young-Sang Cho, Gi-Ra Yi, Shin-Hyun Kim, David J. Pine, and Seung-Man Yang. Colloidal clusters of microspheres from water-in-oil emulsions. *Chemistry of Materials*, 17(20):5006–5013, 2005.

[82] Orlin D. Velev, Abraham M. Lenhoff, and Eric W. Kaler. A class of microstructured particles through colloidal crystallization. *Science*, 287(5461):2240–2243, 2000.

[83] Vinothan N. Manoharan, Mark T. Elsesser, and David J. Pine. Dense packing and symmetry in small clusters of microspheres. *Science*, 301(5632):483–487, 2003.

[84] Yuchi Yang, Biwei Wang, Xiudi Shen, Luyin Yao, Lei Wang, Xiao Chen, Songhai Xie, Tongtao Li, Jianhua Hu, Dong Yang, and Angang Dong. Scalable assembly of crystalline binary nanocrystal superparticles and their enhanced magnetic and electrochemical properties. *Journal of the American Chemical Society*, 140(44):15038–15047, 2018.

[85] L. L. A. Adams, Thomas E. Kodger, Shin-Hyun Kim, Ho Cheng Shum, Thomas Franke, and David A. Weitz. Single step emulsification for the generation of multi-component double emulsions. *Soft Matter*, 8:10719–10724, 2012.

[86] Teresa Brugarolas, Fuquan Tu, and Daeyeon Lee. Directed assembly of particles using microfluidic droplets and bubbles. *Soft Matter*, 9:9046–9058, 2013.

[87] Ju Hyeon Kim, Tae Yoon Jeon, Tae Min Choi, Tae Soup Shim, Shin-Hyun Kim, and Seung-Man Yang. Droplet microfluidics for producing functional microparticles. *Langmuir*, 30(6):1473–1488, 2014.

[88] Dhananjay Dendukuri and Patrick S. Doyle. The synthesis and assembly of polymeric microparticles using microfluidics. *Advanced Materials*, 21(41):4071–4086, 2009.

[89] Jing-Tao Wang, Juan Wang, and Jun-Jie Han. Fabrication of advanced particles and particle-based materials assisted by droplet-based microfluidics. *Small*, 7(13):1728–1754, 2011.

[90] Shelley L. Anna, Nathalie Bontoux, and Howard A. Stone. Formation of dispersions using “flow focusing” in microchannels. *Applied Physics Letters*, 82:364–366, 2003.

[91] T. Nisisako, T. Torii, T. Takahashi, and Y. Takizawa. Synthesis of monodis-

perse bicolored janus particles with electrical anisotropy using a microfluidic co-flow system. *Advanced Materials*, 18(9):1152–1156, 2006.

[92] Shengqing Xu, Zhihong Nie, Minseok Seo, Patrick Lewis, Eugenia Kumacheva, Howard A. Stone, Piotr Garstecki, Douglas B. Weibel, Irina Gitlin, and George M. Whitesides. Generation of monodisperse particles by using microfluidics: Control over size, shape, and composition. *Angewandte Chemie International Edition*, 44(5):724–728, 2005.

[93] E. Amstad, M. Chemama, M. Eggersdorfer, L. R. Arriaga, M. P. Brenner, and D. A. Weitz. Robust scalable high throughput production of monodisperse drops. *Lab Chip*, 16:4163–4172, 2016.

[94] N. Tsapis, E. R. Dufresne, S. S. Sinha, C. S. Riera, J. W. Hutchinson, L. Mahadevan, and D. A. Weitz. Onset of buckling in drying droplets of colloidal suspensions. *Phys. Rev. Lett.*, 94:018302, 2005.

[95] É. Lintingre, G. Ducouret, F. Lequeux, L. Olanier, T. Périé, and L. Talini. Controlling the buckling instability of drying droplets of suspensions through colloidal interactions. *Soft Matter*, 11:3660–3665, 2015.

[96] Zhe Liu, Yong Liu, Jinge Yang, Shengsong Li, Chaoyi Peng, Xin Cui, Liping Sheng, and Binrui Wu. Highly efficient and controlled fabrication of supraparticles by leidenfrost phenomenon. *Langmuir*, 38(30):9157–9165, 2022.

[97] David Quéré. Leidenfrost dynamics. *Annual Review of Fluid Mechanics*, 45:197–215, 2013.

[98] Ranajt Mondal, Avik Das, Debasis Sen, Dillip K. Satapathy, and Madivala G. Basavaraj. Spray drying of colloidal dispersions containing ellipsoids. *Journal of Colloid and Interface Science*, 551:242–250, 2019.

[99] Asep Bayu Dani Nandiyanto and Kikuo Okuyama. Progress in developing spray-drying methods for the production of controlled morphology particles: From the nanometer to submicrometer size ranges. *Advanced Powder Technology*, 22(1):1–19, 2011.

[100] Thomas Ballweg, Carsten Gellermann, and Karl Mandel. Coatings with a mole-hill structure of nanoparticle-raspberry containers for surfaces with abrasion-refreshable reservoir functionality. *ACS Applied Materials & Interfaces*, 7(44):24909–24914, 2015.

[101] Avik Das, D. Sen, S. Mazumder, A. K. Ghosh, C. B. Basak, and K. Dasgupta. Formation of nano-structured core–shell micro-granules by evaporation induced assembly. *RSC Adv.*, 5:85052–85060, 2015.

[102] Sarah Wenderoth, Tim Granath, Johannes Prieschl, Susanne Wintzheimer, and Karl Mandel. Abrasion indicators for smart surfaces based on a luminescence turn-on effect in supraparticles. *Advanced Photonics Research*, 1(1):2000023, 2020.

[103] Thomas Young. Iii. an essay on the cohesion of fluids. *Philosophical Transactions of the Royal Society of London*, 95:65 – 87, 1805.

[104] Hans-Jürgen Butt, Karlheinz Graf, and Michael Kappl. *Contact Angle Phenomena and Wetting*, chapter 7, pages 118–144. John Wiley Sons, Ltd, 2003.

[105] Arun K. Kota, Wonjae Choi, and Anish Tuteja. Superomniphobic surfaces: Design and durability. *MRS Bulletin*, 38(5):383–390, 2013.

[106] Robert N. Wenzel. Resistance of solid surfaces to wetting by water. *Industrial & Engineering Chemistry*, 28:988–994, 1936.

[107] A. B. D. Cassie and S. Baxter. Wettability of porous surfaces. *Trans. Faraday Soc.*, 40:546–551, 1944.

[108] Arun Kota, Gibum Kwon, and Anish Tuteja. The design and applications of superomniphobic surfaces. *NPG Asia Materials*, 6:e109, 2014.

[109] Anish Tuteja, Wonjae Choi, Minglin Ma, Joseph Mabry, Sarah Mazzella, Gregory Rutledge, Gareth McKinley, and Robert Cohen. Designing superoleophobic surfaces. *Science (New York, N.Y.)*, 318:1618–22, 2008.

[110] Kerstin Koch, Holger Florian Bohn, and Wilhelm Barthlott. Hierarchically sculptured plant surfaces and superhydrophobicity. *Langmuir*, 25(24):14116–14120, 2009.

[111] Bharat Bhushan and Yong Chae Jung. Natural and biomimetic artificial surfaces for superhydrophobicity, self-cleaning, low adhesion, and drag reduction. *Progress in Materials Science*, 56(1):1–108, 2011.

[112] Jiann Shieh, Fu Ju Hou, Yan Chen Chen, Hung Min Chen, Shun Po Yang, Chao Chia Cheng, and Hsuen Li Chen. Robust airlike superhydrophobic surfaces. *Advanced Materials*, 22(5):597–601, 2010.

[113] Changdong Gu, Hang Ren, Jiangping Tu, and Tong-Yi Zhang. Micro/nanobinary structure of silver films on copper alloys with stable water-repellent property under dynamic conditions. *Langmuir*, 25(20):12299–12307, 2009.

[114] Ralf Helbig, Julia Nickerl, Christoph Neinhuis, and Carsten Werner. Smart skin patterns protect springtails. *PloS one*, 6(9):e25105, 2011.

[115] Junping Zhang and Stefan Seeger. Superoleophobic coatings with ultralow sliding angles based on silicone nanofilaments. *Angewandte Chemie International Edition*, 50(29):6652–6656, 2011.

[116] Hans-Jürgen Butt, Ciro Semprebon, Periklis Papadopoulos, Doris Vollmer, Martin Brinkmann, and Matteo Ciccotti. Design principles for superamphiphobic surfaces. *Soft Matter*, 9:418–428, 2013.

[117] Hannu Teisala and Hans-Jürgen Butt. Hierarchical structures for superhydrophobic and superoleophobic surfaces. *Langmuir*, 35(33):10689–10703, 2019.

[118] Takashi Fujii, Yoshitaka Aoki, and Hiroki Habazaki. Fabrication of super-oil-repellent dual pillar surfaces with optimized pillar intervals. *Langmuir*, 27(19):11752–11756, 2011.

[119] Kevin Golovin, Duck H. Lee, Joseph M. Mabry, and Anish Tuteja. Transparent, flexible, superomniphobic surfaces with ultra-low contact angle hysteresis. *Angewandte Chemie International Edition*, 52(49):13007–13011, 2013.

[120] Xu Deng, Lena Mammen, Hans-Jürgen Butt, and Doris Vollmer. Candle soot as a template for a transparent robust superamphiphobic coating. *Science*, 335(6064):67–70, 2012.

[121] K. Zhao, K.S. Liu, J.F. Li, W.H. Wang, and L. Jiang. Superamphiphobic cali-based bulk metallic glasses. *Scripta Materialia*, 60(4):225–227, 2009.

[122] Shuaijun Pan, Arun K. Kota, Joseph M. Mabry, and Anish Tuteja. Superomniphobic surfaces for effective chemical shielding. *Journal of the American Chemical Society*, 135(2):578–581, 2013.

[123] Vinayak Rastogi, Antonio A. García, Manuel Marquez, and Orlin D. Velev. Anisotropic particle synthesis inside droplet templates on superhydrophobic surfaces. *Macromolecular Rapid Communications*, 31(2):190–195, 2010.

[124] Carola Seyfert, Erwin J. W. Berenschot, Niels R. Tas, Arturo Susarrey-Arce, and Alvaro Marin. Evaporation-driven colloidal cluster assembly using droplets on superhydrophobic fractal-like structures. *Soft Matter*, 17:506–515, 2021.

[125] Jinming Zhou, Jing Yang, Zhandong Gu, Guofu Zhang, Yu Wei, Xi Yao, Yanlin Song, and Lei Jiang. Controllable fabrication of noniridescent microshaped photonic crystal assemblies by dynamic three-phase contact line behaviors on superhydrophobic substrates. *ACS Applied Materials & Interfaces*, 7(40):22644–22651, 2015.

[126] Sanghyuk Wooh, Hannah Huesmann, Muhammad Nawaz Tahir, Maxime Paven, Kristina Wichmann, Doris Vollmer, Wolfgang Tremel, Periklis Papadopoulos, and Hans-Jürgen Butt. Synthesis of mesoporous supraparticles on superamphiphobic surfaces. *Advanced Materials*, 27(45):7338–7343, 2015.

[127] Huanshu Tan, Christian Diddens, Michel Versluis, Hans-Jürgen Butt, Detlef Lohse, and Xuehua Zhang. Self-wrapping of an ouzo drop induced by evaporation on a superamphiphobic surface. *Soft Matter*, 13:2749–2759, 2017.

[128] M.I. Rial-Hermida, N.M. Oliveira, A. Concheiro, C. Alvarez-Lorenzo, and J.F. Mano. Bioinspired superamphiphobic surfaces as a tool for polymer- and solvent-independent preparation of drug-loaded spherical particles. *Acta Biomaterialia*, 10(10):4314–4322, 2014.

[129] H. Tan, Sanghyuk Wooh, Hans-Jürgen Butt, Xuehua Zhang, and D. Lohse. Porous supraparticle assembly through self-lubricating evaporating colloidal ouzo drops. *Nature Communications*, 10(478):1–8, 2019.

[130] Takafumi Sekido, Sanghyuk Wooh, Regina Fuchs, Michael Kappl, Yoshinobu Nakamura, Hans-Jürgen Butt, and Syuji Fujii. Controlling the structure of supraballs by ph-responsive particle assembly. *Langmuir*, 33(8):1995–2002, 2017.

[131] Atsushi Fujiwara, Junwei Wang, Shotaro Hiraide, Alexander Götz, Minoru T. Miyahara, Martin Hartmann, Benjamin Apeleo Zubiri, Erdmann Spiecker, Nicolas Vogel, and Satoshi Watanabe. Fast gas-adsorption kinetics in supraparticle-based mof packings with hierarchical porosity. *Advanced Materials*, 35(44):2305980, 2023.

[132] Marcel Sperling, Orlin D. Velev, and Michael Gradzielski. Controlling the shape of evaporating droplets by ionic strength: Formation of highly anisometric silica supraparticles. *Angewandte Chemie International Edition*, 53(2):586–590, 2014.

[133] Lijun T. Raju, Shubhankar Chakraborty, Binita Pathak, and Saptarshi Basu. Controlling self-assembly and topology at micro–nano length scales using a contact-free mixed nanocolloid droplet architecture. *Langmuir*, 34(18):5323–5333, 2018.

[134] Anvay Patil, Christian M. Heil, Bram Vanthournout, Markus Bleuel, Saranshu Singla, Ziying Hu, Nathan C. Gianneschi, Matthew D. Shawkey,

Sunil K. Sinha, Arthi Jayaraman, and Ali Dhinojwala. Structural color production in melanin-based disordered colloidal nanoparticle assemblies in spherical confinement. *Advanced Optical Materials*, 10(5):2102162, 2022.

[135] Minghan Hu, Hans-Jürgen Butt, Katharina Landfester, Markus B. Bannwarth, Sanghyuk Wooh, and Héloïse Thérien-Aubin. Shaping the assembly of superparamagnetic nanoparticles. *ACS Nano*, 13(3):3015–3022, 2019.

[136] Nicolas Pazos-Perez, Claudia Simone Wagner, Jose M. Romo-Herrera, Luis M. Liz-Marzán, F Javier GarcíadeAbajo, Alexander Wittemann, Andreas Fery, and Ramón A. Alvarez-Puebla. Organized plasmonic clusters with high coordination number and extraordinary enhancement in surface-enhanced raman scattering (sers). *Angewandte Chemie International Edition*, 51(51):12688–12693, 2012.

[137] Sarah Schyck, Janne-Mieke Meijer, Lucia Baldauf, Peter Schall, Andrei V. Petukhov, and Laura Rossi. Self-assembly of colloidal superballs under spherical confinement of a drying droplet. *JCIS Open*, 5:100037, 2022.

[138] Liang Wu, Alexandr Malijevský, Carlos Avendaño, Erich A. Müller, and George Jackson. Demixing, surface nematization, and competing adsorption in binary mixtures of hard rods and hard spheres under confinement. *The Journal of Chemical Physics*, 148(16):164701, 2018.

[139] Sabyasachi Dasgupta, Marina Katava, Mohammed Faraj, Thorsten Auth, and Gerhard Gompper. Capillary assembly of microscale ellipsoidal, cuboidal, and spherical particles at interfaces. *Langmuir*, 30(40):11873–11882, 2014.

[140] M. G. Basavaraj, G. G. Fuller, J. Fransaer, and J. Vermant. Packing, flipping, and buckling transitions in compressed monolayers of ellipsoidal latex particles. *Langmuir*, 22(15):6605–6612, 2006.

[141] Gianni Jacucci, Brooke W. Longbottom, Christopher C. Parkins, Stefan A. F. Bon, and Silvia Vignolini. Anisotropic silica colloids for light scattering. *J. Mater. Chem. C*, 9:2695–2700, 2021.

[142] Eduardo Basurto, Péter Gurin, Szabolcs Varga, and Gerardo Odriozola. Ordering, clustering, and wetting of hard rods in extreme confinement. *Phys. Rev. Res.*, 2:013356, 2020.

[143] Da Wang, Michiel Hermes, Rama Kotni, Yaoting Wu, Nikos Tasios, Yang Liu, Bart de Nijs, Ernest Wee, Christopher Murray, Marjolein Dijkstra, and Alfons van Blaaderen. Interplay between spherical confinement and particle shape on the self-assembly of rounded cubes. *Nature Communications*, 9:2228, 2018.

[144] Xiaomei Yao and Jeff Z. Y. Chen. Rodlike molecules in extreme confinement. *Phys. Rev. E*, 101:062706, 2020.

[145] Jessi E.S. van der Hoeven, Harith Gurunarayanan, Maarten Bransen, D.A. Matthijs de Winter, Petra E. de Jongh, and Alfons van Blaaderen. Silica-coated gold nanorod supraparticles: A tunable platform for surface enhanced raman spectroscopy. *Advanced Functional Materials*, 32(27):2200148, 2022.

[146] Da Wang, Michiel Hermes, Stan Najmr, Nikos Tasios, Albert Grau-Carbonell, Yang Liu, Sara Bals, Marjolein Dijkstra, Christopher Murray, and Alfons Blaaderen. Structural diversity in three-dimensional self-assembly of nanoplatelets by spherical confinement. *Nature Communications*, 13(6001):1–12, 2022.

[147] Xiao-Liang Fang, Cheng Chen, Ming-Shang Jin, Qin Kuang, Zhao-Xiong Xie, Su-Yuan Xie, Rong-Bin Huang, and Lan-Sun Zheng. Single-crystal-like hematite colloidal nanocrystal clusters: synthesis and applications in gas sensors, photocatalysis and water treatment. *J. Mater. Chem.*, 19:6154–6160, 2009.

[148] Henriëtte E. Bakker, Simone Dussi, Barbera L. Droste, Thijs H. Besseling, Chris L. Kennedy, Evert I. Wiegant, Bing Liu, Arnout Imhof, Marjolein Dijkstra, and Alfons van Blaaderen. Phase diagram of binary colloidal rod-sphere mixtures from a 3d real-space analysis of sedimentation–diffusion equilibria. *Soft Matter*, 12:9238–9245, 2016.

[149] Thomas E. Gartner, Christian M. Heil, and Arthi Jayaraman. Surface composition and ordering of binary nanoparticle mixtures in spherical confinement. *Mol. Syst. Des. Eng.*, 5:864–875, 2020.

[150] Yunfeng Li, Jeffrey Jun-Yan Suen, Elisabeth Prince, Egor M. Larin, Anna Klinkova, Héloïse Thérien-Aubin, Shoujun Zhu, Bai Yang, Amr S. Helmy, Oleg D. Lavrentovich, and Eugenia Kumacheva. Colloidal cholesteric liquid crystal in spherical confinement. *Nature Communications*, 7(12520):1–11, 2016.

[151] Melis Yetkin, Yashraj M. Wani, Kritika Kritika, Michael P. Howard, Michael Kappl, Hans-Jürgen Butt, and Arash Nikoubashman. Structure formation in supraparticles composed of spherical and elongated particles. *Langmuir*, 40(1):1096–1108, 2024.

[152] C.C. Ho, Andrew Keller, Jeffrey A. Odell, and Ronald Harry Ottewill. Preparation of monodisperse ellipsoidal polystyrene particles. *Colloid and Polymer Science*, 271:469–479, 1993.

[153] Grant T.D. Shouldice, Gerald A. Vandezande, and Alfred Rudin. Practical aspects of the emulsifier-free emulsion polymerization of styrene. *European Polymer Journal*, 30(2):179–183, 1994.

[154] Florian Geyer, Clarissa Schönecker, Hans-Jürgen Butt, and Doris Vollmer. Enhancing co2 capture using robust superomniphobic membranes. *Advanced Materials*, 29(5):1603524, 2017.

[155] K.M Keville, E.I Franses, and J.M Caruthers. Preparation and characterization of monodisperse polymer microspheroids. *Journal of Colloid and Interface Science*, 144(1):103–126, 1991.

[156] Hans-Jürgen Butt, Karlheinz Graf, and Michael Kappl. *Solid Surfaces*, chapter 8, pages 145–176. John Wiley Sons, Ltd, 2003.

[157] H. Anton and A. Herr. *Calculus with Analytic Geometry*. Wiley, 1995.

[158] L. Pauchard and C. Allain. Buckling instability induced by polymer solution drying. *Europhysics Letters*, 62(6):897, 2003.

[159] Binita Pathak and Saptarshi Basu. Phenomenology and control of buckling dynamics in multicomponent colloidal droplets. *Journal of Applied Physics*, 117(24):244901, 2015.

[160] J. Bahadur, D. Sen, S. Mazumder, B. Paul, H. Bhatt, and S. G. Singh. Control of buckling in colloidal droplets during evaporation-induced assembly of nanoparticles. *Langmuir*, 28(3):1914–1923, 2012.

[161] J. Bahadur, D. Sen, S. Mazumder, S. Bhattacharya, H. Frielinghaus, and G. Goerigk. Origin of buckling phenomenon during drying of micrometer-sized colloidal droplets. *Langmuir*, 27(13):8404–8414, 2011.

[162] Ahmed Al Harraq and Bhuvnesh Bharti. Increasing aspect ratio of particles suppresses buckling in shells formed by drying suspensions. *Soft Matter*, 16:9643–9647, 2020.

[163] R. Vasanthi, Sarika Bhattacharyya, and Biman Bagchi. Anisotropic diffusion of spheroids in liquids: Slow orientational relaxation of the oblates. *The Journal of Chemical Physics*, 116(3):1092–1096, 2002.

[164] Marcel Sperling, Periklis Papadopoulos, and Michael Gradzielski. Understanding the formation of anisometric supraparticles: A mechanistic look inside droplets drying on a superhydrophobic surface. *Langmuir*, 32(27):6902–6908, 2016.

[165] Mahesh S. Tirumkudulu. Buckling of a drying colloidal drop. *Soft Matter*, 14:7455–7461, 2018.

[166] Basavaraj Madivala, Jan Fransaer, and Jan Vermant. Self-assembly and rheology of ellipsoidal particles at interfaces. *Langmuir*, 25(5):2718–2728, 2009.

[167] J. C. Loudet, A. G. Yodh, and B. Pouligny. Wetting and contact lines of micrometer-sized ellipsoids. *Phys. Rev. Lett.*, 97:018304, 2006.

[168] H. Lehle, E. Noruzifar, and M. Oettel. Ellipsoidal particles at fluid interfaces. *The European Physical Journal E*, 26(1–2):151–160, 2008.

[169] F Bresme and M Oettel. Nanoparticles at fluid interfaces. *Journal of Physics: Condensed Matter*, 19(41):413101, 2007.

[170] Priyanka Biswas, D. Sen, S. Mazumder, C. B. Basak, and P. Doshi. Temperature mediated morphological transition during drying of spray colloidal droplets. *Langmuir*, 32(10):2464–2473, 2016.

[171] D. Sen, S. Mazumder, J. S. Melo, Arshad Khan, S. Bhattyacharya, and S. F. D'Souza. Evaporation driven self-assembly of a colloidal dispersion during spray drying: Volume fraction dependent morphological transition. *Langmuir*, 25(12):6690–6695, 2009.

[172] R. Porcel, A.B. Jódar, M.A. Cabrerizo, R. Hidalgo-Álvarez, and A. Martín-Rodríguez. Sequential adsorption of triton x-100 and sodium dodecyl sulfate onto positively and negatively charged polystyrene latexes. *Journal of Colloid and Interface Science*, 239(2):568–576, 2001.

[173] Hans-Jürgen Butt, Karlheinz Graf, and Michael Kappl. *Surfactants, Micelles, Emulsions, and Foams*, chapter 12, pages 118–144. John Wiley Sons, Ltd, 2003.

[174] Wojciech Kwieciński, Tim Segers, Sjoerd van der Werf, Arie van Houselt, Detlef Lohse, Harold J. W. Zandvliet, and Stefan Kooij. Evaporation of dilute sodium dodecyl sulfate droplets on a hydrophobic substrate. *Langmuir*, 35(32):10453–10460, 2019.

[175] Ana Dominguez, Aurora Fernandez, Noemi Gonzalez, Emilia Iglesias, and Luis Montenegro. Determination of critical micelle concentration of some surfactants by three techniques. *Journal of Chemical Education*, 74(10):1227, 1997.

[176] Ana B. Jódar-Reyes, Antonio Martín-Rodríguez, and Juan L. Ortega-Vinuesa. Effect of the ionic surfactant concentration on the stabilization/destabilization of polystyrene colloidal particles. *Journal of Colloid and Interface Science*, 298(1):248–257, 2006.

[177] Yu Tang, Biying Du, Jun Yang, and Yuanming Zhang. Temperature effects on surface activity and application in oxidation of toluene derivatives of ctab-sds with kmno4. *Journal of Chemical Sciences*, 118(3):281–285, 2006.

[178] Jörg Roller, John David Geiger, Markus Voggenreiter, Janne-Mieke Meijer, and Andreas Zumbusch. Formation of nematic order in 3d systems of hard colloidal ellipsoids. *Soft Matter*, 16:1021–1028, 2020.

[179] Arash Nikoubashman. Ordering, phase behavior, and correlations of semiflexible polymers in confinement. *The Journal of Chemical Physics*, 154(9):090901, 2021.

[180] Lars Onsager. The effects of shape on the interaction of colloidal particles. *Annals of the New York Academy of Sciences*, 51(4):627–659, 1949.

[181] Alejandro Cuetos and Marjolein Dijkstra. Kinetic pathways for the isotropic-nematic phase transition in a system of colloidal hard rods: A simulation study. *Phys. Rev. Lett.*, 98:095701, 2007.

[182] A. Gschwind, M. Klopotek, Y. Ai, and M. Oettel. Isotropic-nematic transition for hard rods on a three-dimensional cubic lattice. *Phys. Rev. E*, 96:012104, 2017.

[183] Albert P. Philipse. The random contact equation and its implications for (colloidal) rods in packings, suspensions, and anisotropic powders. *Langmuir*, 12(5):1127–1133, 1996.

[184] S. R. Williams and A. P. Philipse. Random packings of spheres and spherocylinders simulated by mechanical contraction. *Phys. Rev. E*, 67:051301, 2003.

[185] Claudia Ferreiro-Córdova and Jeroen S. van Duijneveldt. Random packing of hard spherocylinders. *Journal of Chemical & Engineering Data*, 59(10):3055–3060, 2014.

[186] Alan Wouterse, Stephen R Williams, and Albert P Philipse. Effect of particle shape on the density and microstructure of random packings. *Journal of Physics: Condensed Matter*, 19(40):406215, 2007.

[187] Jian Zhao, Shuixiang Li, Ruiping Zou, and Aibing Yu. Dense random packings of spherocylinders. *Soft Matter*, 8:1003–1009, 2012.

[188] Andriy V. Kyrylyuk and Albert P. Philipse. Effect of particle shape on the random packing density of amorphous solids. *physica status solidi (a)*, 208(10):2299–2302, 2011.

[189] Yu. Trukhina and T. Schilling. Computer simulation study of a liquid crystal confined to a spherical cavity. *Phys. Rev. E*, 77:011701, 2008.

[190] G. H. Koenderink, G. A. Vliegenthart, S. G. J. M. Kluijtmans, A. van Blaaderen, A. P. Philipse, and H. N. W. Lekkerkerker. Depletion-induced crystallization in colloidal rodsphere mixtures. *Langmuir*, 15(14):4693–4696, 1999.

[191] Marie Adams, Zvonimir Dogic, Sarah Keller, and Seth Fraden. Entropically driven microphase transitions in mixtures of colloidal rods and spheres. *Nature*, 393:349–351, 2001.

[192] J. Opdam, D. Guu, M. P. M. Schelling, D. G. A. L. Aarts, R. Tuinier, and M. P. Lettinga. Phase stability of colloidal mixtures of spheres and rods. *The Journal of Chemical Physics*, 154(20):204906, 2021.

[193] Mengqi Xiao, Jingjing Liu, Zhijie Chen, Wenxuan Liu, Chengcheng Zhang, Yingying Yu, Chaoran Li, and Le He. Magnetic assembly and manipulation of janus photonic crystal supraparticles from a colloidal mixture of spheres and ellipsoids. *J. Mater. Chem. C*, 9:11788–11793, 2021.

[194] Michael P. Howard, Wesley F. Reinhart, Tanmoy Sanyal, M. Scott Shell, Arash Nikoubashman, and Athanassios Z. Panagiotopoulos. Evaporation-induced assembly of colloidal crystals. *The Journal of Chemical Physics*, 149(9):094901, 2018.

[195] Steffen Egly, Christina Fröhlich, Stefanie Vogel, Alina Gruenewald, Junwei Wang, Rainer Detsch, Aldo R. Boccaccini, and Nicolas Vogel. Bottom-up assembly of silica and bioactive glass supraparticles with tunable hierarchical porosity. *Langmuir*, 34(5):2063–2072, 2018.

[redacted]

[redacted]

Melis Yetkin

Curriculum Vitae

[redacted]